"G. d'Annunzio" University of Chieti-Pescara

School of Advanced Studies "G. d'Annunzio"

DOCTORATE OF RESEARCH IN:

BIOMOLECULAR AND PHARMACEUTICAL SCIENCES

CYCLE XXXVIII

"Inorganic and inorganic-organic solids for selective adsorption of target molecules from aqueous media in solid phase extraction"

Department of Medical, Oral and Biotechnological Sciences

Scientific Disciplinary Sector CHEM-07/A

PhD Student

Irene Di Guida

Coordinator

Prof. Assunta Pandolfi

Academic tutor

Prof. Serena Fiorito

Industrial tutor

Roberto Spogli

Academic Years 2022/2025

ACKNOWLEDGEMENTS

During the last three years many people have helped me writing this work. First of all, I'd like to thank all the people in Prolabin&Tefarm, in particular Roberto Spogli and Michele Sisani for giving me this opportunity, Caterina Faffa for sharing the highs and lows of this experience and Gabriele Pastori for the advices.

I'd also like to thank Prof. Francesco Epifano and his group, specifically Prof. Serena Fiorito and Chiara Collevecchio for the collaboration and support they gave me during the PhD course.

One last thank goes to Prof. Paolo Colombo from Università di Padova and his group for the development of the LHD pellets.

INDEX

1 Introduction 1

1.1 Solid phase extraction 1

1.2 Layered double hydroxides 3

1.2.1 Structural aspects 3

1.2.2 Synthetic strategies 5

1.3 Non lamellar solids used in SPE 6

1.4 Phytoextracts as a source of natural molecules useful for everyday life 7

1.4.1 *Gentiana lutea* extract 7

1.4.2 *Polygonum cuspidatum* extract 8

1.5 Antibiotics as a source of water pollution 8

1.6 Aim of this work 9

Bibliography 12

2 Materials and methods 16

2.1 Instrumental set 16

2.1.1 X-ray powder diffractometry 16

2.1.2 Atomic emission spectroscopy ICP/OES 17

2.1.3 Thermal analysis (TGA and DSC) 18

2.1.4 IR spectroscopy 19

2.1.5 UV-VIS spectroscopy 20

2.1.6 Scanning electron microscopy (SEM) 21

2.1.7 Surface area analysis with B.E.T. method 22

2.1.8 High performance liquid chromatography HPLC 23

2.2 Materials 24

2.2.1 Commercial solids 24

2.2.2 Synthesis and modification of LDHs 24

2.2.3 Silica surface modification 30
2.3 Methods 31
2.3.1 Target molecules adsorption from phytoextracts 31
2.3.2 Desorption of target molecules from MgAl-azelate LDH and FT-IR-ATR analysis 34
2.3.3 Antibiotic adsorption studies 35
Bibliography 38
3 Results and discussion Adsorption of target molecules from phytoextracts 39
3.1 Characterization of synthetized inorganic LDHs 39
3.2 Characterization of organically modified LDHs 42
3.2.1 Characterization of deprotonated C_2-C_{12} dicarboxylic acids modified MgAl LDHs 42
3.2.2 Characterization of deprotonated monocarboxilic acids modified MgAl LDHs 57
3.2.3 Characterization of modified silica 60
3.3 Extraction of gentiopicroside and amarogentin from *Gentiana lutea* 63
3.3.1 Effect of the intercalated conjugated bases of dicarboxylic acids chain length 63
3.3.2 Comparison between deprotonated monocarboxylic and dicarboxylic acids with same chain length as anions in the interlayer region 66
3.3.3 Study of the matrix effect 67
3.4 Extraction of emodin and chrysophanol from *Polygonum cuspidatum* 68
3.5 Characterization of MgAl-azelate before and after the adsorption processes 69
3.5.1 XRPD analysis 70
3.5.2 SEM imaging 71
3.5.3 BET surface area analysis 73
3.5.4 FT-IR-ATR analysis 74
3.6 Study of the effect of the surface area 75
3.6.1 XRPD analysis 77

3.6.2 SEM images 77
3.6.3 BET analysis 78
3.6.4 FT-IR-ATR analysis 78
Bibliography 80
4 Results and discussion Antibiotic removal from water 81
4.1 Characterization of synthetized sorbent solids 81
4.2 Adsorption tests of SMX on LDHs based on ion exchange 86
4.2.1 LDHs screening 86
4.2.2 Effect of the pH 88
4.2.3 Kinetic of the adsorption process 89
4.2.4 Effect of the SMX / LDH ratio 90
4.2.5 SEM characterization of the LDH after the adsorption 90
4.3 Adsorption tests on sorbent solids based on non-ionic interactions 93
4.3.1 Adsorption of SMX 93
4.3.2 Adsorption of CPX 94
4.3.3 Solids characterization after adsorption 95
4.3.4 Adsorption of SMX, CPX and TC 103
4.3.5 Solids characterization after adsorption of SMX, CPX and TC 105
4.4 Production of pellets for adsorption tests in column 107
Bibliography 109
5 Conclusions and future developments 110
5.1 Target molecules separation from phytoextracts 110
5.2 Antibiotic removal 111

1 INTRODUCTION

1.1 SOLID PHASE EXTRACTION

The extraction of selected molecules from complex matrices of various chemical composition is a fundamental step in the isolation process that is required for pre-concentration or extraction of analytes or for the purification of matrices from a selected pollutant. Extraction of complex molecules from natural extracts is often an easier and cheaper way to obtain them compared to their synthesis in chemical laboratory. A very powerful and widely used technique is solid phase extraction (SPE), that provides isolation and purification of many analytes, including selected secondary metabolites, from matrices of different origin. Most of the materials used for this process are economic and the selected analytes are usually recovered in high percentages and with high enrichment factors. Moreover, SPE stands out for the fast phase separation that they provide and the possibility to couple it with many techniques for the detection of chemical compounds of interest. This process has a wide range of application, from purification to trace enrichment, as well as derivatization, class fractionation and desalting[1].

As for liquid-liquid extraction process, SPE is based on the partition of analytes between two phases, but in this case one is liquid and made of the solution of the compounds of interest, while the other one is constituted by a sorbent insoluble solid. In addition, in this case, the extraction can be performed in normal phase (with a polar sorbent and a non-polar or slightly polar solvent for the extraction of polar analytes), reverse phase (with a non-polar or slightly polar sorbent and a polar solvent for the extraction of non-polar or slightly polar analytes) or based on ion exchange. The most common configuration involves the use of a cartridge or a column to pack the sorbent solid, that is usually in quantities (for laboratory experiment scale) that varies from milligrams to grams; the sample is eluted through the solid phase thanks to the application of a positive pressure on the top of the cartridge or a negative one below it. Other used configurations include disk SPE, multi-well SPE, solid phase micro-extraction and magnetic SPE[2].

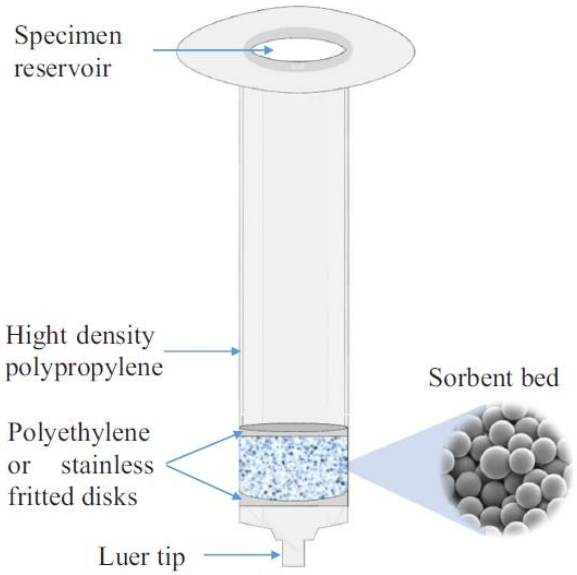

Figure 1. 1 SPE cartridge scheme[2]

The choice of the sorbent material is a key factor for the success of the extraction and adsorption of the target compounds, therefore the knowledge of the type and mechanism of interaction between the sorbent and the analyte is fundamental to select the most suitable and efficient extraction system: a preliminary study of hydrophobic, polar, and ionogenic properties of both the solute and the solid phase helps to select the best SPE design. Hydrogen bonding, Van der Waals interactions, dipole-dipole forces and ionic interactions are the most commonly observed retention mechanisms for SPE[3]. The solid phase can be made of numerous sorbent materials of different chemical nature, but most of them are characterized by a high surface area that is the result of a rigid and porous three-dimensional structure. The materials are usually divided in classes based on their chemical nature and the most commonly used are the ones already known in the analytical chemistry field: silica gels that could be chemically modified (i.e. normal phase or reverse phases up to C-18), polymeric sorbents (usually copolymers of styrene and divinylbenzene) and graphitized or porous carbon. Starting from polymeric materials, also immunosorbents can be synthetized for the selection of proteins, peptides, hormones and antibodies[4] while, for a high selectivity of other biological molecules, molecular imprinted polymers have been developed[5]. Nanosized materials have also been used as sorbents in SPE due to their very high surface area[6]. Among this class of

solids, also layered double hydroxides (LDHs), as synthetized or after modification, have been used in different types of SPE, such as dispersive SPE[7,8] or magnetic SPE[9,10].

1.2 LAYERED DOUBLE HYDROXIDES

Layered double hydroxides (LDHs) are mixed hydroxides of divalent and trivalent metals with comparable ionic radii with an exchangeable anion in-between the hydroxyl layers. These materials, as other lamellar solids, can indeed form host-guest structures with both inorganic and organic anions with a phenomenon called "intercalation" (Figure 1.2): this ability makes them suitable for the uptake of specific anions and/or their release.

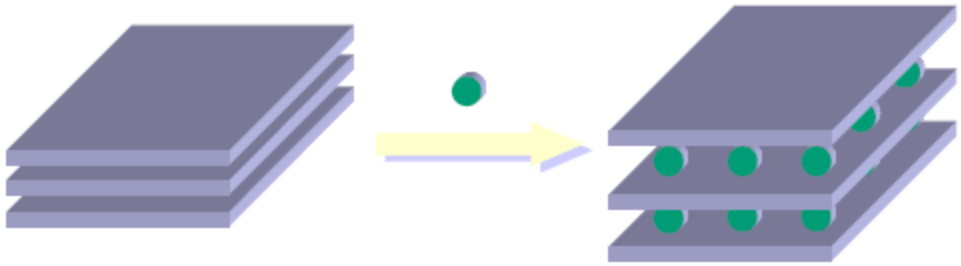

Figure 1. 2 Scheme of an intercalation of a lamellar solid

The possibility to synthetically vary the chemical composition of the metals and the anion and to exchange the anion has made this class of materials used in many different fields, for example as catalyst, polymer additive, drug delivery system, cosmetics additive, and also as adsorption agent.

1.2.1 Structural aspects

The crystalline structure of these materials is brucite-like: in the $Mg(OH)_2$ mineral every Mg^{2+} atom is coordinated by six OH^- anions in an octahedral geometry with shared corners, originating planes of metal hydroxides that are packed via van der Waals forces. LDHs are instead composed of layers of hydroxides, where, for each metal, two hydroxyl groups are bound: this stoichiometry, due to the presence of trivalent cations, provides an excess of positive charge that is compensated by exchangeable anions in the interlayer region. The general formula for these solids is:

$$[M(II)_{1-x}M(III)_x(OH)_2]^{x+}[A^{n-}_{x/n}]^{x-} \cdot mH_2O$$

Where M(II) is the divalent metal, M(III) is the trivalent metal, x is the cationic molar fraction of the divalent metal (expressed as $M(III)/[M(III) + M(II)]$), n is the charge of the anion in the interlayer region and m are the moles of water per mole of solid, usually $0.4 \leq m \leq 1$.

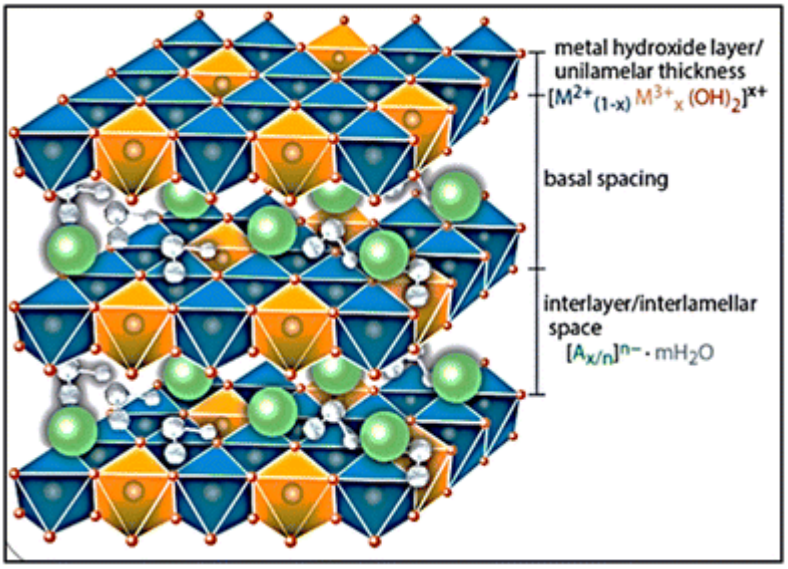

Figure 1. 3 Scheme of LDH crystalline structure[11]

The longest known example of mineral LDH, named hydrotalcite, is made of Mg as divalent metal, Al as trivalent metal and carbonate as anion. In the hydrotalcites group of minerals are reported more than 40 minerals with different polytypic phases[12]. The term LDH originates from Feitknecht's work, that consisted in the synthesis of hydrotalcite-like compounds, that he named "doppelschichtstrukturen", that can be translated as double plane structures. The first formulated hypothesis on the structure of these solids was the intercalation of planes made of divalent cations hydroxides with planes made of trivalent cations hydroxides[13]. This theory was then overcome after single crystal X-ray diffraction experiments[14,15].

The possibility to synthetize these materials, allows their customization varying the chemical nature of the metals and of the anion. The main characteristic of the cations that can give origin to LDHs is the octahedral coordination structure of their hydroxides[16]: this makes Mg^{2+}, Zn^{2+}, Co^{2+}, Mn^{2+}, Fe^{2+}, Ni^{2+} cations suitable components for the layers. The trivalent metals have to isomorphically substitute some divalent cations, making their ionic radius a key parameter in the determination of the possibility to incorporate them in the layers[17,18]. The most commonly used trivalent anion are Al^{3+}, Cr^{3+} or Fe^{3+}. Table 1.1 shows the ionic radii of some divalent and trivalent metals expressed in Å according to Shannon[19].

Table 1. 1 Ionic radii of different divalent and trivalent metals

M(II)	**Be**	**Mg**	**Cu**	**Ni**	**Co**	**Zn**	**Fe**	**Mn**	**Cd**	**Ca**
Radius (Å)	0.30	0.65	0.69	0.72	0.74	0.74	0.76	0.80	0.97	0.98
M(III)	**Al**	**Ga**	**Ni**	**Co**	**Fe**	**Mn**	**Cr**	**V**	**Ti**	**In**
Radius (Å)	0.50	0.62	0.62	0.63	0.64	0.66	0.69	0.74	0.76	0.81

The hard nature of Be^{2+} implies the difficulty of formation of octahedral complexes[20], hence the difficulty to form a Be containing LDH. The other divalent metals listed in Table 1.1 can give origin to LDH structures, with the exception of Cu^{2+} that needs the presence of another divalent cation of those listed in the table due to the presence of the Jahn-Teller effect[21]. All trivalent metals characterized by an ionic radius that varies between 0.5 Å and 0.8 Å can be incorporated in the LDH structure.

The molar fraction of the trivalent metal *x* is also important in the evaluation of the stability and the purity of the crystalline phases. To avoid the segregation of different phases (in the case of the hydrotalcite the hydroxides of the trivalent or the divalent ion), it is known that the optimal range is $0.20 \leq x \leq 0.33$[22].

The nature of the anion in the interlayer region can vary on the basis of the purpose of the material and can be grouped in four different types:

1. inorganic anions: F^-, Cl^-, Br^-, I^-, $(ClO_4)^-$, $(NO_3)^-$, $(ClO_3)^-$, $(IO_3)^-$, $(OH)^-$, $(CO_3)_2^-$, $(SO_4)^{2-}$, $(S_2O_3)^{2-}$, $(WO_4)^{2-}$, $(CrO_4)^{2-}$, $[SiO(OH)_3]^-$;
2. isopolianions ($V_{10}O_{28}^{6-}$, $Mo_7O_{24}^{6-}$, etc.) ed eteropolianions ($PMo_{12}O_{40}^{3-}$, $PW_{12}O_{40}^{3}$ etc.);
3. anionic complexes ($[Fe(CN)_6]^{3-}$, $[Fe(CN)_6]^{4-}$, etc.) and organometallic complexes;
4. organic acids derived anions: with e.g. carboxylic, solphonic, and phosphonic, moieties.

The interlayer distance depends on the steric hindrance and the number of the intercalated anions.

1.2.2 Synthetic strategies

Many different strategies have been reported for the synthesis of LDHs, such as[11,23]:

1. Co-precipitation method
2. Hydrothermal synthesis
3. Sol-gel synthesis
4. Urea method

The co-precipitation method is the most used one and consists in the precipitation of the metal hydroxides starting from a diluted solution of salts of the desired layer components and of the target anion for the interlayer region. The equilibrium of the solution is then disturbed by slowly adding an alkali solution (typically NaOH). Controlling the concentration of the reagents, the temperature, the speed and hence the time of addition, the morphology and crystallinity of the resulting materials can be tuned.

In the second case the reaction is conducted under pressure and at high temperature (as high as 180°C), starting from mixtures of metal hydroxides or oxides and the control of temperature and reaction time is also in this case necessary to modify the crystallinity of the final material.

The sol gel synthesis is performed by firstly obtaining the mixed metal oxides of the desired metals via the formation of a gel in an organic solvent and subsequent calcination, and then reconstituting the hydroxides dispersing the material in water by increasing the pH[24].

With the urea method, the material is obtained through the addition of urea to a solution of the salts of the divalent and trivalent metals and heating the resulting solution up to the boiling point. With the temperature increase, urea decomposes to ammonium cyanate, which then undergoes a hydrolysis reaction leading to the formation of ammonium carbonate, as it can be seen in the following equations.

$$CO(NH_2)_2 \rightleftarrows NH_4OCN$$

$$NH_4OCN + H_2O \rightleftarrows (NH_4)_2CO_3$$

The ammonium carbonate is responsible for a slow increase of the pH that determines a slow precipitation-dissolution-reprecipitation of the mixed hydroxides of the metals in solution. The slow process leads to the formation of a material characterised by a good degree of crystallinity.

The anion bound to the layers via electrostatic interaction can be exchanged after the synthetic process with others with higher affinity for the layers, that depends on the dimensions of the anion and its charge density.

1.3 NON LAMELLAR SOLIDS USED IN SPE

Other inorganic solids that can be used in SPE as they are or after modification (e.g. an organic functionalization) are silica[25] and magnesium oxide[26].

Silica (chemical formula SiO_2) is widely spread in nature: it is usually found as mineral in the form of quartz, is the main constituent of sand and is also found as biosilica for example in unicellular organisms and primitive animals as sponges[27]. It is easily industrially synthetized and therefore it is commercially available with a variety of different characteristics (e.g. dimensions, morphology). It is used in SPE as it is as sorbent solid for the extraction of polar compound in normal phase extractions, but it can also be modified using the free OH moieties on the surface to chemically bond organic molecules in order to customize the material for specific applications[28].

Magnesium oxide, commonly called magnesia, is a white solid with chemical formula MgO found in nature in mineral form of periclase, while the synthetic one is usually produced by calcination of magnesium carbonate or magnesium hydroxide[29] and is widely commercially available. Among its numerous applications, it has been used in micrometric and nanometric form and unmodified or organically modified as sorbent solid in SPE processes[26,30].

1.4 PHYTOEXTRACTS AS A SOURCE OF NATURAL MOLECULES USEFUL FOR EVERYDAY LIFE

It is well known from the past that some plants and their extracts have interesting properties for human beings. Once the compounds responsible for those properties are identified, the possibility to selectively isolate them is fundamental to better use them in different applications. Some phytoextract isolated compounds can be used in the nutraceutical, cosmeceutical or pharmaceutical fields, while others can be used in the food industry for example, without the possible detrimental contributions of other compounds found in the same pristine extract and in order to do so SPE has already been used in the isolation process[31,32].

In the present work two phytoextracts were studied: *Gentiana lutea* extract, that is characterized by the presence of compounds of both pharmacological interest[33] and for the food industry[34], and *Polygonum cuspidatum extract*, with a good concentration of anthraquinones[31] that can be useful for pharmacological applications[35].

1.4.1 *Gentiana lutea* extract

G. lutea is a perennial herb, widely spread in the mountainous regions of western Asia and central and southern Europe and its roots are used in the production of a bitter alcoholic beverage. The compounds responsible for its bitterness are well known and are gentiopicroside and amarogentin, both characterized by secoiridoid glycoside structures[36].

Their bitter indexes are 12 x 10^3 for gentiopicroside and 58 x 10^6 for amarogentin, therefore they are considered among the most bitter naturally occurring compounds.

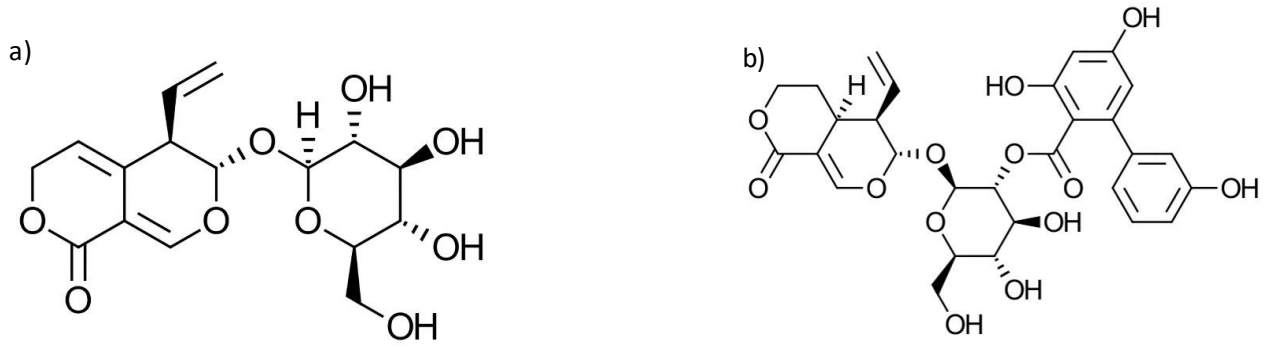

Figure 1. 4 Chemical structures of a) gentiopicroside and b) amarogentin

1.4.2 *Polygonum cuspidatum* extract

P. cuspidatum is an herb that grows in Asia and north America. It has been used in traditional Chinese medicine due to the presence of different active compounds such as anthraquinones (e.g. emodin and chrysophanol) and stilbenes (e.g. resveratrol and polydatin)[37,38].

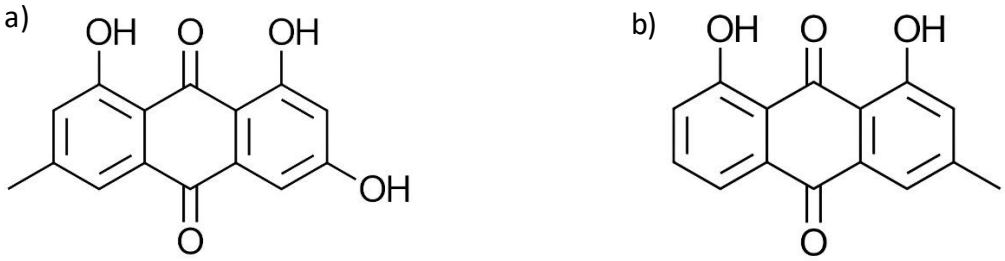

Figure 1. 5 Chemical structure of a) emodin and b) chrysophanol

Emodin and chrysophanol have shown interesting therapeutic properties: the former is reported to have for example antibacterial, anti-inflammatory, diuretic and anticancer properties[39], while the latter has been reported to have, among others, hepatoprotective, anticancer, anti-inflammatory and neuroprotective activity[40].

1.5 Antibiotics as a source of water pollution

The growing water pollution problem demands the development of adsorbing materials that can lower contaminants concentration under thresholds considered safe for environment and human health.

An increasing pollution source is constituted by pharmaceuticals that, during not only their production, but also their use and disposal, are released in the environment, in particular in the

wastewater: after the human consumption part of the drugs is excreted with urine or feces and enters the water streams, adding to the amount of drugs that derives from their production. Their high consumption, together with their bioaccumulation and non-biodegradable nature raise many concerns[41]. Specifically, antibiotics, used to treat bacterial human and animal infections, when accumulated in water streams, can contribute to antimicrobial resistance and can interfere with the ecosystems[42]. These compounds are found in rivers, lakes, seawater and drinking water worldwide, originating from hospitals, households, farming and pharmaceutical industries and they are not completely removed by conventional wastewater treatment plants[43].

Three of the most used and diffused antibiotics in waters are sulfamethoxazole (SMX), ciprofloxacin (CPX) and tetracycline hydrochloride (TC), widely diffused for treatment of humans and veterinarian animals[44,45]. Their chemical structures are shown in Figure 1.6.

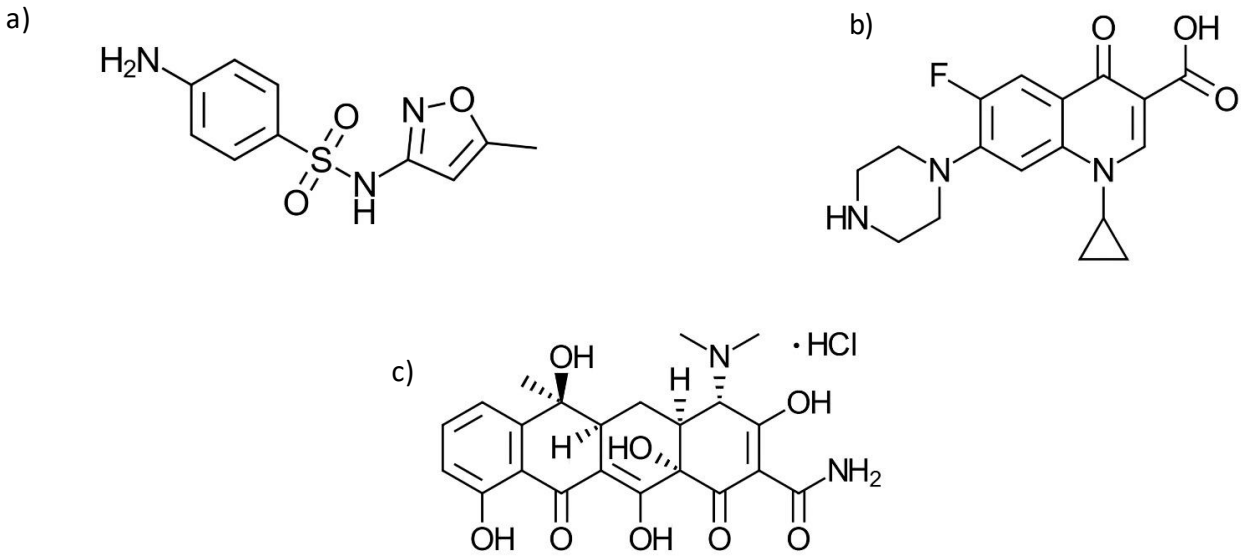

Figure 1. 64 Chemical structures of a) SMX, b) CPX and c) TC

1.6 AIM OF THIS WORK

The focus of the present work is on the isolation of two different types of compounds via SPE procedures using lamellar solids, specifically LDHs, and other inorganic and inorgano-organic sorbent solids.

The first part describes the extraction procedures of gentiopicroside and amarogentin from *G. lutea* and emodin and chrysophanol from *P. cuspidatum.* The use of many LDHs with different metal compositions and different anions in the interlayer region, as well as other inorganic and inorgano-organic materials as sorbent solids in the SPE process for the isolation of gentiopicroside and

amarogentin has already been reported by our research group[34] and the best performances have been registered for MgAl-azelate LDH, material that has shown good adsorption capacities also towards emodin[31]. In this work the mechanism of adsorption is studied by testing the adsorption capacity of nine organically modified MgAl LDHs with dicarboxylic acids with different chain lengths, two organically modified MgAl LDHs with monocarboxylic acids, two MgAl-CO_3 LDHs with different surface areas and an organically modified commercial silica. Specifically, the tested materials are:

1. MgAl-oxalate
2. MgAl-malonate
3. MgAl-succinate
4. MgAl-glutarate
5. MgAl-adipate
6. MgAl-pimelate
7. MgAl-suberate
8. MgAl-sebacate
9. MgAl-dodecandioate
10. MgAl-pentanoate
11. MgAl-nonanoate
12. MgAl-CO_3 with low surface area
13. MgAl-CO_3 with high surface area
14. Organically modified commercial silica with azelaic acid on the surface

Moreover, a structural and morphological analysis of MgAl-azelate LDH is conducted before and after the adsorption processes of gentiopicroside and amarogentin and of emodin and chrysophanol.

The second part of this thesis focuses on the removal of three antibiotics (SMX, CPX and TC) from aqueous systems. Different approaches have been reported in literature for the lowering of the concentration of these compounds, from the degradation to the adsorption on sorbent solids[43–47]. Removal of SMX has been tested using as sorbent solids LDHs such as biochar/MgAl LDH compound[48], MgAl-NO_3[49] and ZnAl-CO_3 calcined[50] but, in the first case the adsorbent was not constituted by only LDH, in the second case no great adsorptions were registered, and in the last reported example the good results were registered after the energetically demanding calcination

step. LDHs based adsorptions have been reported also for CPX[51,52] and TC[53,54], but to the best of our knowledge no LDH was tested for the simultaneous removal of the three antibiotics.

In this work the tested sorbent solids did not limit to LDHs, but also MgO was tested. A list of all the studied materials follows:

1. MgAl-NO_3
2. MgAl-Cl
3. ZnAl-NO_3
4. ZnAl-Cl
5. ZnAl-acetate
6. MgAl-pentanoate
7. MgAl-oxalate
8. MgAl-malonate
9. MgAl-succinate
10. MgAl-glutarate
11. MgAl-adipate
12. MgAl-pimelate
13. MgAl-suberate
14. MgAl-azelate
15. MgAl-sebacate
16. MgAl-dodecandioate
17. MgO

The most promising materials were characterized before and after the antibiotics adsorption via XRPD, SEM and BET surface analysis in order to verify if any changes occurred in the morphology and the structure of the materials.

All the sorbent materials were synthetized for this work, except MgAl-azelate that was already synthetized in our laboratories for previous studies[34] and MgO that was purchased.

BIBLIOGRAPHY

[1] F. Epifano, S. Genovese, L. Marchetti, L. Palumbo, M. Bastianini, F. Cardellini, R. Spogli, S. Fiorito, "Solid phase adsorption of anthraquinones from plant extracts by lamellar solids" *J. Pharm. Biomed. Anal.* **2020**, *190*, 113515.

[2] M. E. I. Badawy, M. A. M. El-Nouby, P. K. Kimani, L. W. Lim, E. I. Rabea, "A review of the modern principles and applications of solid-phase extraction techniques in chromatographic analysis" *Anal. Sci.* **2022**, *38*, 1457–1487.

[3] J. Płotka-Wasylka, M. Marć, N. Szczepańska, J. Namieśnik, "New Polymeric Materials for Solid Phase Extraction" *Crit. Rev. Anal. Chem.* **2017**, *47*, 373–383.

[4] H. Kaur, S. R. Bhagwat, T. K. Sharma, A. Kumar, "Analytical Techniques for Characterization of Biological Molecules – Proteins and Aptamers/Oligonucleotides" *Bioanalysis* **2019**, *11*, 103–117.

[5] Monika Sobiech, Piotr Luliński, "Molecularly imprinted solid phase extraction – recent strategies, future prospects and forthcoming challenges in complex sample pretreatment process" *Trends Anal. Chem.* **2024**, *174*, 117695.

[6] N. Nouri, P. Khorram, O. Duman, T. Sibel, S. Hassan, "Overview of nanosorbents used in solid phase extraction techniques for the monitoring of emerging organic contaminants in water and wastewater samples" *Trends Environ. Anal. Chem.* **2020**, *25*, e00081.

[7] Elnaz Marzi Khosrowshahi, Alireza Khataee, Samira Arefi-Oskoui, Yasin Orooji, "Dispersive solid phase extraction of perfluorooctanoic acid from wastewater using chromium-doped CoFe layered double hydroxide for determination by LC-MS/MS" *Microchem. J.* **2024**, *199*, 109918.

[8] M. Ezoddin, L. Adlnasab, A. Afshari Kaveh, M. A. Karimi, B. Mahjoob, "Development of air-assisted dispersive micro-solid-phase extraction-based supramolecular solvent-mediated Fe_3O_4 @Cu–Fe–LDH for the determination of tramadol in biological samples" *Biomed. Chromatogr.* **2019**, *33*, e4572.

[9] T. Hubetska, V. Demchenko, N. Kobylinska, "Surface engineering: binary Mg,Fe-LDH· *x* Fe_3O_4 nanocomposites for improved magnetic solid-phase extraction of pharmaceuticals from aqueous solution" *Mater. Adv.* **2024**, *5*, 8145–8163.

[10] M. Rajabi, M. Abolhosseini, A. Hosseini-Bandegharaei, M. Hemmati, N. Ghassab, "Magnetic dispersive micro-solid phase extraction merged with micro-sampling flame atomic absorption spectrometry using (Zn-Al LDH)-(PTh/DBSNa)-Fe3O4 nanosorbent for effective trace determination of nickel(II) and cadmium(II) in food samples" *Microchem. J.* **2020**, *159*, 105450.

[11] A. A. Altalhi, E. A. Mohamed, N. A. Negm, "Recent advances in layered double hydroxide (LDH)-based materials: fabrication, modification strategies, characterization, promising environmental catalytic applications, and prospective aspects" *Energy Adv.* **2024**, *3*, 2136–2151.

[12] S. J. Mills, A. G. Christy, J.-M. R. Génin, T. Kameda, F. Colombo, "Nomenclature of the hydrotalcite supergroup: natural layered double hydroxides" *Mineral. Mag.* **2012**, *76*, 1289–1336.

[13] W. Feitknecht, M. Gerber, "Zur Kenntnis der Doppelhydroxyde und basischen Doppelsalze II. Über Mischfällungen aus Calcium-Aluminiumsalzlösungen" *Helv. Chim. Acta* **1942**, *25*, 106–131.

[14] R. Allmann, "The crystal structure of pyroaurite" *Acta Crystallogr. B* **1968**, *24*, 972–977.

[15] H. F. W. Taylor, "Segregation and cation-ordering in sj6grenite and pyroaurite" *Mineral. Mag.* **1969**, *37*.

[16] Fritz Hulliger, *Structural Chemistry of Layer-Type phases, of Physics and Chemistry of Materials with Layered Structures*, F.A Lévy (D. Reidel Publishing Company, **1976**.
[17] W. Reichle, "Synthesis of anionic clay minerals (mixed metal hydroxides, hydrotalcite)" *Solid State Ion.* **1986**, *22*, 135–141.
[18] R. M. Taylor, "The rapid formation of crystalline double hydroxy salts and other compounds by controlled hydrolysis" *Clay Miner.* **1984**, *19*, 591–603.
[19] R. D. Shannon, "Revised Effective Ionic Radii and Systematic Studies of Interatomie Distances in Halides and Chaleogenides" *Acta Crystallogr.* **1976**, *A32*, 751.
[20] L. C. Perera, O. Raymond, W. Henderson, P. J. Brothers, P. G. Plieger, "Advances in beryllium coordination chemistry" *Coord. Chem. Rev.* **2017**, *352*, 264–290.
[21] I. Z. Awan, P. H. Ho, G. Beltrami, O. Gimello, T. Cacciaguerra, P. Gaudin, N. Tanchoux, S. Albonetti, A. Martucci, F. Cavani, D. Tichit, F. Di Renzo, "Design of Multicationic Copper-Bearing Layered Double Hydroxides for Catalytic Application in Biorefinery" *ChemCatChem* **2023**, *15*, e202201622.
[22] Mengting Duan, Shanjing Liu, Qiming Jiang, Xingmei Guo, Junhao Zhang, Shenglin Xiong, "Recent progress on preparation and applications of layered double hydroxides" *Chin. Chem. Lett.* **2022**, *33*, 4428–4436.
[23] U. Costantino, F. Marmottini, M. Nocchetti, R. Vivani, "New Synthetic Routes to Hydrotalcite-Like Compounds − Characterisation and Properties of the Obtained Materials" *Eur. J. Inorg. Chem.* **1998**, *1998*, 1439–1446.
[24] L. Valeikiene, M. Roshchina, I. Grigoraviciute-Puroniene, V. Prozorovich, A. Zarkov, A. Ivanets, A. Kareiva, "On the Reconstruction Peculiarities of Sol–Gel Derived Mg2−xMx/Al1 (M = Ca, Sr, Ba) Layered Double Hydroxides" *Crystals* **2020**, *10*, 470.
[25] Michael J. Telepchak, Thomas F. August, Glynn Chaney, *Silica-Based Solid Phase Extraction. In: Forensic and Clinical Applications of Solid Phase Extraction*, Humana Press, **2004**.
[26] W. Li, J. Qiu, L. Baharinikoo, T. Ch. A. Kumar, B. Al-qargholi, S. S. Shafik, R. Abbass, S. K. Saraswat, "Dispersive solid phase microextraction based on magnesium oxide nanoparticles for preconcentration of auramine O and methylene blue from water samples" *Sci. Rep.* **2022**, *12*, 12806.
[27] C. C. Perry in *Biosilica Evol. Morphog. Nanobiotechnology* (Eds.: W.E.G. Müller, M.A. Grachev), Springer Berlin Heidelberg, Berlin, Heidelberg, **2009**, pp. 295–313.
[28] L. Zhang, X. Chang, Z. Hu, L. Zhang, J. Shi, R. Gao, "Selective solid phase extraction and preconcentration of mercury(II) from environmental and biological samples using nanometer silica functionalized by 2,6-pyridine dicarboxylic acid" *Microchim. Acta* **2010**, *168*, 79–85.
[29] M. Seeger, W. Otto, W. Flick, F. Bickelhaupt, O. S. Akkerman in *Ullmanns Encycl. Ind. Chem.* (Ed.: Wiley-VCH), Wiley, **2011**.
[30] J. Jin, Z. Zhang, Y. Li, X. Lu, L. Wu, J. Chen, "Preparation, characterization and application of octadecyl modified magnesium oxide microspheres" *Anal. Chim. Acta* **2011**, *693*, 54–61.
[31] S. Genovese, F. Epifano, L. Palumbo, G. Pulito, M. Bastianini, F. Cardellini, R. Spogli, S. Fiorito, "Solid phase adsorption of emodin on hydrotalcites and inorganic oxides: A preliminary study" *J. Pharm. Biomed. Anal.* **2020**, *187*, 113348.
[32] S. Genovese, F. Epifano, L. Marchetti, M. Bastianini, F. Cardellini, R. Spogli, S. Fiorito, "Pre-concentration of active principles from different varieties of Camellia sinensis extracts by solid sorbents" *J. Pharm. Biomed. Anal.* **2021**, *196*, 113945.
[33] M. Jiang, B.-W. Cui, Y.-L. Wu, J.-X. Nan, L.-H. Lian, "Genus Gentiana: A review on phytochemistry, pharmacology and molecular mechanism" *J. Ethnopharmacol.* **2021**, *264*, 113391.

[34] S. Fiorito, F. Epifano, L. Palumbo, C. Collevecchio, F. Mascioli, R. Spogli, S. Genovese, “Leaves of Yellow Gentian (*Gentiana lutea*) as an Alternative Source of Bitter Secoiridoid Glycosides” *J. Nat. Prod.* **2022**, *85*, 2232–2235.
[35] E. M. Malik, C. E. Müller, “Anthraquinones As Pharmacological Tools and Drugs” *Med. Res. Rev.* **2016**, *36*, 705–748.
[36] A. Ariño, I. Arberas, M. J. Leiton, M. De Renobales, J. B. Dominguez, “The extraction of yellow gentian root (Gentiana lutea L .)” *Z Leb. Unters Forsch A* **1997**, *205*, 295–299.
[37] J. Ke, M.-T. Li, S. Xu, J. Ma, M.-Y. Liu, Y. Han, “Advances for pharmacological activities of *Polygonum cuspidatum* - A review” *Pharm. Biol.* **2023**, *61*, 177–188.
[38] W. Peng, R. Qin, X. Li, H. Zhou, “Botany, phytochemistry, pharmacology, and potential application of Polygonum cuspidatum Sieb.et Zucc.: A review” *J. Ethnopharmacol.* **2013**, *148*, 729–745.
[39] M. Stompor-Gorący, “The Health Benefits of Emodin, a Natural Anthraquinone Derived from Rhubarb—A Summary Update” *Int. J. Mol. Sci.* **2021**, *22*, 9522.
[40] Prateeksha, M. A. Yusuf, B. N. Singh, S. Sudheer, R. N. Kharwar, S. Siddiqui, A. M. Abdel-Azeem, L. Fernandes Fraceto, K. Dashora, V. K. Gupta, “Chrysophanol: A Natural Anthraquinone with Multifaceted Biotherapeutic Potential” *Biomolecules* **2019**, *9*, 68.
[41] H. Rodríguez-Serin, A. Gamez-Jara, M. De La Cruz-Noriega, S. Rojas-Flores, M. Rodriguez-Yupanqui, M. Gallozzo Cardenas, J. Cruz-Monzon, “Literature Review: Evaluation of Drug Removal Techniques in Municipal and Hospital Wastewater” *Int. J. Environ. Res. Public. Health* **2022**, *19*, 13105.
[42] J. L. Wilkinson, A. B. A. Boxall, D. W. Kolpin, K. M. Y. Leung, R. W. S. Lai, C. Galbán-Malagón, A. D. Adell, J. Mondon, M. Metian, R. A. Marchant, A. Bouzas-Monroy, A. Cuni-Sanchez, A. Coors, P. Carriquiriborde, M. Rojo, C. Gordon, M. Cara, M. Moermond, T. Luarte, V. Petrosyan, Y. Perikhanyan, C. S. Mahon, C. J. McGurk, T. Hofmann, T. Kormoker, V. Iniguez, J. Guzman-Otazo, J. L. Tavares, F. Gildasio De Figueiredo, M. T. P. Razzolini, V. Dougnon, G. Gbaguidi, O. Traoré, J. M. Blais, L. E. Kimpe, M. Wong, D. Wong, R. Ntchantcho, J. Pizarro, G.-G. Ying, C.-E. Chen, M. Páez, J. Martínez-Lara, J.-P. Otamonga, J. Poté, S. A. Ifo, P. Wilson, S. Echeverría-Sáenz, N. Udikovic-Kolic, M. Milakovic, D. Fatta-Kassinos, L. Ioannou-Ttofa, V. Belušová, J. Vymazal, M. Cárdenas-Bustamante, B. A. Kassa, J. Garric, A. Chaumot, P. Gibba, I. Kunchulia, S. Seidensticker, G. Lyberatos, H. P. Halldórsson, M. Melling, T. Shashidhar, M. Lamba, A. Nastiti, A. Supriatin, N. Pourang, A. Abedini, O. Abdullah, S. S. Gharbia, F. Pilla, B. Chefetz, T. Topaz, K. M. Yao, B. Aubakirova, R. Beisenova, L. Olaka, J. K. Mulu, P. Chatanga, V. Ntuli, N. T. Blama, S. Sherif, A. Z. Aris, L. J. Looi, M. Niang, S. T. Traore, R. Oldenkamp, O. Ogunbanwo, M. Ashfaq, M. Iqbal, Z. Abdeen, A. O’Dea, J. M. Morales-Saldaña, M. Custodio, H. De La Cruz, I. Navarrete, F. Carvalho, A. B. Gogra, B. M. Koroma, V. Cerkvenik-Flajs, M. Gombač, M. Thwala, K. Choi, H. Kang, J. L. C. Ladu, A. Rico, P. Amerasinghe, A. Sobek, G. Horlitz, A. K. Zenker, A. C. King, J.-J. Jiang, R. Kariuki, M. Tumbo, U. Tezel, T. T. Onay, J. B. Lejju, Y. Vystavna, Y. Vergeles, H. Heinzen, A. Pérez-Parada, D. B. Sims, M. Figy, D. Good, C. Teta, “Pharmaceutical pollution of the world’s rivers” *Proc. Natl. Acad. Sci.* **2022**, *119*, e2113947119.
[43] A. E. Gahrouei, S. Vakili, A. Zandifar, S. Pourebrahimi, “From wastewater to clean water: Recent advances on the removal of metronidazole, ciprofloxacin, and sulfamethoxazole antibiotics from water through adsorption and advanced oxidation processes (AOPs)” *Environ. Res.* **2024**, *252*, 119029.
[44] H. Chen, B. Gao, H. Li, “Removal of sulfamethoxazole and ciprofloxacin from aqueous solutions by graphene oxide” *J. Hazard. Mater.* **2015**, *282*, 201–207.
[45] C. Ding, Q. Zhu, B. Yang, E. Petropoulos, L. Xue, Y. Feng, S. He, L. Yang, “Efficient photocatalysis of tetracycline hydrochloride (TC-HCl) from pharmaceutical wastewater using AgCl/ZnO/g-

C3N4 composite under visible light: Process and mechanisms" *J. Environ. Sci.* **2023**, *126*, 249–262.

[46] A. Pereira, A. Freitas, M. Silva, A. Camara, H. Moura, D. Ballesteros-Plata, E. Rodríguez-Castellón, L. De Carvalho, "Efficient Removal of Tetracycline Hydrochloride via Adsorption onto Modified Bentonite: Kinetics and Equilibrium Studies" *Appl. Sci.* **2025**, *15*, 3372.

[47] Dehui Xiao, Rongrong Han, Luchen Ai, Shuhui An, Haonan Guo, Wenyuan Tan, Yijing Li, Peng Ju, Houshen Li, "Efficient removal of tetracycline hydrochloride by cobalt-modified Enteromorpha prolifera derived biochar: Synergy of adsorption and sulfite activation" *Sep. Purif. Technol.* **2025**, *377*, 134435.

[48] Guowan Li, Zhujian Huang, Chengyu Chen, Hongcan Cui, Yijuan Su, Yang Yang, Lihua Cui, "Simultaneous adsorption of trace sulfamethoxazole and hexavalent chromium by biochar/MgAl layered double hydroxide composites" *Environ. Chem.* **2019**, *16*, 68.

[49] A.-L. Johnston, E. Lester, O. Williams, R. L. Gomes, "Impacts of multi-pollutants on sulfonamide antibiotic removal from water matrices using layered double hydroxide sorbents" *Environ. Technol. Innov.* **2024**, *33*, 103490.

[50] E. H. Mourid, M. Lakraimi, L. Benaziz, E. H. Elkhattabi, A. Legrouri, "Wastewater treatment test by removal of the sulfamethoxazole antibiotic by a calcined layered double hydroxide" *Appl. Clay Sci.* **2019**, *168*, 87–95.

[51] Dayang Zheng, Min Wu, Eryang Zheng, Yayi Wang, Cang Feng, Jiali Zou, Maoling Juan, Xinxing Bai, Teng Wang, Yuxiang Shi, "Parallel adsorption of low concentrated ciprofloxacin by a CoFe-LDH modified sludge biochar" *J. Environ. Chem. Eng.* **2022**, *10*, 108381.

[52] Priyanka, Bonamali Pal, Satnam Singh, Mehak Bansal, "Superior adsorptive removal of ciprofloxacin by graphene oxide modified Ni-Al layered double hydroxide composites" *J. Alloys Compd.* **2024**, *976*, 173220.

[53] M. Khorshidi, S. Asadpour, N. Sarmast, Z. Aramesh-Boroujeni, N. Sadegh, "Enhanced adsorption performance of tetracycline in aqueous solutions using Mg-Al-LDH/AC nanocomposite" *Arab. J. Chem.* **2023**, *16*, 105301.

[54] L. P. Hoang, T. M. P. Nguyen, H. T. Van, M. Yılmaz, T. K. Hoang, Q. T. Nguyen, T. M. H. Vi, L. T. Q. Nga, "Removal of Tetracycline from aqueous solution using composite adsorbent of ZnAl layered double hydroxide and bagasse biochar" *Environ. Technol. Innov.* **2022**, *28*, 102914.

2 MATERIALS AND METHODS

2.1 INSTRUMENTAL SET

2.1.1 X-ray powder diffractometry

The crystallographic analyses in this thesis were carried out by X-ray diffractometry on polycrystalline powders. The technique is based on the ability of materials characterized by a sufficiently high crystalline order to diffract electromagnetic radiation with a suitable wavelength, such as X-rays. The technique is based on the measurement of the intensity of the diffracted radiation as a function of the diffraction angle.

The instrument used is the Bruker D2 Phaser 2nd Generation benchtop diffractometer that uses X-ray emission originating from the electronic collision on a copper target. The radiation selected by the instrument is Kα (1.54 Å). As can be seen in the figure, the instrument consists of three main components: the X-ray source, the sample housing and the detector of the diffracted radiation. In the geometry used (Bragg-Brentano geometry), the source and the detector are mobile along the plane perpendicular to the sample and vary their position with respect to the sample plane by the same angle θ. The incident beam is collimated by a slit before reaching the analyte and a knife is placed above the sample to cut part of the radiation to prevent it from reaching the detector without first being diffracted.

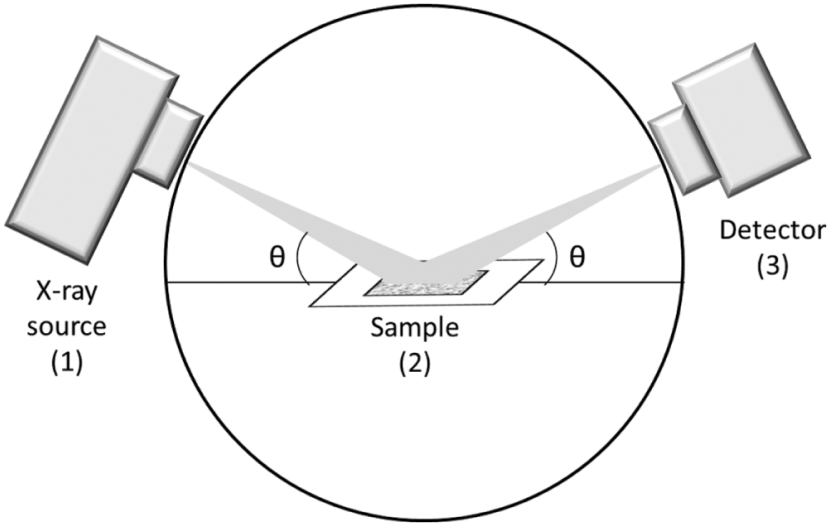

Figure 2. 1 XRD analysis scheme[1]

The result of the analysis consists of a diffractogram in which the intensity of the diffracted light is reported expressed in arbitrary units as a function of the angle 2θ. From the diffraction angle it is then possible, knowing the wavelength λ of the incident radiation and the order n of the diffracted wave, to trace the distance of the two grating points that originate the peak through Bragg's law:

$$n\lambda = 2\,d\sin\theta$$

In the case of LDHs, the most relevant peak series that allows to identify the predominant anion in the interlayer region, is the one corresponding to the planes expressed with Miller indexes (0.0.3) (0.0.6) and (0.0.9). The peak corresponding to the plane (0.0.3), that occur at small angles, is usually the most intense one for each LDH phase and, the distance that can be calculated applying Bragg's law starting from the position of the peak, corresponds to the interlayer distance. For the study conducted in this thesis, is not essential to precisely calculated all the cell parameters, but, for the goal of this work, it's important to know that the basal spacing (*c* cell parameter) is almost three times the interlayer distance, while the metal-metal distance in the layer (*a* cell parameter) can be calculated from the position of the peak associated to the (1.1.0) plane ($a \approx 2\,d_{1.1.0}$)[2].
In the present work, diffractograms in a 2θ range of 1 °- 40 ° with a 0.2 mm slit, a 1 mm knife and a PSD opening of 1.5 and diffractograms in a 2θ range of 5 °- 40 ° and 5° - 80° with a 0.6 mm slit, a 2 mm knife and a PSD opening of 4.5 were recorded.

2.1.2 Atomic emission spectroscopy ICP/OES

To determine the elemental composition of the materials, the Inductively Coupled Plasma/ Optical Emission Spectroscopy (ICP/OES) technique was used. The instrument used was the Avio 200 from Perkin Elmer.

The instrument uses a plasma source to atomize and excite the sample, then analysing the radiation emitted by the excited analyte, thus quantifying the elements that make up the sample. Each element emits a characteristic wavelength that makes it possible to quantify each element without incurring in spectral overlap problems in most cases.

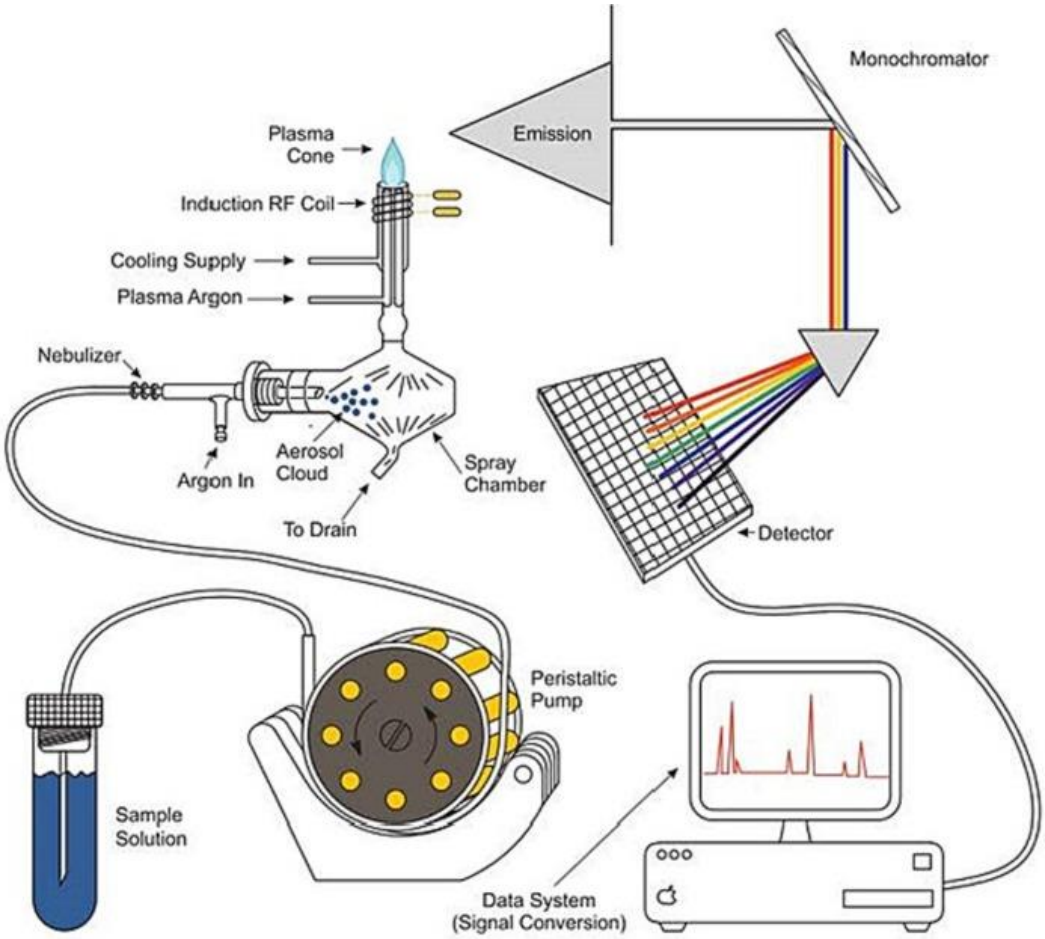

Figure 2. 2 ICP/OES analysis scheme[3]

To determine the Mg/Al and Zn/Al ratios in hydrotalcites, known quantities of sample were first dissolved in 3 mL of HNO_3 and then brought to volume with distilled water, choosing quantities of material and final volume of solution that allowed to have concentrations within the range of the five-point calibration curve created for each metal analysed.

2.1.3 Thermal analysis (TGA and DSC)

Thermogravimetric and calorimetric characterizations were performed by simultaneous analysis with the Perkin Elmer STA 8000 Simultaneous Thermal Analyzer thermobalance.

Thermogravimetric analysis (TGA) is performed by recording the weight of the sample as the temperature varies; this operation can be performed in air or nitrogen, thus eliminating the oxidative processes that occur at high temperatures in the presence of oxygen. The resulting thermogram correlates the weight of the sample (expressed in mg or in percentage weight compared to the initial weight) to the temperature.

Differential thermal analysis (DTA) is performed by recording the difference in temperature (expressed in °C) between the sample and an empty reference crucible as the external temperature varies. The result is expressed by graphing the difference in temperature between the sample and the reference as a function of the external temperature. From this analysis it is possible to distinguish endothermic processes from exothermic ones, since the peaks associated with them are characterized by opposite directions. The instrument used in this work performs a DTA analysis and calculates from the collected data the equivalent result of a differential scanning calorimetry (DSC), hence graphing the results as heat flow between the sample and the reference (mW) as a function of the external temperature. The graphs here reported are have peaks associated to endothermic processes downwards (endo down).

The samples analysed with these techniques were subjected to a temperature ramp of 10 °C/min from 30 °C to 1000 °C.

2.1.4 IR spectroscopy

In this work, part of the chemical-physical characterization of the materials was carried out using a Fourier Transform Infrared Spectrophotometer (FT-IR). Depending on the needs and the type of material that had to be characterized, two techniques were used: attenuated total reflectance IR spectroscopy (FT-IR-ATR) and transmission IR spectroscopy.

In both cases FT/IR-4600 Jasco FT-IR Spectrometer was used.

Both techniques are based on the ability of molecules, to absorb quantized energy necessary to make a jump in the vibrational energetic state of the bonds. The radiations that can give rise to this transition fall in the energy range of infrared radiation. This technique therefore makes it possible to identify the functional groups that characterize a given molecule or material.

The instrument converts the data recorded in the time domain into data in the frequency domain, using a Fourier transform interferometer, which allows to acquire information on the absorbance or transmission of radiation at all wavenumbers at the same time. The result is a spectrum of the absorbed or transmitted radiation intensities expressed in arbitrary units (a.u.) as a function of the wavenumber (cm^{-1}).

In ATR spectroscopy, the sample is placed on an internal reflexion element, which is a high refractive index crystal, usually made of ZnSe or diamond. The incident radiation, after passing through the crystal, penetrates a small thickness of the sample and forms an evanescent wave that, after being

partially absorbed by the sample, results in an attenuated wave that is again reflected by the crystal and sent to the detector. The technique allows the sample to be analysed rapidly without destroying or altering it.

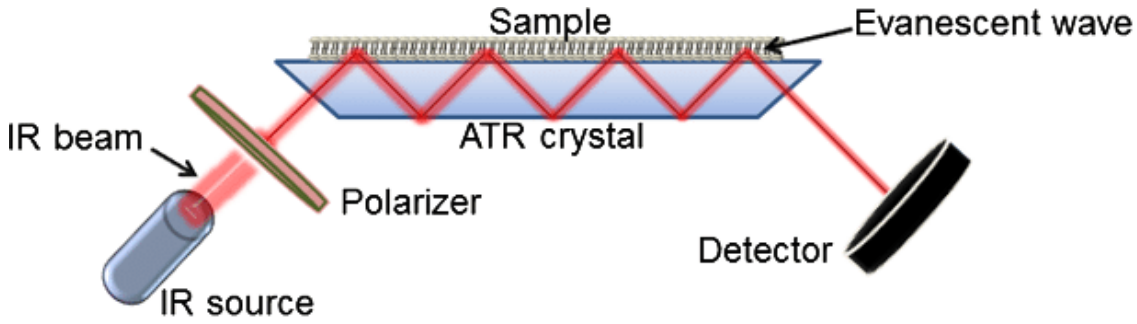

Figure 2. 3 FT-IR ATR analysis scheme[4]

Classical IR spectroscopy instead involves dispersing the analyte in a medium transparent to IR radiation, typically KBr, and creating a pellet that is then hit by IR radiation and the transmitted radiation is collected by the detector. This technique, although it involves more laborious sample preparation, is more sensitive than ATR.

For the analyses performed in this thesis, a ZnSe ATR cell was used and the spectra were collected in an energetic range of 600-4000 cm^{-1}, while the pellets were made in KBr as a dispersing medium, while the analyte was in concentration of 1% or lower; the spectra were collected in an energetic range of 400-4000 cm^{-1}.

2.1.5 UV-VIS spectroscopy

The spectrophotometric determinations in the ultraviolet-visible region were done with the Jasco V-750 UV-vis spectrophotometer.

UV-vis spectroscopy provides information on the electronic energy states of molecules, based on the radiation absorbed by the sample in the range from about 200 to 800 nm. This technique is often used to quantify the analyte, thanks to the linear correlation (Lambert-Beer law) that exists between the concentration of a substance and its absorbance of light radiation at a given wavelength.

The instrument used in this work is a double-beam instrument with a polychromatic source consisting of a deuterium-tungsten lamp, which allows working both in the UV range (deuterium) and in the visible range (tungsten), covering from 190 to 800 nm. The polychromatic light is broken down by a monochromator before being sent to the sample and the reference. The transmitted light

is then transformed into an electrical signal by the detector; the resulting spectrum reports the absorbance (a.u.) as a function of the wavelength (nm).

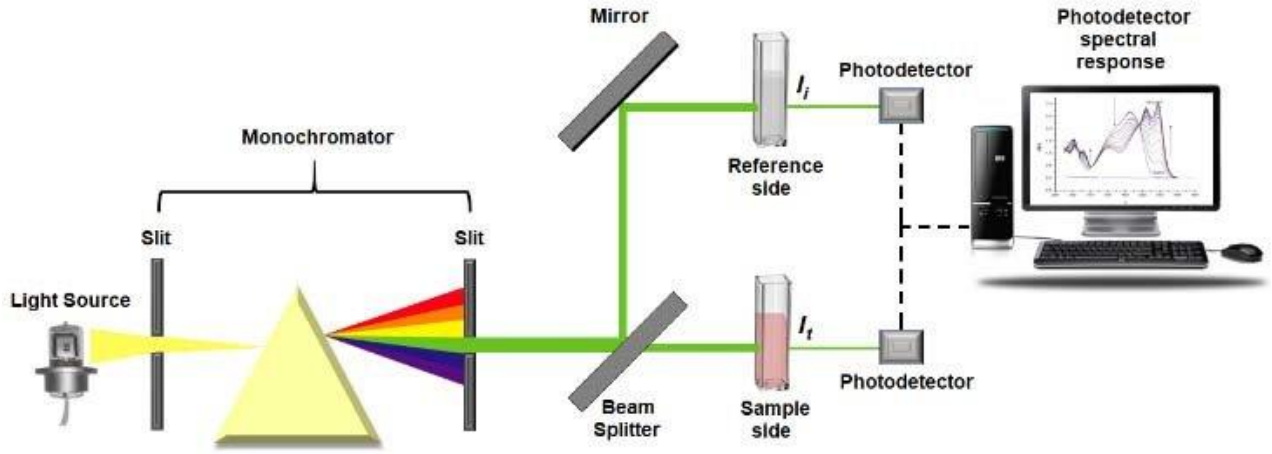

Figure 2. 4 UV-vis spectrometer scheme[5]

The spectra were recorded with quartz cuvettes with an optical path of 1 cm.

2.1.6 Scanning electron microscopy (SEM)

The morphological characterization of the samples was carried out with two scanning electron microscopes: the first, LEO 1525 FE-SEM with Gemini column, is a field emission microscope, with Bruker EDX probe for elemental microanalysis, the second is a ThermoFisher Scientific Phenom ProX benchtop microscope, with CeB_6 source.

All samples were prepared by mounting them on aluminium stubs using a conductive carbon adhesive, blown with compressed air and metallized by ion sputtering with Cr for FE-SEM analyses and with Au for benchtop SEM analyses.

The electro-optical instrument is based on the interaction of an electron beam with the analysed sample. From this interaction, X-ray emissions and different types of electrons are generated: secondary, backscattered, transmitted and Auger electrons. The microscope analyses the first two types listed, the first provides more detailed information on the morphology, while the second is influenced by the structure and relative chemical composition of the analysed sample.

Electrons are generated in the electron column by thermionic effect, they are then accelerated and focused thanks to the use of electronic lenses in the vacuum chamber; the electrons converge on the sample and the emitted signals (X-rays and electrons) are collected by detectors that transfer the information to the processor and then to a screen on which the image is reproduced. The

electron beam is deflected so as to scan the entire surface of the sample, thanks to the use of electromagnetic coils, hence the name “scanning”.

The energy-dispersive X-ray spectroscopy (EDX) gives information on the chemical composition of the sample by analysing the energy of the emitted X-rays.

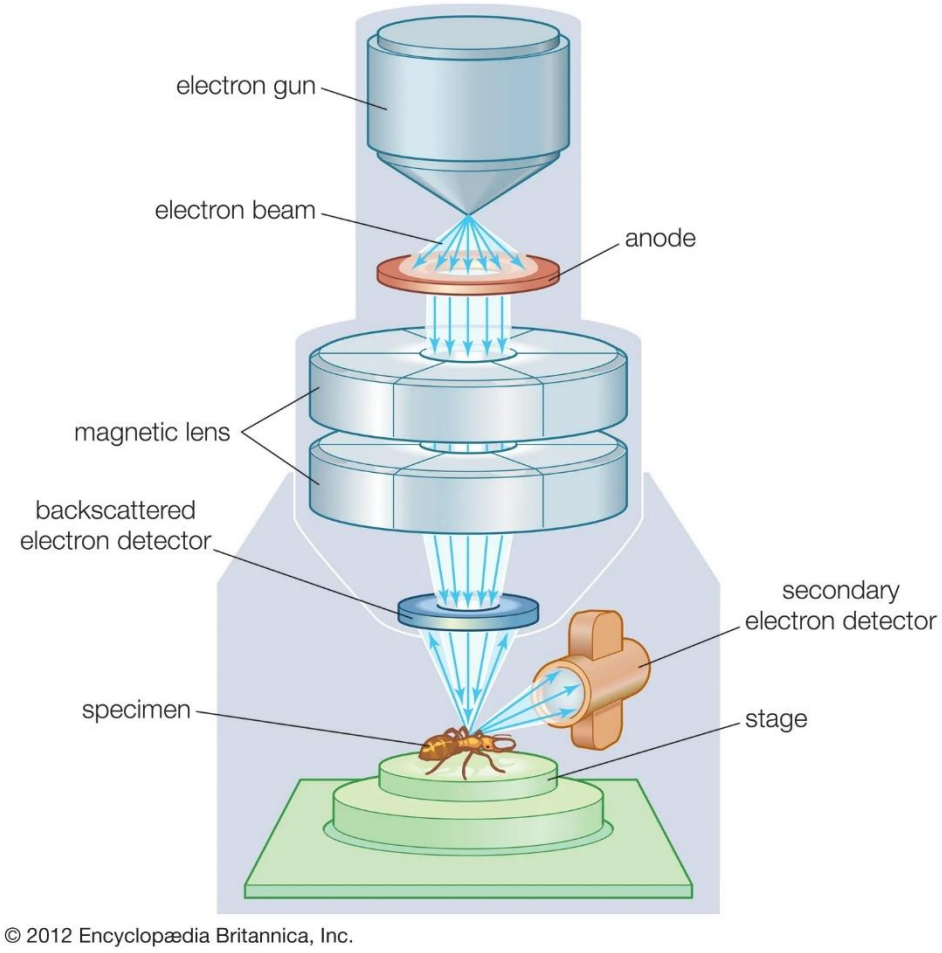

Figure 2. 5 Scanning electron microscope scheme[6]

2.1.7 Surface area analysis with B.E.T. method

Surface area analyses were performed using the Micromeritics Gemini VII Surface Analyzer. The analysed samples (between 100 and 350 mg per sample) were dried at 80°C under a nitrogen flow for three hours before being reweighed and analysed.

The analysis of the surface area according to the Brunauer-Emmett-Teller (B.E.T.) method is based on the surface physical adsorption and desorption of nitrogen by the sample under isothermal conditions at low temperatures (typically 77 K) and specific pressures. Before proceeding with the analysis, it is therefore necessary to dry the sample in a nitrogen flow to prevent impurities, such as water molecules, from being adsorbed on the surface of the material.

The instrument is composed of two gas tanks that, through solenoid valves, allow the passage of gas that is adsorbed in two burettes: the first containing the sample, the second, reference, empty. The gas is made to enter the analysis burette until it reaches a pre-established pressure and, by opening or closing the valve, the instrument regulates the flow of nitrogen necessary to maintain a constant pressure when adsorption occurs. At the same time, the instrument regulates the flow of gas in the reference tube so as to cancel any pressure difference; the quantity of gas adsorbed for each pressure is calculated based on the difference in volume of gas used for the reference burette and the analysis burette.

By analysing the results obtained at multiple pressure points, it is possible to calculate the surface area of the analysed solid.

2.1.8 High performance liquid chromatography HPLC

HPLC analyses were performed using an Agilent 1100 (Santa Clara, CA, USA) series instrument equipped with an auto-sampler, a binary solvent pump, a diode-array detector (DAD) and fluorescence detector (FLD). The separation was achieved with a Kromasil RP C18 (4.6 mm Ø x 150 mm, 5 µm particle size) column.

The technique relies on the different affinity that different molecules have with the stationary phase embedded in the column and the mobile phase: molecules with a higher affinity with the column will be released at higher retention time.

The instrument has three main parts: the injection section, the column and the detector. In the first section the sample is introduced with a syringe in a loop with a well-defined volume, it is then carried by the mobile phase in the column where the separation takes place. The detector can be a mass spectrometer or a UV-vis spectrophotometer, as it is for the instrument used for this thesis.

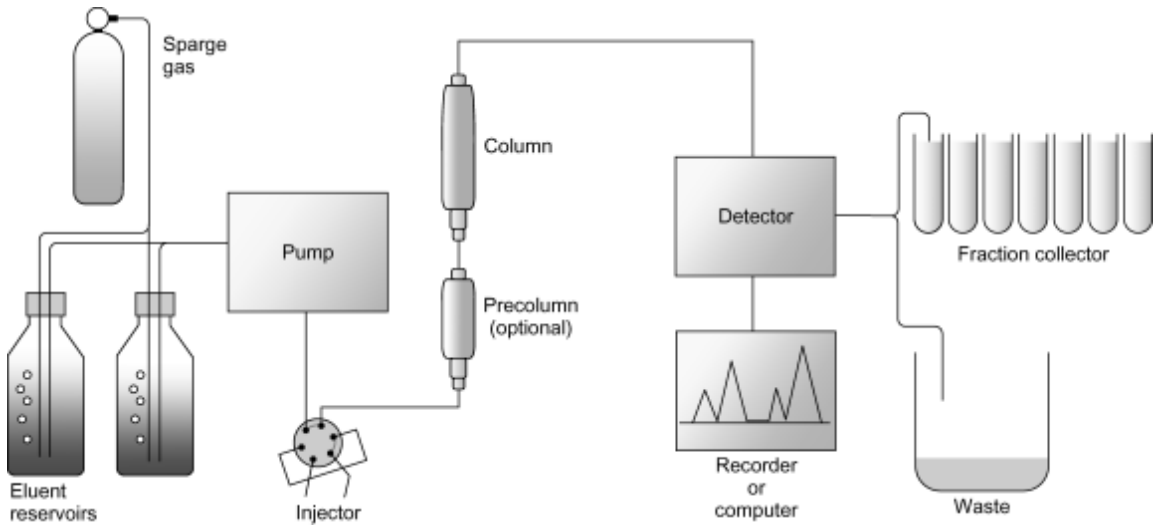

Figure 2. 6 High performance liquid cromatograph scheme[7]

2.2 MATERIALS

2.2.1 Commercial solids

Sipernat 50S and AEROSIL MOX 80 silica were purchase by Evonic (Essen, Germany) and MgO was purchased by Magnesia GmbH (Luneburg, Germany).

2.2.2 Synthesis and modification of LDHs

All the pristine LDHs used in this work as they are or organically modified, were synthesized via urea method, using the urea/(M(II)+M(III)) ratios optimized by Di Michele et al.[8] and by Costantino et al.[9], except for the high surface area MgAl-CO_3 one that was synthetized via co-precipitation method.

All the % yield were calculated considering the composition measured with ICP/OES technique reported in the results chapter and assuming 1 mole of water per mole of LDH.

MgAl-NO_3

The starting LDH, used for the intercalation and extraction studies from the phytoextracts, is made of Mg as divalent metal and Al as trivalent metal, while the interlayer anions are NO_3^-.

1026 g of $Mg(NO_3)_2$*$6H_2O$ (4.0 mol), 639 g of $Al(NO_3)_3$*$9H_2O$ (1.7 mol) and 612 g of urea (10.2 mol) were dissolved in 5.7 L of deionized water in a round bottom flask with a reflux condenser. The reaction mixture was heated and taken in reflux conditions for 48 h after the starting of the precipitation of the material. Once cooled down, the product was filtrated under vacuum with a Büchner funnel, washed three times with deionized water (3.0 L each time) and dried at 50 °C

overnight. The powder was then ground and sifted (100 µm sieve), yielding to 412 g of product, that corresponds to a % yield of 88%.

MgAl-CO_3

The carbonate LDH used for the extraction studies from the phytoextracts and for the antibiotics adsorption studies, is made of Mg as divalent metal and Al as trivalent metal, while the interlayer anions are CO_3^{2-}.

19.80 g of $Mg(NO_3)_2*6H_2O$ (77 mmol), 12.40 g of $Al(NO_3)_3*9H_2O$ (33 mmol) and 19.81 g of urea (330 mmol) were dissolved in 110 mL of deionized water in a round bottom flask with a reflux condenser. The reaction mixture was heated and taken in reflux conditions for 72 h after the starting of the precipitation of the material. Once cooled down, the synthesis mixture was filtrated under vacuum with a Büchner funnel, washed three times with deionized water (20 mL of water each time) and dried at 50 °C overnight. The powder was then ground and sifted (100 µm sieve), yielding to 6.97 g of product, corresponding to a % yield of 78%.

MgAl-Cl

The LDH used for the antibiotics adsorption studies, is made of Mg as divalent metal and Al as trivalent metal, while the interlayer anions are Cl^-.

13.80 g of $MgCl_2*6H_2O$ (68 mmol), 9.10 g of $AlCl_3*6H_2O$ (38 mmol) and 13.50 g of urea (220 mmol) were dissolved in 110 mL of deionized water in a round bottom flask with a reflux condenser. The reaction mixture was heated and taken in reflux conditions for 40h after the starting of the precipitation of the material. Once cooled down, the synthesis mixture was filtrated under vacuum with a Büchner funnel, washed three times with 20 mL of deionized water each time and dried at 50 °C overnight. The powder was then ground and sifted with a 100 µm sieve, with a yield of 6.85 g corresponding to a % yield of 75%.

ZnAl-NO_3

The starting LDH used for the antibiotic adsorption studies is made of Zn as divalent metal and Al as trivalent metal, while the interlayer anions are NO_3^-.

1044 g of $Zn(NO_3)_2*6H_2O$ (3.5 mol), 560 g of $Al(NO_3)_3*9H_2O$ (1.5 mol) and 358 g of urea (6.0 mol) were dissolved in 5.0 L of deionized water in a round bottom flask with a reflux condenser. The reaction mixture was heated and taken in reflux conditions for 24 h after the starting of the

precipitation of the material. Once cooled down, the synthesis mixture was filtrated under vacuum with a Büchner funnel, washed three times with 3.0 L of deionized water each time and dried at 50 °C overnight. The powder was then ground and sifted with a 100 µm sieve, with a yield of 435 g, corresponding to a % yield of 76%.

ZnAl-Cl

The starting LDH used for the antibiotic adsorption studies is made of Zn as divalent metal and Al as trivalent metal, while the interlayer anions are Cl^-.

481 g of $ZnCl_2$ (3.5 mol), 362 g of $AlCl_3*6H_2O$ (1.5 mol) and 360 g of urea (6.0 mol) were dissolved in 5.0 L of deionized water in a round bottom flask with a reflux condenser. The reaction flask was heated and taken in reflux conditions for 24h after the starting of the precipitation of the material. Once cooled down, the synthesis mixture was filtrated under vacuum with a Büchner funnel, washed three times with 3.0 L of deionized water and dried at 50 °C overnight. The powder was then ground and sifted at 100 µm and a yield of 405 g was obtained, corresponding to a % yield of 71%.

MgAl-CO_3 with high surface area

The LDH with high surface area was synthesized via co-precipitation method: the salts of the metals are dissolved in deionized water and a 50% NaOH solution is added under stirring. The increase in pH leads to the fast precipitation of the mixed hydroxide. In this case, after the precipitation the slurry was left open and under stirring for 18 h, then it was centrifuged and dispersed in a concentrated Na_2CO_3 solution for 4 h in order to intercalate the carbonate anion.

577 g of $Mg(NO_3)_2*6H_2O$ (2.3 mol) and 281 g of $Al(NO_3)_3*9H_2O$ (0.75 mol) were dissolved in 3 L of deionized water. 505 g of NaOH 50% in water solution (6.3 mol) were added to the solution under mechanical stirring leading to an increase of the pH up to 10.9.

After 18 h under stirring, the LDH was centrifuged and dispersed in 2 L of a 1 M Na_2CO_3 solution. After 4 h under stirring, the LDH was centrifuged, washed four times, dried at 70 °C, ground and sifted with a 100 µm sieve, with a yield of 222 g (92%).

Organic modification of MgAl-NO_3 LDH

All the organic modifications were performed using MgAl-NO_3 LDH as the substrate; the solid was added to a solution containing the organic acid equivalent to the ion exchange capacity of the LDH

and NaOH equimolar to the acid. The dicarboxylic acids were treated as monoanionic, assuming that only one moiety was deprotonated, in order to leave an acidic site free, in principle, to interact with target molecules. The yields were calculated based on the chemical composition of the starting material determined via ICP as expressed in chapter 3 and considering only monoanionic molecules in the interlayer region in case of functionalization with dicarboxylic acids.

MgAl-oxalate

20.00 g of the nitrate LDH were dispersed in 400 mL of an aqueous solution containing 6.16 g of oxalic acid (68 mmol) and 5.62 g of a NaOH in solution at 50% in weight (70 mmol). The reaction was kept under magnetic stirring for 4 h at room temperature. The slurry was then filtrated under vacuum with a Büchner funnel, washed with deionized water in order to get rid of the non-intercalated organic modifier and dried in oven at 40 °C overnight (100 mL). The dried solid was then ground and sifted at 100 µm, getting 18.53 g of product (85%).

MgAl-malonate

To 400 mL of an aqueous solution containing 7.08 g of malonic acid (68 mmol) and 5.44 g of a NaOH in solution at 50% in weight (68 mmol), 20.00 g of the pristine LDH were added. The reaction was kept under magnetic stirring for 4 h at room temperature. The slurry was then filtrated under vacuum with a Büchner funnel, washed with 100 mL of deionized water, dried in oven at 50 °C overnight, ground and sifted at 100 µm, getting 18.77 g of product (82%).

MgAl-succinate

19.90 g of the pristine LDH were dispersed in 400 mL of an aqueous solution containing 8.03 g of succinic acid (68 mmol) and 5.51 g of a NaOH in solution at 50% in weight (69 mmol). The reaction was kept under magnetic stirring for 4 h at room temperature. The slurry was then filtrated under vacuum on Büchner funnel, washed with 100 mL deionized water, dried in oven at 50 °C overnight, ground and sifted at 100 µm, getting 18.65 g of product (79%).

MgAl-glutarate

20.00 g of the nitrate LDH were dispersed in 400 mL of an aqueous solution containing 8.98 g of glutaric acid (68 mmol) and 5.44 g of a NaOH in solution at 50% in weight (68 mmol). The time, temperature and work-up of the reaction were the same used for the other modifications previously described. The quantity of the collected final product was 19.04 g (77%).

MgAl-adipate

To 400 mL of an aqueous solution containing 9.93 g of adipic acid (68 mmol) and 5.60 g of a NaOH in solution at 50% in weight (70 mmol), obtained heating the solvent in order to facilitate the solubilization of the adipate, 20.00 g of the pristine LDH were added. The time, temperature and work-up of the reaction were the same used for the other modifications previously described. The quantity of the collected final product was 20.57 g (80%).

MgAl-pimelate

To 400 mL of an aqueous solution containing 10.89 g of pimelic acid (68 mmol) and 5.44 g of a NaOH in solution at 50% in weight (68 mmol), obtained heating the solvent in order to facilitate the solubilization of the pimelate, 20.00 g of the pristine LDH were added. The time, temperature and work-up of the reaction were the same used for the other modifications previously described. The yield was of 19.42 g (73%).

MgAl-suberate

To 500 mL of a deionized water/ethanol 80/20 solution containing 11.86 g of suberic acid (68 mmol) and 5.55 g of a NaOH in solution at 50% in weight (69 mmol), obtained heating the solvent in order to facilitate the solubilization of the suberate, 20.05 g of the pristine LDH were added. The time and temperature of the reaction were the same used for the other modifications previously described. To the work-up used for the other materials, a washing step in ethanol (100 mL) was added. The quantity of the collected material was 20.02 g (72%).

MgAl-sebacate

To 500 mL of a deionized water/ethanol 80/20 solution containing 13.75 g of sebacic acid (68 mmol) and 5.54 g of a NaOH in solution at 50% in weight (69 mmol), obtained heating the solvent in order to facilitate the solubilization of the sebacate, 19.90 g of the pristine LDH were added. The time and temperature of the reaction were the same used for the MgAl-suberate LDH; the yield was of 19.78 g (67%).

MgAl-dodecandioate

To 500 mL of a deionized water/ethanol 80/20 solution containing 15.65 g of dodecanoic acid (68 mmol) and 5.63 g of a NaOH in solution at 50% in weight (70 mmol), obtained heating the solvent in order to facilitate the solubilization of the dodecandioate, 20.00 g of the pristine LDH were added.

The time and temperature of the reaction were the same used for MgAl-suberate LDH. The yield was of 19.89 g (63%).

MgAl-pentanoate

An aqueous solution containing 8.67 g of pentanoic acid (84 mmol) and 6.64 g of NaOH in solution at 50% in weight (83 mmol), was made by dissolving the solutes in 450 mL of deionized water. 25.07 g of LDH were added and, after 4 h under magnetic stirring, the slurry was filtrated, washed with 100 mL of deionized water, dried at 50 °C overnight, ground and sifted at 100 μm and a yield of 22.05 g was recorded (78%).

MgAl-nonanoate

The nonanoic acid (10.43 g, 66 mmol) was dissolved and deprotonated in 450 g of deionized water with 5.49 g of a solution of NaOH 50% in weight (69 mmol). After the solubilization, 19.71 g of the nitrate form of the LDH was added and the slurry was kept under magnetic stirring for 4 h. After the reaction, the material was filtrated under vacuum on Büchner funnel, washed with 100 mL of deionized water, dried at 50°C in oven overnight, ground and sifted at 100 μm and a yield of 22.53 g was recorded (87%).

MgAl-azelate reference material

The MgAl LDH functionalised with the azelaic acid, was synthetized before the starting of this work in our laboratories and it was obtained with an ion exchange from a co-precipited MgAl-NO_3 LDH. The choice of the type of synthesis was driven by the ease of scalability on an industrial level of this material; in this work, when it was possible, a higher degree of crystallinity was perused for the synthetized materials, in order to better characterize the materials.

Organic modification of ZnAl-NO_3 LDH

The organic modification was performed using ZnAl-NO_3 LDH as the substrate; the solid was added to a solution containing an excess of sodium acetate. Specifically, 110.66 g of sodium acetate trihydrate (813 mmol) were dissolved in 800 mL of deionized decarbonated water in a capped Erlenmeyer flask and 30.18 g of Zn$AlNO_3$ LDH previously synthetized were added under nitrogen flux to avoid the solubilisation of carbon dioxide in the reaction medium. The dispersion was kept under magnetic stirring for 24 h, then it was centrifuged, washed twice with 300 mL deionized

decarbonated water and dried at 60 °C for two hours. The dried material was then ground and sifted with a 100 µm sieve. 25.13 g of material were collected (84%).

2.2.3 Silica surface modification

A commercial silica was functionalized with azelaic acid as organic surface pendants: in order to do so, a first reaction with aminopropyltriethoxysilane (APTES) was conducted and then the reaction with azelaic acid in presence of 1,1'-carbonyldiimidazole (CDI) and methansulfonic acid resulted in the formation of the amide. The synthesis was conducted by modifying the method reported by Zhang *et al.*[10].

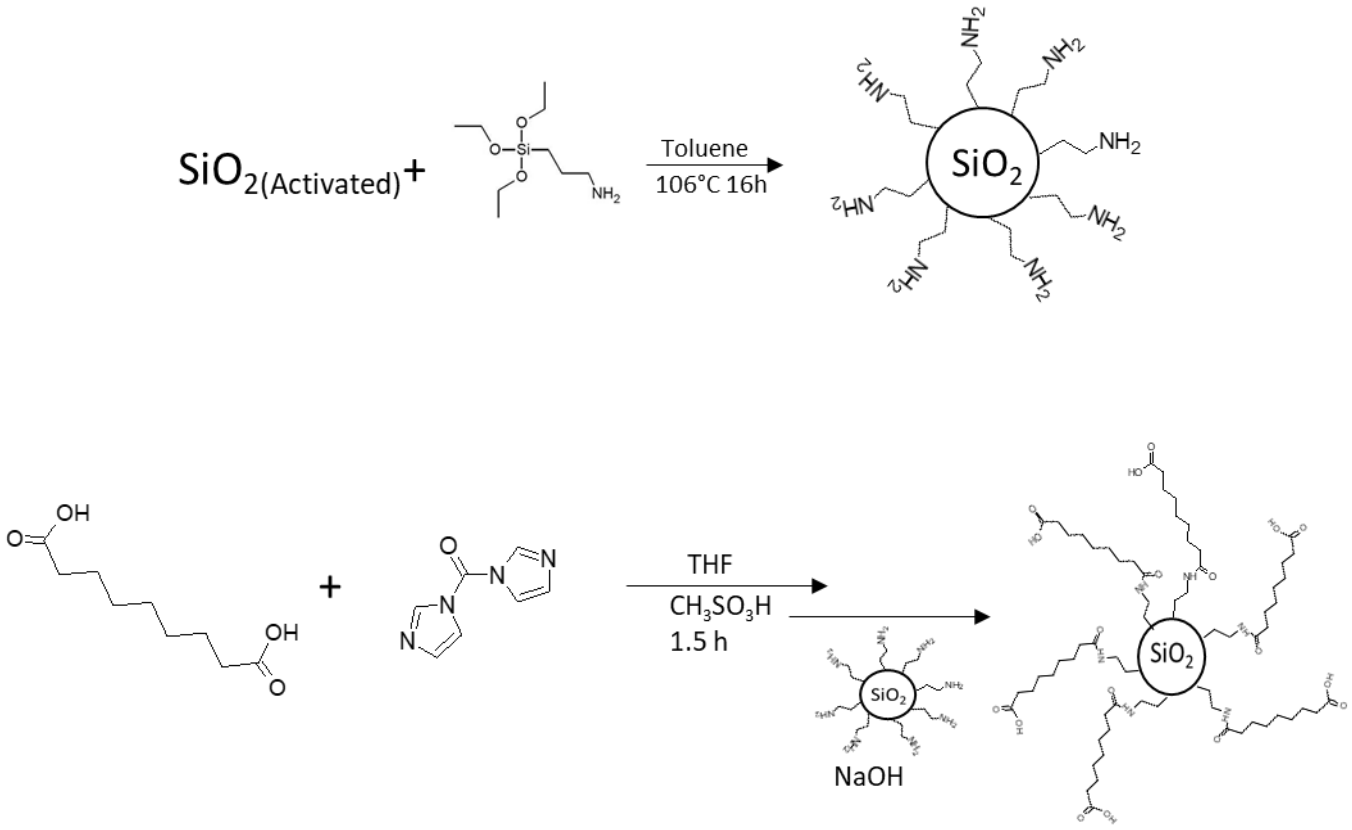

Scheme 2. 1 Reaction scheme of silica surface modification

2.0000 g of commercial silica Sipernat 50S were activated with 100 mL of 37 % HCl in reflux conditions for 4 h in a round bottom flask equipped with a reflux condenser. The material was then filtrated under vacuum with a Büchner funnel and washed until neutrality of the washing water and then dried at 70 °C overnight.

1.0048 g of the resulting silica was dispersed in 10 mL of toluene with 1 mL of APTES (4.0 mmol) and the temperature was raised up to 106 °C with a reflux condenser for 16 h, then it was filtrated,

washed with ethanol, toluene, twice again with ethanol and finally three times with diethyl ether (5 mL of solvent for each step). The material was dried in oven at 50 °C for 6 h, obtaining 1.4704 g.

0.0600 g of azelaic acid (0.3 mmol), 0.0086 g of methanesulfonic acid (0.1 mmol) and 0.0506 g of CDI (0.3 mmol) were dissolved in 200 mL of tetrahydrofuran and, after 1.5 h, 1.0003 g of the APTES-modified silica and 0.0840 g of NaOH (2.1 mmol) were added. After 17 h the material was filtrated, washed with ethanol and dried overnight in oven at 60 °C. 0.6241 g of final product were collected.

2.3 METHODS

2.3.1 Target molecules adsorption from phytoextracts

Aqueous extracts of G*entiana lutea*

The procedure consisted in the microwaves assisted-extraction methodology (40 sec, 600-675 Watt) in water. The experimental protocol concerns the suspension of 1 g of finely triturated dry *G. lutea* leaves in 100 mL of HPLC-grade H_2O followed by filtration.

The resulting solution was divided into 6 aliquots, each made up of 5 mL of the extract, and kept under magnetic stirring for 24 h with 100 mg of one of the solid supports herein under investigation. Each mixture was filtrated under vacuum and centrifuged, analyzing the resulting filtrate by HPLC-DAD analysis at 254 nm, setting the column temperature at 25 °C with an injection volume of 20 µL. The elution was achieved with a mobile phase made of a solution of H_2O/HCOOH 99.6/0.4 as solvent A and of CH_3CN/HCOOH 99.6/0.4 as solvent B; the followed gradient elution program is depicted in table 2.1; the flow rate was 1.0 mL/min, for a total run time of 15 min.

Table 2. 1 Gradient elution program for HPLC analysis of Gentiana lutea extract

Time (min)	A %	B %
0	97	3
3	70	30
9	70	30
12	97	2
15	97	2

The calibration curves were calculated by analyzing pure standard stock solutions at 9 different concentrations ranging between 0.5 and 200 μg/mL. The main analytical parameters determined for the calibration curves are reported in Table 2.2.

Table 2. 2 analytical parameters for the determination of gentiopicroside and amarogentin

	Gentiopicroside	**Amarogentin**
Slope	114112	112397
Intercept	1650	1501
Coefficient of determination (r^2)	0.9997	0.9999
Retention time	5.30 ± 0.02 min	7.90 ± 0.05 min

The percentage of adsorbed molecules was determined as a difference between the starting and the final concentration in solution. The measurements were collected in triplicate.

Methanolic extracts of *G. lutea*

The methanolic extract was obtained by overnight maceration of the finely triturated leaves in methanol. Specifically, 10 g of triturated leaves were added to 120 mL of methanol. After the maceration, the dispersion was filtrated and the solution was dried with a rotary evaporator.

For every material tested, 100 mg or 50 mg of solid were added to 5 mL of aqueous solution obtained solubilizing 50 mg of dried methanolic leaves extract of *G. lutea* according to the experiment. The suspensions were then kept under magnetic stirring for 24 hours, then filtrated and centrifuged. The concentration of the target molecules was determined via HPLC-DAD in the same conditions used to analyze the aqueous extract. The percentage of adsorbed molecules was calculated as a difference between the initial concentration and the resulting one after the contact with the solid. The measurements were collected in triplicate.

Here are reported as an example two HPLC chromatograms of *G. lutea* leaves extract before and after treatment with MgAl-azelate.

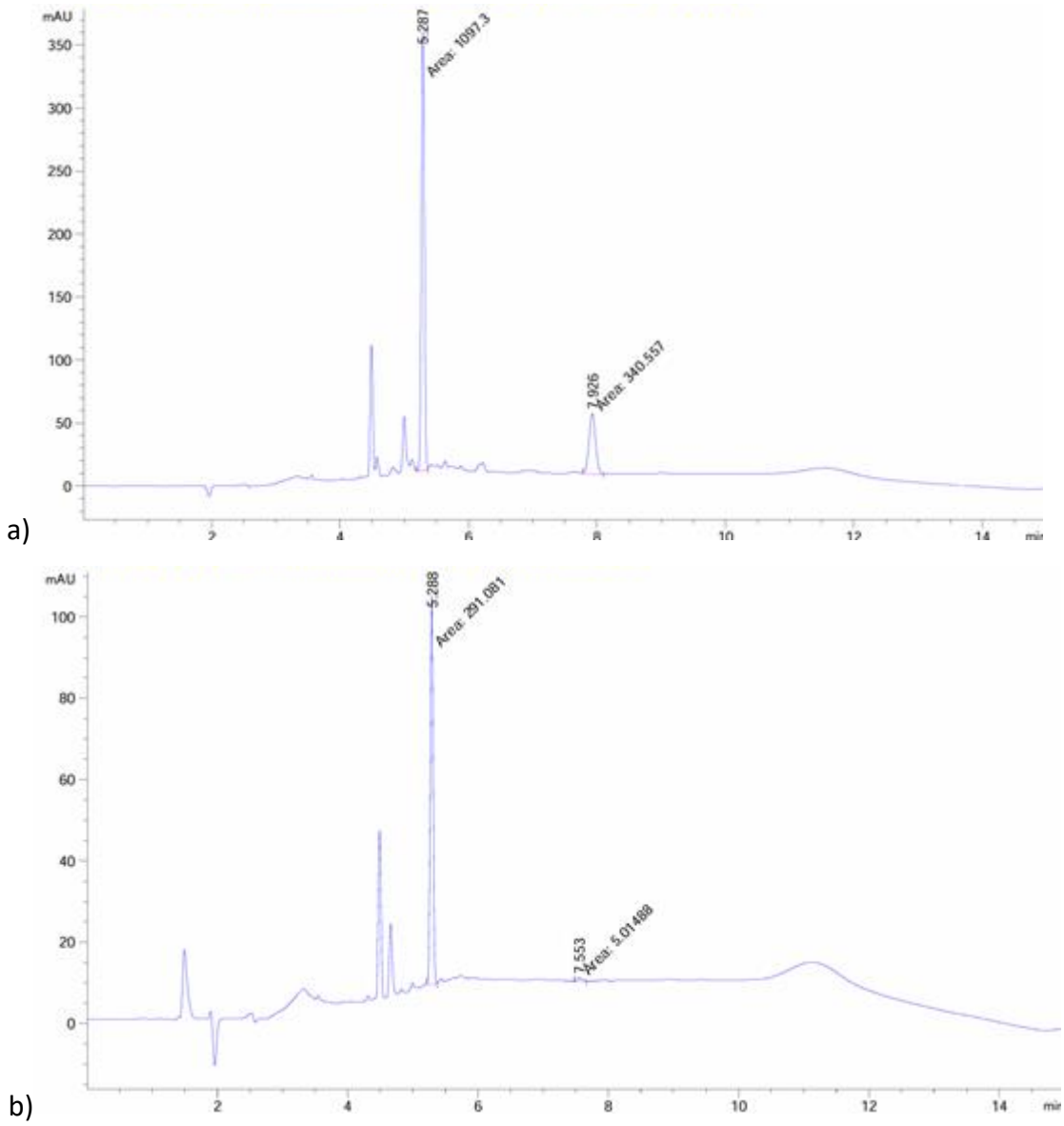

Figure 2. 7 HPLC chromatograms recorded at 254 nm G. lutea leaves extract before (a) and after treatment with MgAl-azelate (b)

The solids that provided the most interesting results were then collected and dried at room temperature in order to further characterize them.

Extract of *P. cuspidatum*

The *P. cuspidatum* extract was obtained by overnight maceration of the finely triturated leaves in methanol. The procedure was the same used for the methanolic extract of the *G. lutea* leaves.

For every material tested, 100 mg of solid was added to 5 mL of aqueous solution obtained solubilizing 50 mg of dried methanolic leaves extract of *P. Cuspidatum*. The suspensions were then kept under magnetic stirring for 24 hours, then filtrated and centrifuged. The concentration of the target molecules was determined via HPLC-DAD, reading the adsorption at 254 nm, setting the column temperature at 25 °C with an injection volume of 20 µL. The elution was achieved with a

mobile phase made of a solution of H_2O/HCOOH 99.6/0.4 as solvent A and of CH_3CN/HCOOH 99.6/0.4 as solvent B; the followed gradient elution program is depicted in Table 2.3, the flow rate was 1.0 mL/min, for a total run time of 40 min. The percentage of adsorbed molecules was calculated as a difference between the initial concentration and the resulting one after the contact with the solid. The measurements were collected in triplicate.

The solids that provided the most promising results were then collected and dried at room temperature in order to further characterize them.

Table 2. 3 Gradient elution program for HPLC analysis of Polygonum cuspidatum extract

Time (min)	A %	B %
0	98	2
3.00	60	40
5.00	60	40
5.01	50	50
38.00	50	50
40.00	98	2

The calibration curves were calculated by analyzing pure standard stock solutions at 9 different concentrations ranging between 0.5 and 100 μg/mL. The main analytical parameters determined for the calibration curves are reported in Table 2.4.

Table 2. 4 Analytical parameters for the determination of emodin and chrysophanol

	Emodin	Chrysophanol
Slope	3130	2491
Intercept	-464	-397
Coefficient of determination (r^2)	0.9992	0.9990
Retention time	15.0 ± 0.2 min	34.2 ± 0.6 min

Here are reported as an example two HPLC chromatograms of *P. cuspidatum* extract before and after treatment with MgAl-CO_3 with high surface area. No great selectivity can be seen in the chromatograms due to the presence in the extract of other anthraquinones with structure similar to emodin and chrysophanol.

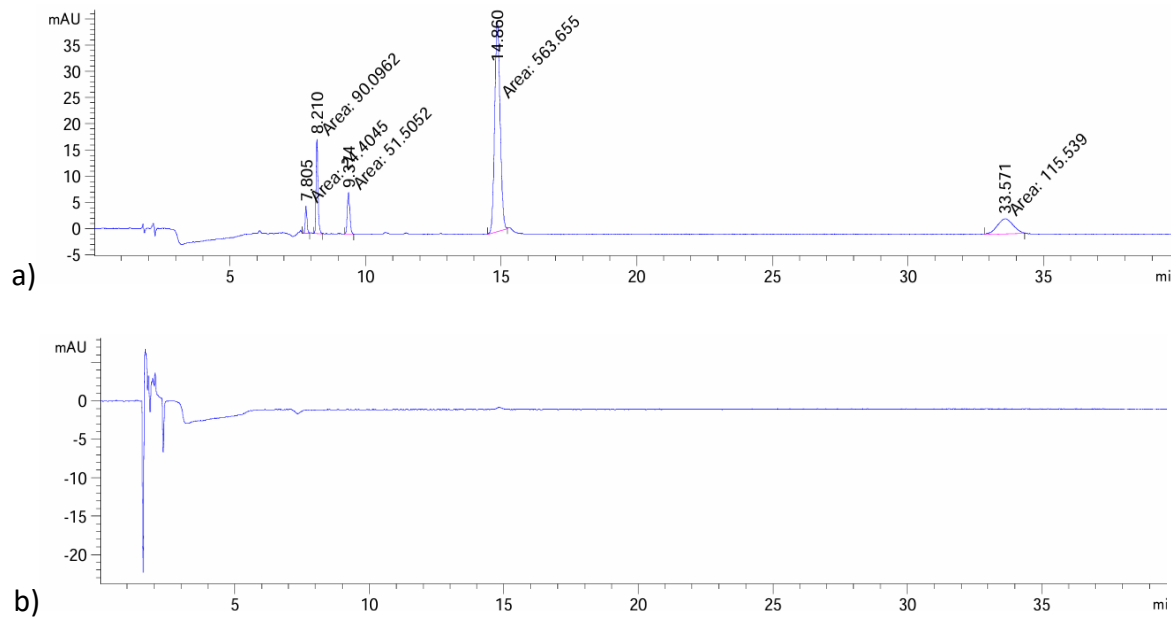

Figure 2. 8 HPLC chromatograms recorded at 254 nm P. cuspidatum extract before (a) and after treatment with MgAl-CO_3 with high surface area (b)

2.3.2 Desorption of target molecules from MgAl-azelate LDH and FT-IR-ATR analysis

The desorption of the adsorbed molecules from the MgAl-azelate LDH was conducted by dispersing 100 mg of the solid in 1 mL of ethanol. The dispersion was kept under magnetic stirring for 48 h and then it was filtrated on syringe polyethylene filter. The resulting solution was then deposited on the FT-IR-ATR ZnSe crystal and the ethanol was let completely evaporate before the analysis.

2.3.3 Antibiotic adsorption studies

The adsorption capacities of SMX on LDHs that could give ion exchange, were evaluated spectrophotometrically. In 100 mL of a 0.2 mg/mL SMX aqueous solution, 400 mg of each tested LDH were dispersed. After 24 hours the dispersion was filtrated with a 50 µm syringe filter, diluted and analyzed with the UV-vis spectrophotometer between 200 nm and 500 nm, evaluating the absorbance at the maximum of the peak (258 nm) and hence calculating the concentration. The measurements were collected in triplicate. The calibration curve was daily calculated on 7 points with SMX solutions prepared every day with absorbance at 258 nm between 0.05 and 1. An example of the most important collected parameters follows.

Table 2. 5 Example of parameters collected for the UV-vis calibration curve

Slope	18277
Intercept	0.0015
Coefficient of determination (r^2)	0.9991

In order to evaluate the effect of the pH, the pH of the starting SMX solution was modified by adding HCl 1 M or NaOH 0.1 M until reaching the desired acidity level monitored via pH-meter (EDGE pH, Hanna instruments).

The kinetic behavior was evaluated without changing the pristine pH, but 1 mL was taken from the dispersion under stirring and analyzed as described before 15, 30, 60, 120, 240, 360, 1440 minutes after the starting of the adsorption process; each kinetic point was determined in triplicate. The XRPD spectra were collected on different solutions 30 minutes, 2 hours and 24 hours after the beginning of the process.

The adsorption capacities of SMX, CPX and TC on solids that could interact via weak forces, were evaluated with HPLC-DAD analysis at 270 nm for sulfamethoxazole, 285 nm for ciprofloxacin, and 350 nm for tetracycline hydrochloride, setting the column temperature at 25 °C with an injection volume of 20 µL. The elution was achieved with a mobile phase made of a solution of H_2O/HCOOH 99.6/0.4 as solvent A and of CH_3CN/HCOOH 99.6/0.4 as solvent B; the followed gradient elution program is depicted in Table 2.6, the total run time was 11 min.

Table 2. 6 Gradient elution program for HPLC analysis of antibiotic solutions

Time (min)	A %	B %	Flow (mL/min)
0	95	5	1
1	95	5	0.6
8	35	65	0.6
10	40	60	1
11	95	5	1

The calibration curves were calculated by analyzing pure standard stock solutions at 12 different concentrations ranging between 0.1 and 125 µM. The main analytical parameters determined for the calibration curves are reported in Table 2.7.

Table 2. 7 Analytical parameters for the determination of SMX, CPX and TC

	SMX	CPX	TC
Slope	52.927	79.483	31.844
Intercept	93.414	82.637	22.514
Coefficient of determination (r^2)	0.9973	0.998	0.999
Retention time	9.44 ± 0.05 min	7.78 ± 0.02 min	7.98 ± 0.02 min

The adsorption of only SMX and only CPX was evaluated by adding for every tested sorbent material 100 mg of the solid in 10 mL (ratio 1:100) or 50 mL (ratio 1:20) of the studied antibiotic solution in concentration 0.1 mg/mL with 0.2 % of acetic acid. The adsorption of TC was evaluated only with a ratio antibiotic / sorbent solid of 1:20.

The adsorption of the mix of the three antibiotics was evaluated by solubilizing 1 mg of each antibiotic in 10 mL of a solution made of 9.9 ml of H_2O + 100 µL of a 20 % acetic acid aqueous solution and adding 100 mg, 200 mg and 300 mg of each tested solid in order to achieve an antibiotic / solid ratio of 1:100, 1:200 and 1:300 for each antibiotic.

The solids were left in the solutions for 24 hours under stirring, then the dispersions were filtrated and centrifuged and the supernatant was analyzed via HPLC-DAD.

The most interesting solids were collected after the contact with the antibiotics solutions and dried at room temperature, in order to perform further characterizations.

BIBLIOGRAPHY

[1] Janice P. L. Kenney, Harish Veeramani, Daniel S. Alessi, Unruh, Daniel K., Tori Z. Forbes, *Analytical Geomicrobiology: A Handbook of Instrumental Techniques*, Cambridge University Press, **2019**.

[2] V. Rives, "Characterisation of layered double hydroxides and their decomposition products" *Mater. Chem. Phys.* **2002**, *75*, 19–25.

[3] C. Douvris, T. Vaughan, D. Bussan, G. Bartzas, R. Thomas, "How ICP-OES changed the face of trace element analysis: Review of the global application landscape" *Sci. Total Environ.* **2023**, *905*, 167242.

[4] Alessio Ausili, Marina Sánchez, Juan C. Gómez-Fernández, "Attenuated total reflectance infrared spectroscopy: A powerful method for the simultaneous study of structure and spatial orientation of lipids and membrane proteins" *Biomed. Spectrosc. Imaging* **2015**, *4*, 159–70.

[5] M. S. Braga, O. F. Gomes, R. F. V. V. Jaimes, E. R. Braga, W. Borysow, W. J. Salcedo Sao Paulo, Brazil, **2019**, pp. 1–6.

[6], "https://www.britannica.com/technology/scanning-electron-microscope" **n.d.**

[7], "https://www.analyticaltoxicology.com/en/high-performance-liquid-chromatography-hplc/" **n.d.**

[8] A. Di Michele, E. Boccalon, F. Costantino, M. Bastianini, R. Vivani, M. Nocchetti, "Insight into the synthesis of LDH using the urea method: morphology and intercalated anion control" *Dalton Trans.* **2024**, *53*, 12543–12553.

[9] U. Costantino, F. Marmottini, M. Nocchetti, R. Vivani, "New Synthetic Routes to Hydrotalcite-Like Compounds − Characterisation and Properties of the Obtained Materials" *Eur. J. Inorg. Chem.* **1998**, *1998*, 1439–1446.

[10] L. Zhang, X. Chang, Z. Hu, L. Zhang, J. Shi, R. Gao, "Selective solid phase extraction and preconcentration of mercury(II) from environmental and biological samples using nanometer silica functionalized by 2,6-pyridine dicarboxylic acid" *Microchim. Acta* **2010**, *168*, 79–85.

3 RESULTS AND DISCUSSION

ADSORPTION OF TARGET MOLECULES FROM PHYTOEXTRACTS

3.1 CHARACTERIZATION OF SYNTHETIZED INORGANIC LDHS

The nitrate form of the MgAl LDH was characterised via XRPD analysis and the exact composition, used to decide the functionalization conditions later on in the work, was determined via ICP-OES.

The XRPD spectrum is here reported.

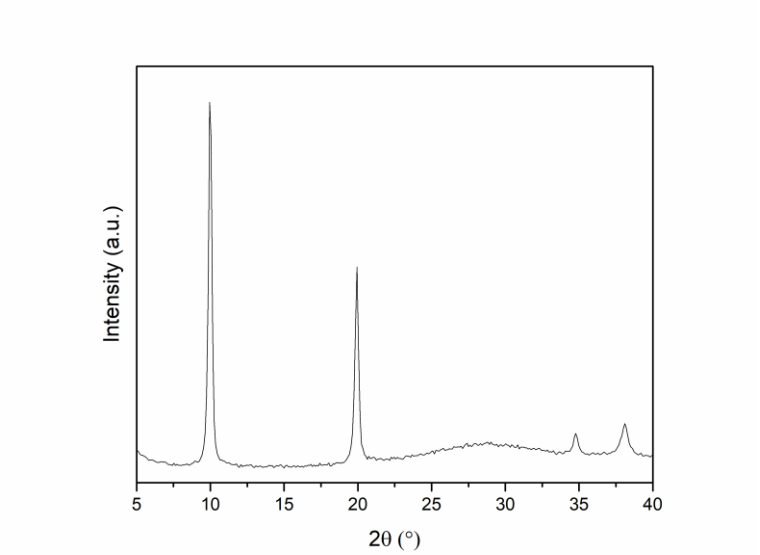

Figure 3. 1 MgAl-NO_3 XRPD pattern

A typical nitrate LDH diffractogram can be observed, with a 2θ of 9.9°, corresponding to an interlayer distance of 8.9 Å, as expected for this kind of material.

The molar fraction of Mg and Al was determined via ICP analysis and the calculated composition was the following: $Mg_{0.64}\ Al_{0.36}\ (NO_3)_{0.36}\ (OH)_2$ * n H_2O. The precise value of n is difficult to determine even with TG analysis, because, apart from the crystallization water molecules, the material tends to adsorb water depending on the air humidity, and the evaporation processes are not separated in TGA, therefore it's difficult to determine the precise formula weight of LDHs. In order to estimate the formula weight, n was considered equal to 1, leading to a FW of 99.58 g/mol. The ion exchange capacity, calculated with the same approximation, is 3.6 mmol/g.

TGA and DSC were also performed on the MgAl-NO_3 LDH to have a reference for the further organic modifications:

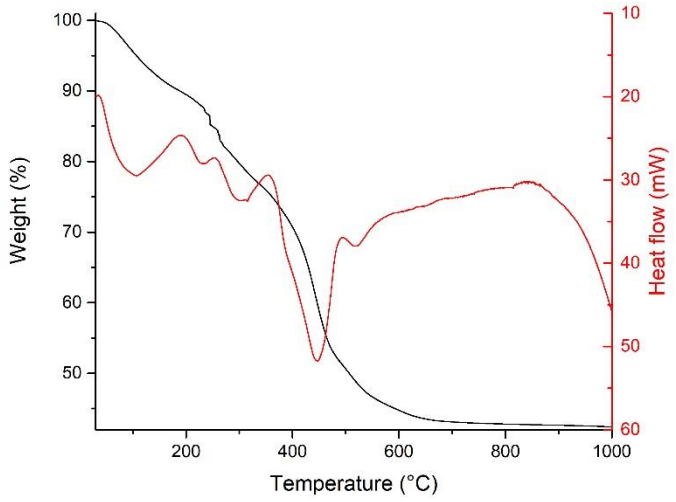

Figure 3. 2 TGA (black line) and DSC (red line) patterns for MgAl-NO_3 LDH

The first weight loss of 10.0% is due to the water content, while the remaining loss (47.5%) takes place during the nitrates decomposition and the OH groups condensation, mainly endothermic processes.

The XRPD analysis was conducted also on the MgAl-CO_3 LDH.

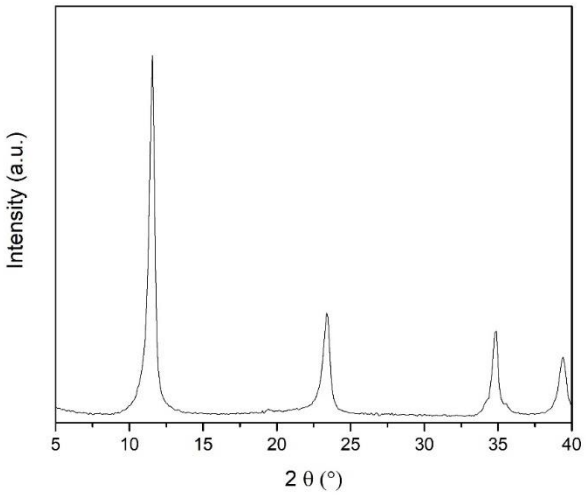

Figure 3. 3 MgAl-CO_3 XRPD pattern

The XRPD spectrum shows the reflections of magnesium aluminium hydroxide carbonate with an interlayer distance of about 7.7 Å.

The BET analysis showed a surface area of 17.10 m^2/g.

The determined composition is the following: $Mg_{0.68}Al_{0.32}$ $(CO_3)_{0.16}(OH)_2$* n H_2O. The precise value of n is difficult to determine even with TG analysis, because, apart from the crystallization water molecules, the material tends to adsorb water depending on the air humidity, therefore it's difficult to determine the precise formula weight of LDHs. In order to estimate the formula weight, n was considered equal to 1, leading to a FW of 86.55 g/mol.

The same characterizations were conducted on the MgAl-CO_3 sample with a high surface area ($MgAlCO_3$ HA).

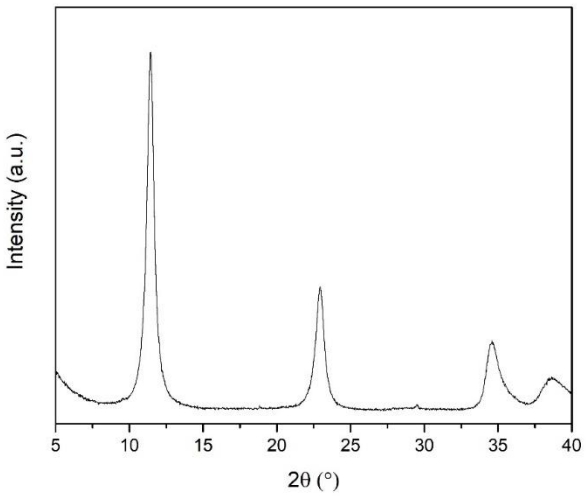

Figure 3. 4 MgAl-CO_3 HA XRPD pattern

The XRD pattern showed an interlayer distance of 7.7 Å, coherent with the presence of the carbonate anions in the interlayer region.

The BET analysis showed a surface area of 72.58 m^2/g.

The molar fraction of Mg and Al was determined via ICP analysis and the calculated composition was the following: $Mg_{0.75}$ $Al_{0.25}$ $(CO_3)_{0.125}$ $(OH)_2$ * n H_2O. The precise value of n is difficult to determine even with TG analysis, because, apart from the crystallization water molecules, the material tends to adsorb water depending on the air humidity, and the evaporation processes are not separated in

TGA, therefore it's difficult to determine the precise formula weight of LDHs. In order to estimate the formula weight, n was considered equal to 1, leading to a FW of 81.25 g/mol.

3.2 CHARACTERIZATION OF ORGANICALLY MODIFIED LDHS

3.2.1 Characterization of deprotonated C_2-C_{12} dicarboxylic acids modified MgAl LDHs

The LDHs obtained modifying the pristine MgAl-NO_3 LDH with the conjugated bases of dicarboxylic acids with various chain lengths (ranging from 2 to 12 carbon atoms), were characterised via XRPD analysis, FT-IR-ATR analysis and TG-DSC analysis. Here are reported also the characterizations performed on the MgAl-azelate used as benchmark, that wasn't synthesized in this work, but was produced in our laboratories.

XRPD characterization

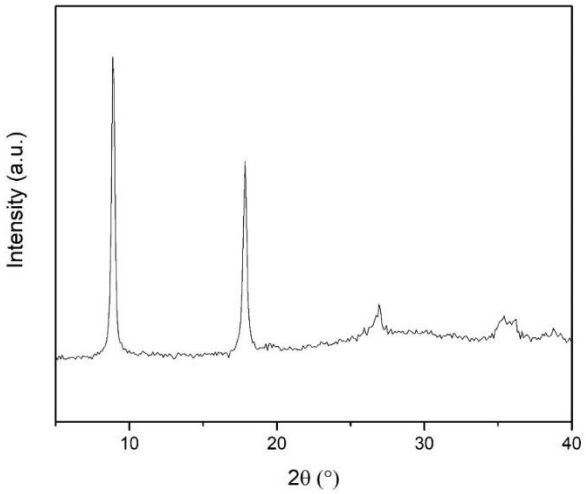

Figure 3. 5 MgAl-oxalate XRPD pattern

After the intercalation of the oxalate anion, the interlayer distance increases to 9.8 Å. In the spectrum the peak associated to the nitrate interlayer distance is no longer detected.

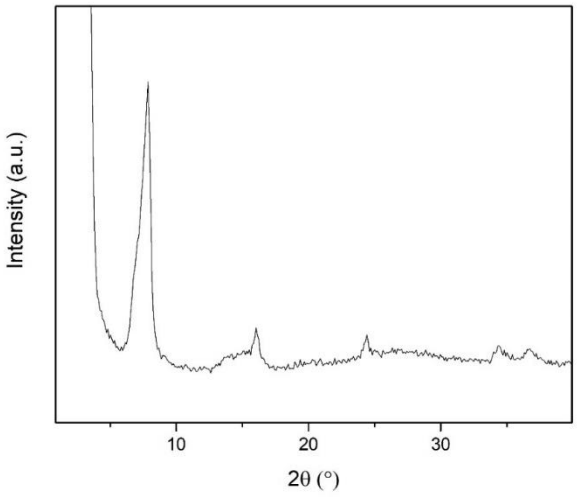

Figure 3. 6 MgAl-malonate XRPD pattern

After the intercalation of the malonate anion, the interlayer distance increases to 11.0 Å.

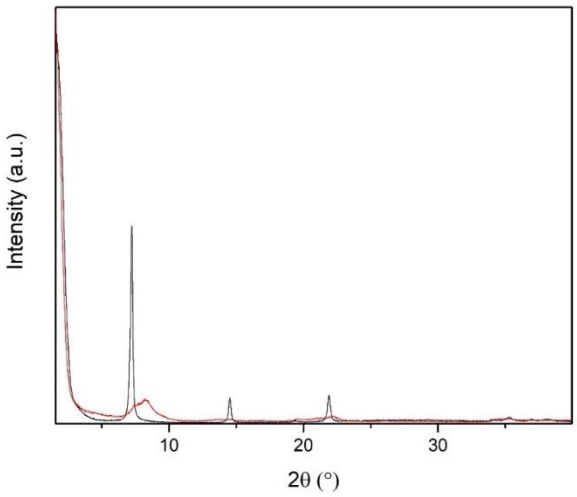

Figure 3. 7 Wet (black line) and dry (red line) MgAl-succinate XRPD pattern

After the intercalation of the succinate anion, the interlayer distance increases to 12.0 Å, but, after the drying process, a peak at 10.7 Å is detected, due to a different arrangement of the anions in the interlayer region after the removal of part of the water molecules. In the spectrum the peak associated to the presence of the nitrate in the interlayer is no longer detected.

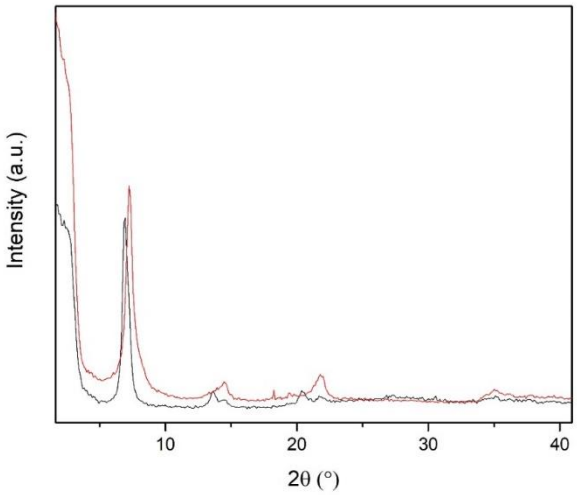

Figure 3. 8 Wet (black line) and dry (red line) MgAl-glutarate XRPD pattern

After the functionalization with the glutarate, the MgAl LDH changes its interlayer distance, that increases to 12.7 Å with a small reduction to 12.1 Å after the drying process.

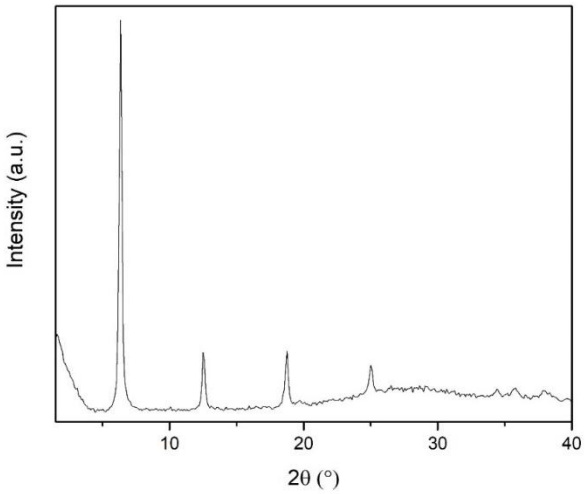

Figure 3. 9 MgAl-adipate XRPD pattern

When the adipate anion is intercalated in the LDH structure, the interlayer distance shifts to 14.2 Å, showing in the XRPD pattern no signal associated to the nitrate phase.

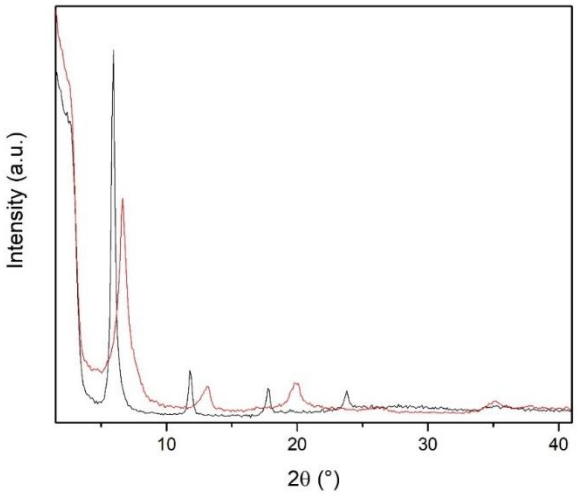

Figure 3. 10 Wet (black line) and dry (red line) MgAl-pimelate XRPD pattern

After the functionalization with the pimelate, the MgAl LDH changes its interlayer distance, that increases to 14.9 Å with a reduction to 13.3 Å after the drying process. No peak associated to the presence of nitrate anions in the interlayer region is detected.

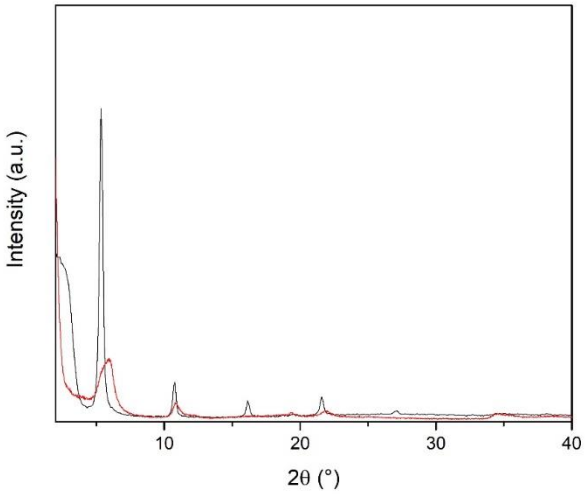

Figure 3. 11 Wet (black line) and dry (red line) MgAl-suberate XRPD pattern

The functionalization with the suberate anion shifts the main diffraction peak to 16.5 Å; after the drying process it is reduced to 15.0 Å. The spectrum doesn't show the presence of nitrate anions in the interlayer region.

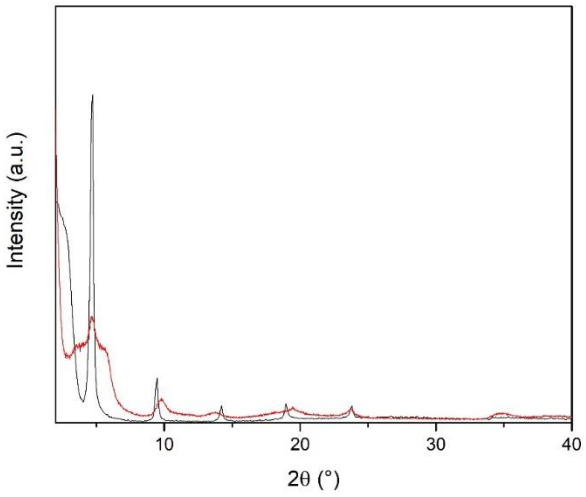

Figure 3. 12 Wet (black line) and dry (red line) MgAl-sebacate XRPD pattern

The functionalization with the sebacate anion shifts the main diffraction peak to 18.8 Å, but, when dried, the material shows two shoulders in the diffraction pattern, the first at 24.7 Å and 15.6 Å. In addition, in this case the nitrate phase is not detected.

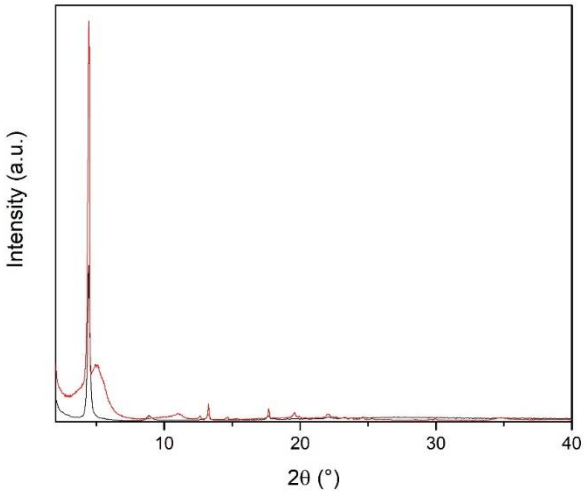

Figure 3. 13 Wet (black line) and dry (red line) MgAl-dodecandioate XRPD pattern

After the intercalation of the dodecandioate anion, the interlayer region of the MgAl LDH increases to 19.9 Å. After drying a new peak can be detected at 17.9 Å. No peak associated to the presence of nitrate anions in the interlayer region is detected.

The formation of a phase with lower interlayer distance after the drying process, is probably due to the evaporation of hydration water molecules that the organic molecules bring in the interlayer region in the first step.

Here is reported a stacking of all the XRD patterns of the wet materials in order to compare them. The spectrum of MgAl-azelate is also reported as a reference, with an interlayer distance of 15.2 Å.

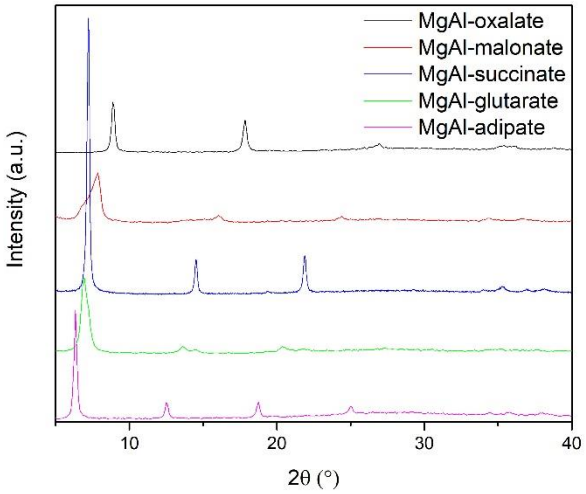

Figure 3. 14 XRPD patterns of wet LDHs organically modified with deprotonated dicarboxylic acids with chain lengths ranging from C_2 to C_6

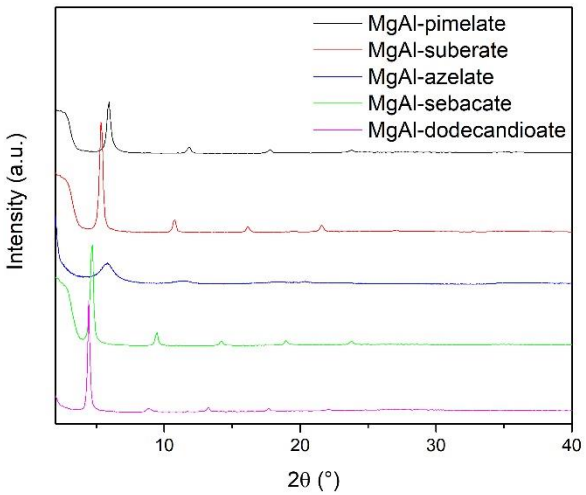

Figure 3. 15 XRPD patterns of wet LDHs organically modified with deprotonated dicarboxylic acids with chain lengths ranging from C_7 to C_{12}

It can be noted that, as expected, increasing the number of carbon atoms that make up the chain, the interlayer distance increases; the only exception is the MgAl-azelate that, being less crystalline, has a broader peak centred at a higher angle than the expected one.

Here are reported all the interlayer distances measured in this work and, for some, the ones reported in literature for the corresponding monocarboxylic acid (the matrix used in the literature reference is a ZnAl LDH, but the different divalent cation likely doesn't affect greatly the basal spacing)[1].

Table 3. 1 Interlayer distances of the organically modified solids and the comparison with the monocarboxylic acids reported in literature

Chain length	Deprotonated dicarboxylic acid main interlayer distance (wet) (Å)	Deprotonated dicarboxylic acid main interlayer distance (dry) (Å)	Deprotonated monocarboxylic acid interlayer distance (literature) (Å)
C2	9.8	9.8	-
C3	11.0	11.0	13.7
C4	12.0	10.7	-
C5	12.7	12.1	15.6
C6	14.2	14.2	-
C7	14.9	13.3	18.2
C8	16.5	15.0	-
C9	-	15.2	-
C10	18.8	18.8 (24.7 and 15.6 new peaks)	21.8
C12	19.9	19.9 (17.9 new peak)	-

The presence of the second carboxylic moiety seem to determine a small and constant shrinkage of the interlayer region compared to what was measured for the monocarboxylic acids.

FT-IR characterization

The IR spectra were performed with the FT-IR-ATR technique: it can be noted that the peak associated with the vibrational energies of the nitrate anions at 1343 cm^{-1}, is not detectable in any of the synthetized materials, meaning that the original interlayer anion has been replaced and its concentration in the solids is lower than approximately 5% wt.

Here are reported the spectra.

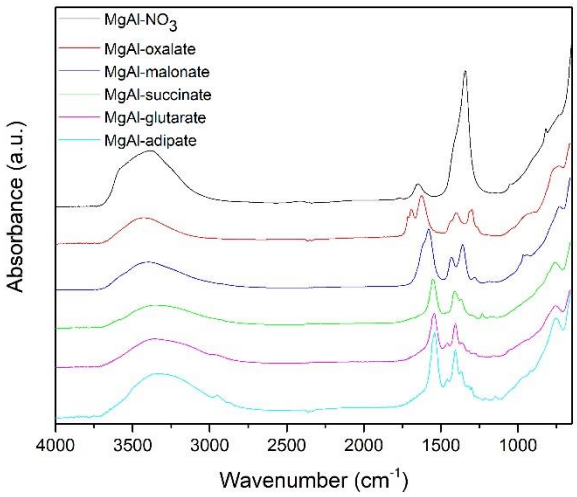

Figure 3. 16 FT-IR-ATR spectra of the LDHs organically modified with deprotonated dicarboxylic acids with chain lengths ranging from C_2 to C_6 and the reference MgAl-NO_3 LDH

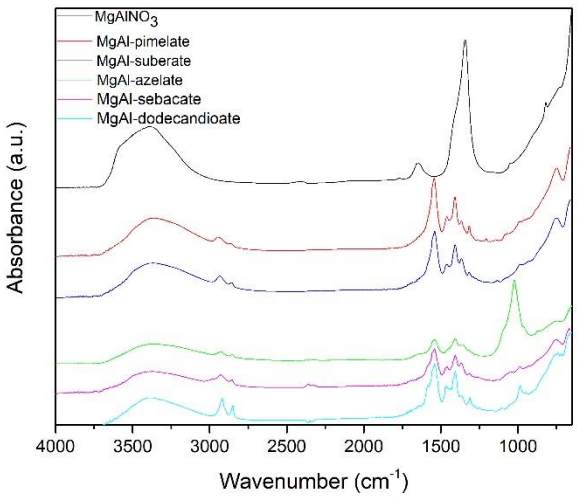

Figure 3. 17 FT-IR-ATR spectra of the LDHs organically modified with deprotonated dicarboxylic acids with chain lengths ranging from C_7 to C_{12} and the reference MgAlNO_3 LDH

Thermogravimetric analysis and differential scanning calorimetry

To determine the percentage of water in the samples and the level of functionalization of the materials, all the LDHs were analysed via TGA-DSC measurements. Due to the possible presence of both monoanionic and dianionic organic acid, it is not possible to precisely calculate the percentage of intercalated organic molecule: for every material is then reported the percentage of weight loss without the percentage of water, that is given by the organic load, the nitrates that might still be in the interlayer region and the condensation of hydroxyl groups.

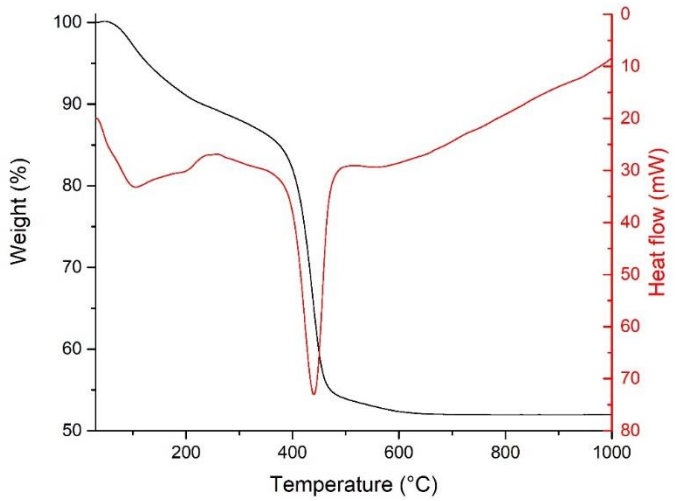

Figure 3. 18 MgAl-oxalate TGA (black line) and DSC (red line) patterns (endo down)

For the material functionalized with the oxalate anion, a total loss of 47.8% of the weight is registered, with a water loss equal to 3.5%: the weight loss without water is 44.3%. The main step is associated to an endothermic process, due to the decomposition of the oxalate. The same behaviour is noted in the analysis of the oxalic acid (Figure 3.19), but, the presence of the inorganic matrix contributes to the increase of the degradation temperature.

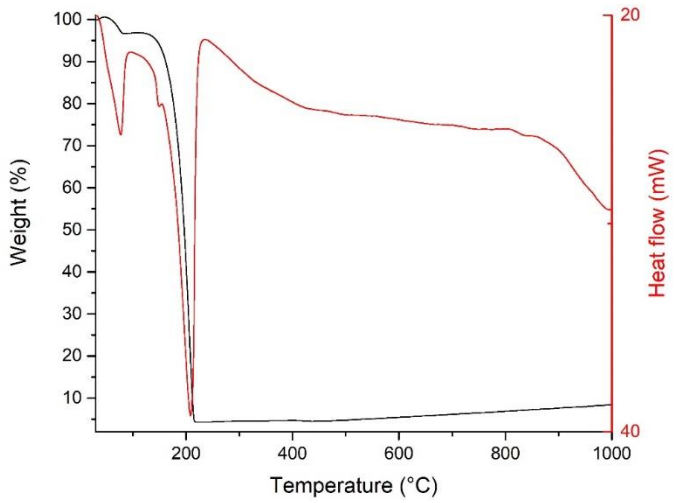

Figure 3. 19 Oxalic acid TGA (black line) and DSC (red line) patterns (endo down)

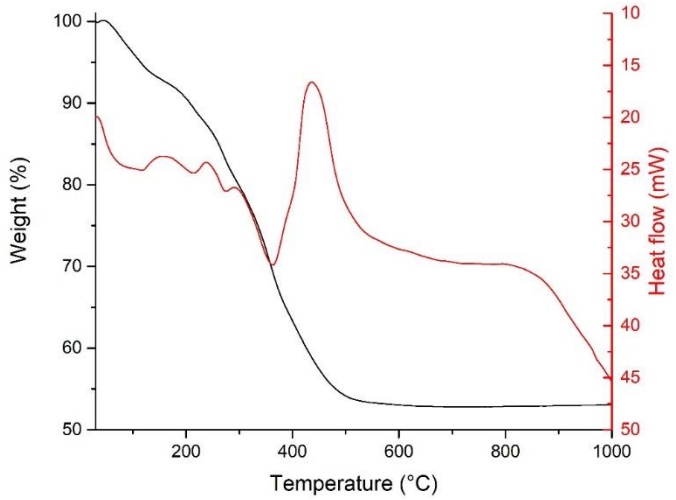

Figure 3. 20 MgAl-malonate TGA (black) and DSC (red) patterns (endo down)

The MgAl-malonate has a total loss of 47.2% and a percentage of water of 8.8%: the weight loss without water is 38.4%. An overlap of different processes can be noted, some of which are endothermic and others exothermic: the decomposition of the malonate is responsible for the first ones: Figure 3.21 shows how the malonic acid undergoes different decomposition steps without any exothermic reaction in absence of the LDH matrix. The exothermic peak that is observed for the LDH might be due to different reaction pathways that take place when the malonate is in the interlayer region.

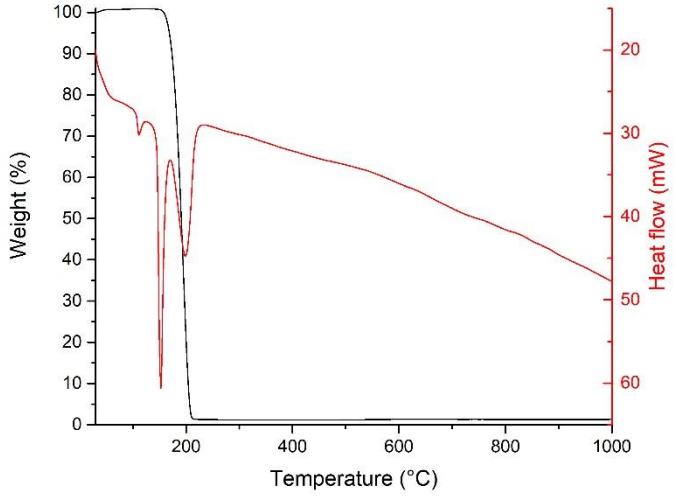

Figure 3. 21 Malonic acid TGA (black line) and DSC (red line) patterns (endo down)

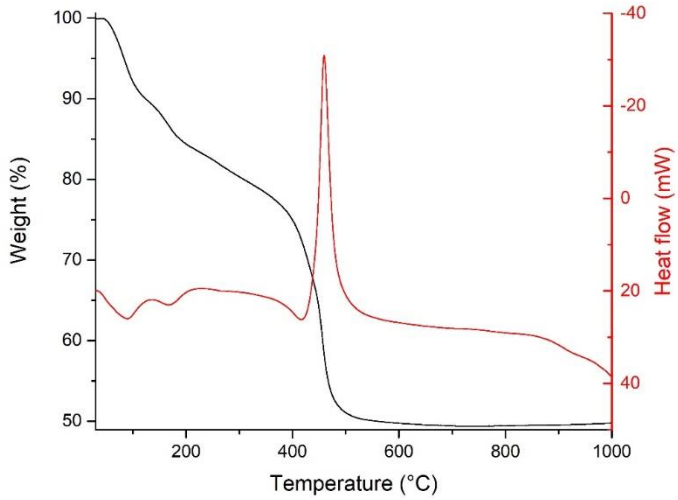

Figure 3. 22 MgAl-succinate TGA (black line) and DSC (red line) patterns (endo down)

A total weight loss of 50.6% is registered for the MgAl-succinate, with a water content of 12.7%: the weight loss without water is 37.9%. The main step is due to the exothermic combustion process.

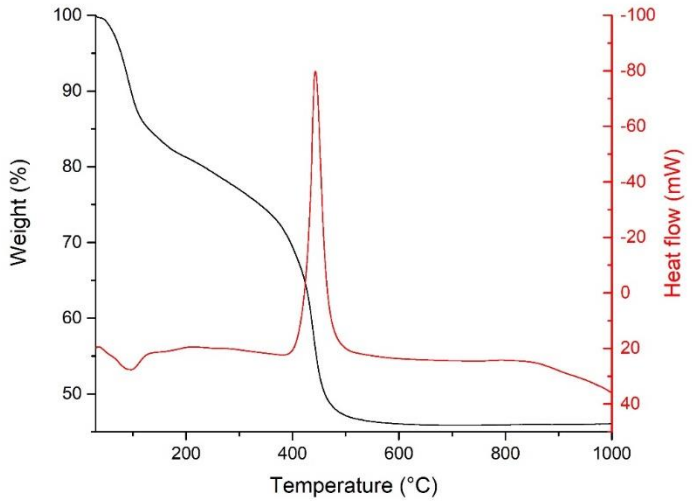

Figure 3. 23 MgAl-glutarate TGA (black line) and DSC (red line) patterns (endo down)

A total weight loss of 54.1% is registered for the MgAl-glutarate LDH, with a water content of 19.1%: the weight loss without water is 35.0%. The main step is due to the exothermic combustion process.

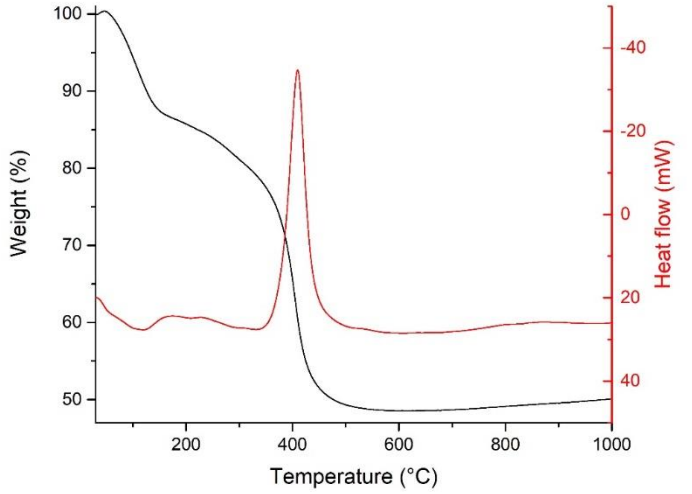

Figure 3. 24 MgAl-adipate TGA (black) and DSC (red) patterns (endo down)

The calculated total weight loss of the MgAl-adipate is 48.5%, with a percentage of water of 12.9% of the total initial weight: the weight loss without water is 35.6%. An exothermic peak is detected corresponding to the main loss step.

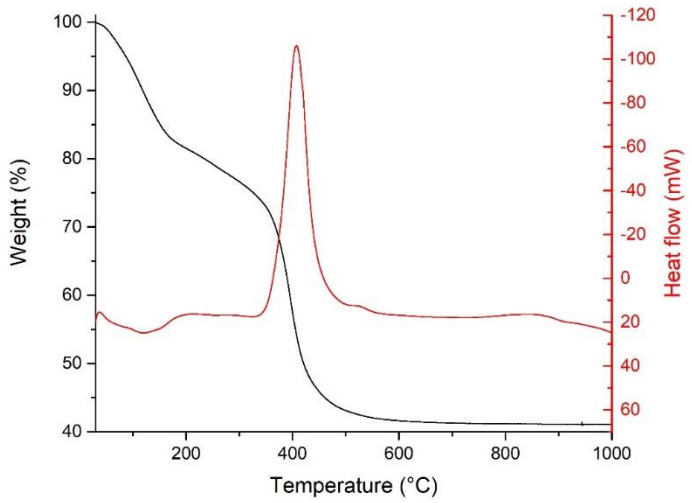

Figure 3. 25 MgAl-pimelate TGA (black) and DSC (red) patterns (endo down)

The total weight loss of the MgAl-pimelate LDH is equal to 59.1%, while the calculated water content is 19.0%: the weight loss without water is 40.1%. The most incisive step is associated to an exothermic process.

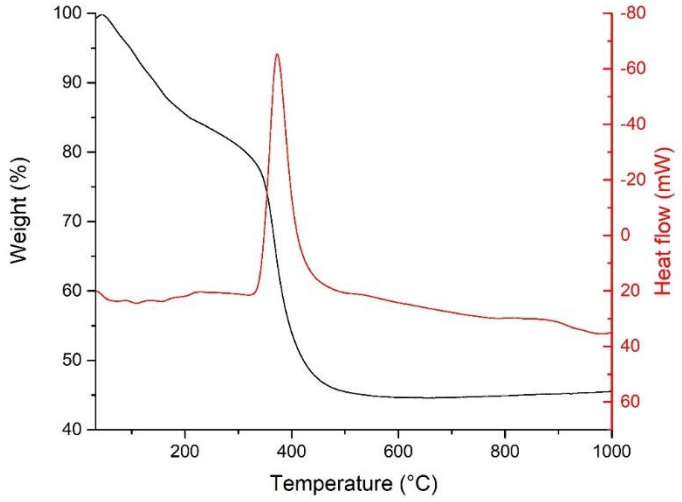

Figure 3. 26 MgAl-subetare TGA (black line) and DSC (red line) patterns (endo down)

Analysing MgAl-suberate LDH, the total weight loss registered is 53.3% with a percentage of water in the solid of 15.2%: the weight loss without water is 38.1%. The combustion of the suberate can be deduced by the presence of an exothermic peak.

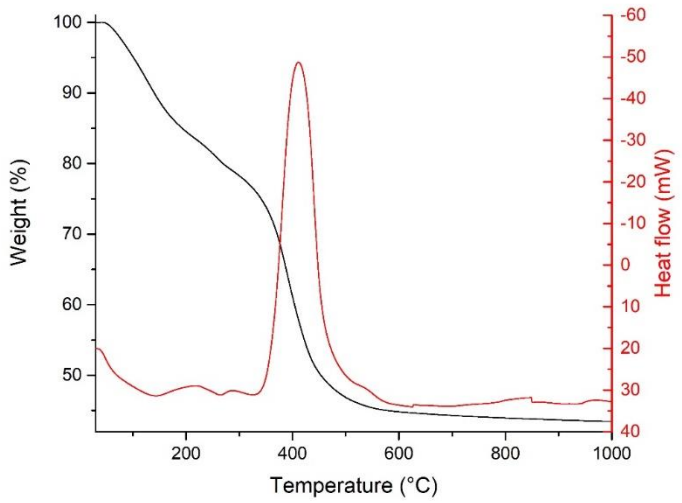

Figure 3. 27 MgAl-azelate TGA (black) and DSC (red) patterns (endo down)

The MgAl-azelate reference LDH has a water content of 15.5%, and a total weight loss of 56.5%: the weight loss without water is 41.1%. Also in this case an exothermic process is correlated to the main gravimetric step, probably the combustion of the azelate anion.

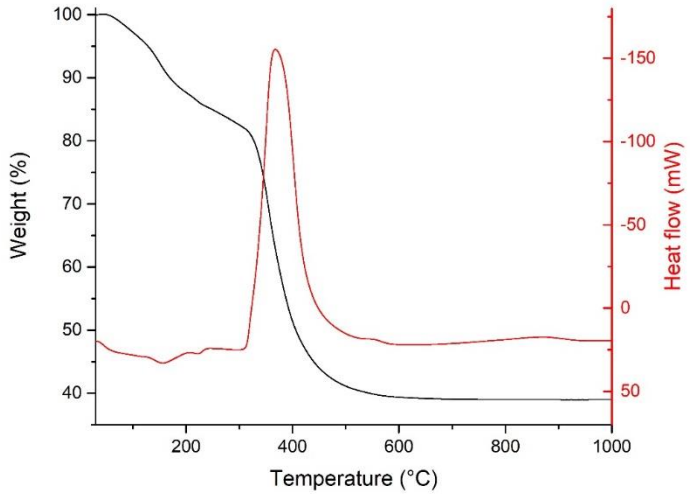

Figure 3. 28 MgAl-sebacate TGA (black line) and DSC (red line) patterns (endo down)

The total weight loss is equal to 60.7%, while the calculated water content is 13.0% for the MgAl-sebacate LDH (weight loss without water is 47.7%). The biggest weight loss is associated to an exothermic process.

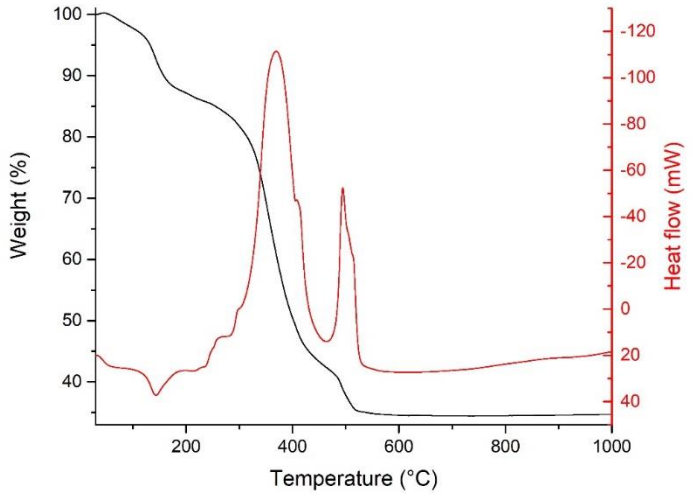

Figure 3. 29 MgAl-dodecandioate TGA (black) and DSC (red) patterns (endo down)

For the MgAl-dodecandioate LDH, a total weight loss of 63% is registered, while the water percentage is 10.4%: the weight loss without water is 52.6%. Two exothermic processes are registered, probably due to the presence of some anions in the interlayer region and others on the surface.

The following table lists the main information given by the TG-DSC analysis for the organically functionalized materials. All the materials have weight losses without water between 35% and 53%.

Table 3. 2 TG analysis results for organically modified materials

Solid	Water content (%)	Weight loss without water (%)
MgAl-oxalate	3.5	44.3
MgAl-malonate	8.8	38.4
MgAl-succinate	12.7	37.9
MgAl-glutarate	19.1	35.0
MgAl-adipate	12.9	35.6
MgAl-pimelate	19.0	40.1
MgAl-suberate	15.2	38.1
MgAl-azelate	15.5	41.0
MgAl-sebacate	13.0	47.7
MgAl-dodecandioate	10.4	52.6

3.2.2 Characterization of deprotonated monocarboxilic acids modified MgAl LDHs

The $MgAlNO_3$ LDH organically modified with pentanoate anion and the one modified with nonanoate anion have been characterized via XRPD, FT-IT-ATR and TG-DSC analysis.

XRPD analysis

From the powder diffraction spectra of the MgAl-pentanoate LDH, an interlayer distance of 15.6 Å is calculated for the wet sample, while, after the drying of the material, the distance increases to 27.1 Å. This change is attributed to a rearrangement of the organic anions after the interlayer solvent molecules have evaporated. No peak associated to the phase with the nitrate in the interlayer region is detected.

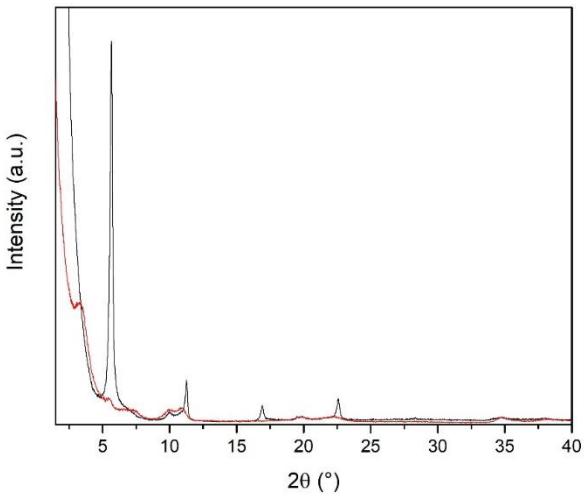

Figure 3. 30 Wet (black line) and dry (red line) MgAl-pentanoate XRPD pattern

A similar behaviour is observed for the MgAl-nonanoate LDH, where the interlayer distance increases from 20.7 Å to 28.9 Å. Also in this case no peak associated to the phase with the nitrate in the interlayer region is detected.

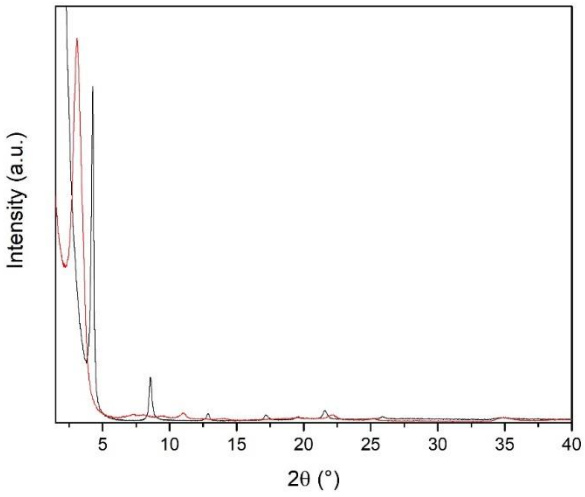

Figure 3. 31 Wet (black line) and dry (red line) MgAl-nonanoate XRPD pattern

FTIR-ATR analysis

The IR spectra collected with the FT-IR-ATR technique, show that the peak associated to the nitrate vibrational movements at 1343 cm^{-1} is not detected in any of the prepared materials, meaning that the nitrate anion is less than 5% in weight of the solid. The spectra are reported in the following figure.

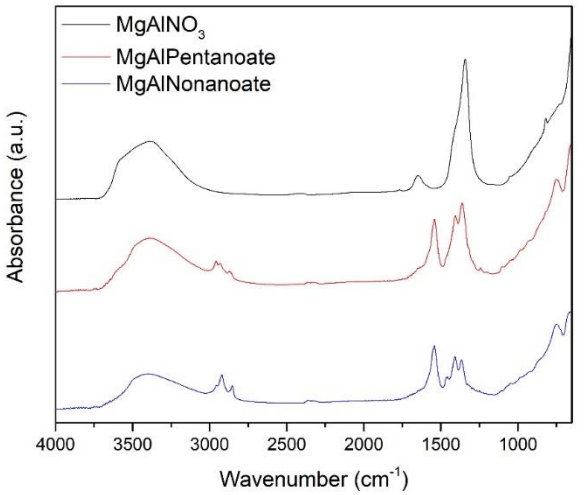

Figure 3. 32 FT-IR-ATR spectra of the LDHs organically modified with carboxylic acids with chain lengths C5 and C8 and the reference MgAl-NO_3 LDH

TGA-DSC

The TGA shows a weight loss associated to the water content equal to 11.0% and a total weight loss of 53.7% for the MgAl-pentanoate LDH. The main loss corresponds to an exothermic process, probably the organic molecule combustion. The percentage of intercalated organic molecule, calculated by considering the charge and mass balance of nitrate anions and carboxylate anions, is of 8.9%.

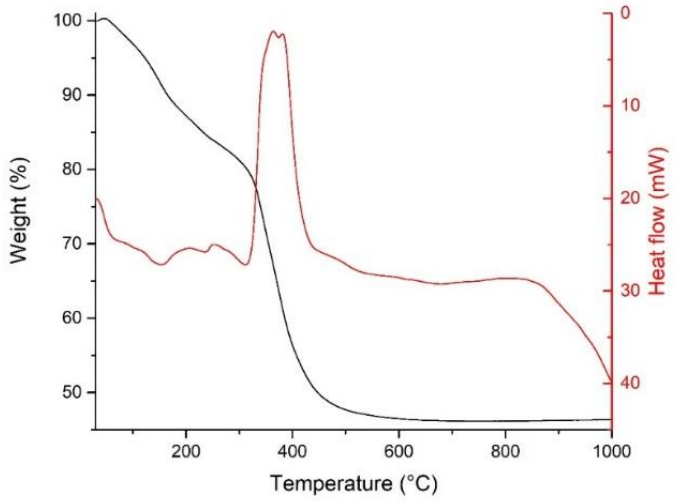

Figure 3. 33 MgAl-pentanoate TGA (black) and DSC (red) patterns (endo down)

The same considerations can be made for the MgAl-nonanoate LDH, but in this case the water content is equal to 10.2% and the total weight loss is 62.3%. The calculated percentage of intercalated organic molecule is of 33.2%

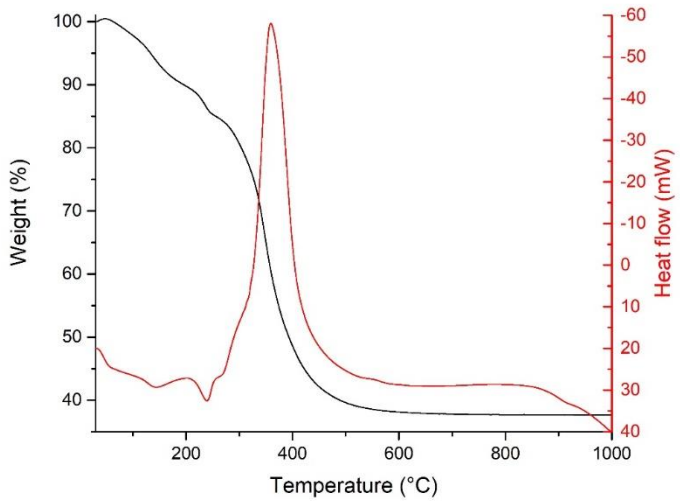

Figure 3. 34 MgAl-nonanoate TGA (black) and DSC (red) patterns (endo down)

3.2.3 Characterization of modified silica

The modified commercial silica (Sipernat 50S) was characterized after every synthetic step via thermogravimetric analysis and FT-IR. The IR was performed on two different concentrations of solid in the KBr tablet in order to have generic information on the solid and more accurate information on the organic group modifications.

FT-IR

The IR spectra of the starting silica (SiO_2), of the APTES functionalised silica (APTES-SiO_2) and of the azelate-APTES functionalised silica (AZ-APTES-SiO_2) were collected.

Here are reported all the three normalized spectra.

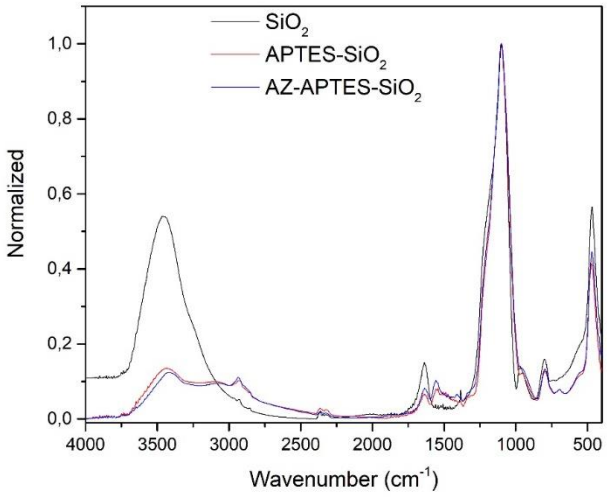

Figure 3. 35 IR spectra of pristine silica (black), APTES modified silica (red) and azelate-APTES modified silica (blue)

There are some major modifications in the spectra in the region between 1400 cm^{-1} and 1800 cm^{-1}. In particular, some signals are detected for the organically modified materials, that are not detected for the pristine silica. In order to better analyse the materials, a more concentrated tablet was analysed for both the samples, focusing the attention in the previously highlighted region. It can be observed that, after the reaction with the azelate, the peak at 1490 cm^{-1}, one of the two associated to the N-H bond stretching[2], is not detectable anymore, confirming the successful amidation reaction.

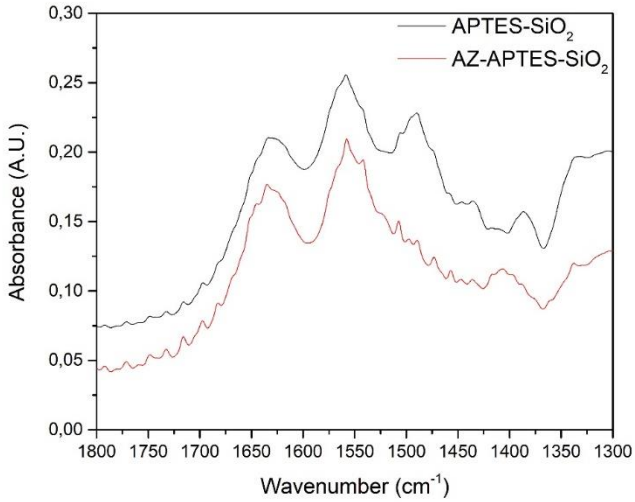

Figure 3. 36 IR spectra of APTES modified silica (black) and azelate-APTES modified silica (red)

TGA-DSC

The APTES functionalised silica is characterized by a total weight loss of 14.1 % and a percentage of solvent equal to 0.7 %, leading to a percentage of organic functionalizing agent equal to 13.4 %.

The DSC shows a first endothermic step (solvent evaporation step), followed by many overlapped exothermic steps, due to the propyl amine combustion.

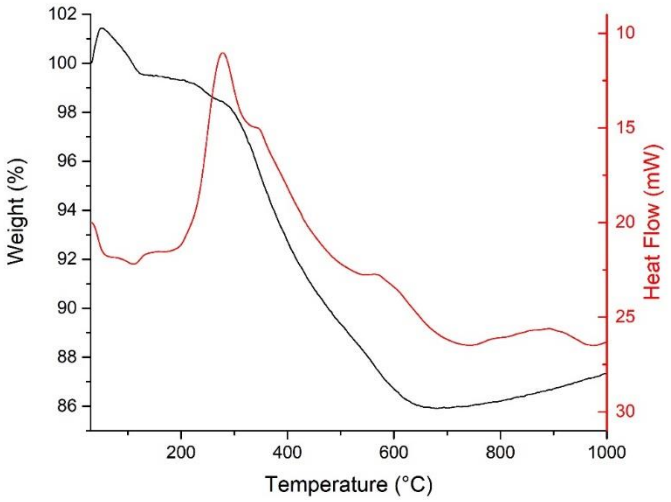

Figure 3. 37 APTES modified silica TGA (black) and DSC (red) patterns (endo down)

After the reaction with the azelaic acid, the total weight loss of the material increases to 18.7 %, with a percentage of solvent of 0.8% and a 17.9% of organic modifier.

Also in this case the DSC shows a first endothermic step caused by the solvent evaporation process, followed by the combustion of the organic molecules that originates the exothermic peaks.

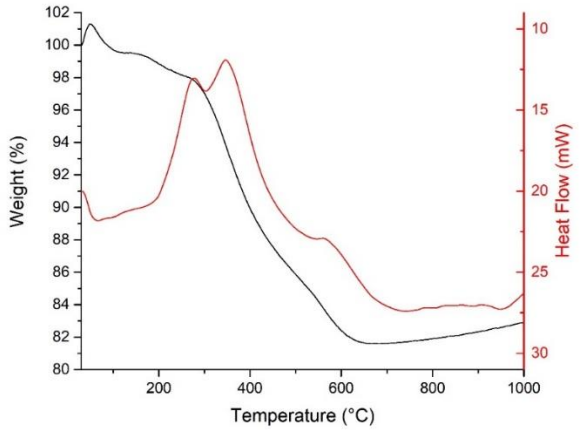

Figure 3. 38 Azelate-APTES modified silica TGA (black) and DSC (red) patterns (endo down)

By comparing the organic modifier quantity in both materials, a percentage of azelate of 4.5 % can be calculated for the final material.

3.3 EXTRACTION OF GENTIOPICROSIDE AND AMAROGENTIN FROM *GENTIANA LUTEA*

The experiments were performed with two types of extract, a methanolic one and an aqueous MW-assisted one, obtained as described in materials and methods chapter. The quantities of gentiopicroside and amarogentin in milligram per gram of dry extract determined via HLPC-DAD and expressed as mean value ± SD for every extraction method are reported in Table 3.3.

Table 3. 3 Quantification of gentiopicroside and amarogentin per gram of dry extract of G. lutea depending on the extraction method

Method of extraction	**Extractive yield (mg/g)**	
	Gentiopicroside	**Amarogentin**
MeOH maceration	70.5 ± 0.1	20.6 ± 0.1
Microwave-assisted (H_2O)	168.8 ± 0.1	72.1 ± 0.1

3.3.1 Effect of the intercalated conjugated bases of dicarboxylic acids chain length

In order to better understand the causes of the very good adsorption capacity of gentiopicroside and amarogentin shown by the LDH MgAl-azelate in previous studies, the adsorption capacity of the target molecules of the LDHs series with conjugated bases of dicarboxylic acids with variable chain length as intercalated anion was evaluated.

The experiments were performed as previously described in material and methods chapter, on aqueous *G. lutea* extract obtained via microwave assisted extraction conducted on the plant leaves. This extraction method allows to have a lower impact on the plant, not concerning the complete eradication in order to get the roots. It is moreover a greener approach thanks to the use of water as extraction solvent, avoiding the use of other organic solvents.

The adsorption capacity of each solid was evaluated determining via HPLC after filtration of the solid the amount of residual gentiopicroside and amarogentin in the extract and calculating the adsorbed percentage of target molecules by subtracting the concentration of each secondary metabolite in the filtrate from the content of the same molecule in the blank original solution of plant extract.

Performing the adsorption tests on the synthesised solids, the following values were recorded (Table 3.4).

Table 3. 4 Quantitative determination of gentiopicroside and amarogentin (values expressed as percentages ± SD) from leaf aqueous extracts of G. lutea adsorbed onto the solid sorbents under investigation

Sample entry	Gentiopicroside	Amarogentin
	% ± SD	% ± SD
MgAl-oxalate	30.1 ± 0.1	87.4 ± 0.1
MgAl-malonate	40.1 ± 0.1	92.5 ± 0.1
MgAl-succinate	42.9 ± 0.1	97.6 ± 0.1
MgAl-glutarate	43.1 ± 0.1	94.7 ± 0.2
MgAl-adipate	46.5 ± 0.1	98.1 ± 0.1
MgAl-pimelate	43.8 ± 0.1	97.5 ± 0.1
MgAl-suberate	44.4 ± 0.1	98.8 ± 0.1
MgAl-azelate	43.3 ± 0.1	97.8 ± 0.1
MgAl-sebacate	52.2 ± 0.1	98.6 ± 0.1
MgAl-dodecandioate	44.7 ± 0.1	98.0 ± 0.1

For a greater completeness of the present study, we repeated the same experiments increasing the amount of two of the sorbent solids (MgAl-sebacate and MgAl-malonate) with the same quantity of extract, in order to evaluate if the adsorption capacity may increase for gentiopicroside. Results are reported in Table 3.5.

Table 3. 5 Effect of sorbent loading on gentiopicroside and amarogentin adsorptions

Sample entry	Gentiopicroside	Amarogentin
	% ± SD	% ± SD
MgAl-sebacate (100 mg)	52.2 ± 0.1	98.6 ± 0.1
MgAl-sebacate (150 mg)	55.9 ± 0.1	98.7 ± 0.1
MgAl-sebacate (200 mg)	60.6 ± 0.1	98.7 ± 0.1
MgAl-malonate (100 mg)	40.1 ± 0.1	92.5 ± 0.1
MgAl-malonate (150 mg)	40.1 ± 0.1	97.7 ± 0.1
MgAl-malonate (200 mg)	42.4 ± 0.1	97.9 ± 0.1

Discussing about the optimization of the extraction process, the amount obtained by aqueous MW-extraction was 149.2 ± 0.7 and 19.9 ± 0.4 µg/mL for gentiopicroside and amarogentin respectively, spending less time, without the use of organic extraction solvent and having the water solution ready for the subsequent treatment.

For all tested sorbents, the same pattern of results in terms of extractive yields and selectivity have been achieved after the treatment with the already tested MgAl-azelate, and the new ones Magnesium Aluminium based clays characterized by the presence of deprotonated dicarboxylic acids with a carbon chain length in the range of C_2–C_{12} as the exchangeable organic anions which balances the positive charge of the layer.

All solids exhibited a higher capacity to retain amarogentin than gentiopicroside and the percentages of adsorption for gentiopicroside reached values under the 50 % with the exception of MgAl-sebacate. The differences in structure between gentiopicroside and amarogentin, in the larger number of phenolic hydroxyl groups of the latter compound, may account for the considerable differences recorded in adsorption.

Interestingly, it can be noted that, for small chain lengths, the percentage of molecule adsorbed, is lower than the ones calculated for longer chains. Increasing the chain length from C_2 to C_4, the percentages increase, while, for higher chain lengths, no big difference in the adsorption capacity is detected. A possible interpretation of this set of data, is that smaller alkyl chains only offer the hydrophilic portion to the target molecules, while, with longer chains, the lipophilic regions of the molecules are also stabilised.

A new survey has been carried out to consider if an increased sorbent loading may affect the adsorption capacity of gentiopicroside.

Thus, two solids resulting from the preliminary screening were selected, and increased quantities of the same (from 100 to 200 mg) were employed under identical experimental conditions for extraction and subsequent quantification by HPLC.

With an increased focus on gentiopicroside, the obtained values showed a very slight increase in the adsorption of the secondary metabolite, maybe because the target molecule is not completely prone to the adsorption.

3.3.2 Comparison between deprotonated monocarboxylic and dicarboxylic acids with same chain length as anions in the interlayer region

The role of the second carboxylic group of the organic modifier is another important aspect of the phenomenon: an experiment was performed adsorbing the target molecules on two MgAl LDHs with pentanoate and nonanoate anions and the results were compared to the ones observed for the azelate and glutarate LDHs. Also in this case the extraction was MW-assisted and in aqueous solution. The results are reported in Table 3.6.

Table 3. 6 Comparison of the adsorption capacities of gentiopicroside and amarogentin of LDHs modified with mono and dicarboxylic acids with equal chain length

Sample entry	Gentiopicroside	Amarogentin
	% ± SD	% ± SD
MgAl-glutarate	43.1 ± 0.1	94.7 ± 0.2
MgAl-pentanoate	40.9 ± 0.1	80.3 ± 0.1
MgAl-azelate	43.3 ± 0.1	97.8 ± 0.1
MgAl-nonanoate	43.6 ± 0.1	72.1 ± 0.4

While almost no variation or only a small one is observed for the gentiopicroside adsorption capacity, the percentage of amarogentin retained by the solids modified with the deprotonated monocarboxylic acids slightly varies, confirming that the interaction of the target molecule with the solids is dependent on the hydrogen bonds that it can make with the sorbent solid. The absence of the second carboxylic group reduces this possibility, considering that the only moiety left is also responsible for the electrostatic interaction with the inorganic matrix in the interlayer region.

3.3.3 Study of the matrix effect

Another variable that can play an important role on the adsorption capacity of the solids under investigation, is the matrix. In previous studies[3], indeed, it was observed that not all the LDHs showed the same behaviour: the zinc aluminium LDHs usually show less interaction with both gentiopicroside and amarogentin. So, to be able to determine if the interaction is mainly driven by the inorganic matrix, or by the nature of the organic anions, adsorption tests were performed on the azelate modified silica and the results were compared with the ones obtained for the MgAl-azelate LDH.

For this experimental set, due to the low viability of the plant during the period of the year in which the tests were performed, the adsorptions were studied on the water solution of the methanolic dried extract obtained previously in the year, as described in chapter 2. The MgAl- azelate reference too was tested in the water solution containing the methanolic extract of *Gentiana lutea.*

The results are shown in Table 3.7.

Table 3. 7 Gentiopicroside and amarogentin adsorption of MgAl-azelate LDH, silica, APTES modified silica and azelate-APTES modified silica

Sample entry	Gentiopicroside	Amarogentin
	% ± SD	% ± SD
MgAl-azelate	42.6 ± 0.1	90.4 ± 0.1
SiO_2	N.D.	20.0 ± 0.2
APTES-SiO_2	64.8 ± 0.2	39.9 ± 0.5
AZ-APTES-SiO_2	39.6 ± 0.2	46.3± 0.1

As it can be observed, the adsorption percentages of the azelate modified silica are lower than the ones seen for the LDH, proving that the inorganic matrix in an important factor in the optimization of the adsorption capacity of the material. This effect is more important when studying the behaviour of amarogentin: this molecule has more hydroxyl groups that can interact with the surface OH of the LDH that remain free after the organic functionalization, and the metallic cation could also play a role in the interaction.

The different percentages of adsorbed gentiopicroside and amarogentin on the variously modified silica can also be discussed. As it is clear from the data, the original silica is not able to adsorb the gentiopicroside and has very low affinity for the amarogentin. Modifying it with APTES on the surface, both the molecules are adsorbed in higher percentage, although the former has a greater increase than the latter. Finally, the last modification with the azelate anion lowers the affinity for gentiopicroside, but increases the one for amarogentin, suggesting that the organic molecule can be responsible for the selectivity shown by the LDHs towards the amarogentin.

3.4 EXTRACTION OF EMODIN AND CHRYSOPHANOL FROM *POLYGONUM CUSPIDATUM*

Given the great affinity of the deprotonated dicarboxylic acids intercalated LDHs towards the hydroxyl group rich amarogentin, the same solids were tested as adsorbents of anthraquinones from *Polygonum cuspidatum* extract. The study was conducted monitoring the concentration of emodin and chrysophanol.

The concentration of emodin and chrysophanol in the dry methanolic extract, obtained as described in materials and methods, determined via HPLC-DAD, are 45.2 ± 0.5 mg/g and 11.2 ± 0.3 mg/g respectively.

In Table 3.8 are reported the obtained results.

Table 3. 8 Quantitative determination of emodin and chrysophanol (values expressed as percentages ± SD) from leaf methanolic extracts of P. cuspidatum adsorbed onto the solid sorbents under investigation

Sample entry	Emodin	Chrysophanol
	% ± SD	% ± SD
MgAl-oxalate	100.0 ± 0.1	99.4 ± 0.1
MgAl-malonate	99.3 ± 0.1	89.8 ± 0.1
MgAl-succinate	97.5 ± 0.1	87.9 ± 0.1
MgAl-glutarate	99.2 ± 0.1	92.6 ± 0.1
MgAl-adipate	100.0 ± 0.2	97.5 ± 0.1
MgAl-pimelate	96.9 ± 0.1	94.7 ± 0.2
MgAl-suberate	99.3 ± 0.1	99.5 ± 0.1
MgAl-azelate	100.0 ± 0.2	84.6 ± 0.1
MgAl-sebacate	97.9 ± 0.1	94.2 ± 0.1
MgAl-dodecandioate	100.0 ± 0.3	98.9 ± 0.1

Contrary to what was observed for gentiopicroside and amarogentin from the *G. lutea* extract, the selectivity towards the emodin with respect to the chrysophanol is very low. Both the target molecules are adsorbed in good percentage by all the solids. It can be observed that in this case no chain length effect is detected, differently from what was seen for the previously examined extract.

3.5 CHARACTERIZATION OF MGAL-AZELATE BEFORE AND AFTER THE ADSORPTION PROCESSES

MgAl-azelate LDH was characterized before and after the adsorption of gentiopicroside and amarogentin from *G. lutea* and of emodin and chrysophanol from *P. cuspidatum*, in order to

understand if the adsorption process mainly happens on the surface of the solid or in the interlayer region, and if the interaction is due to weak forces.

The techniques used to have a physical-chemical characterization of the solids are:

- XRPD analysis

- SEM imaging

- BET surface area analysis

- FT-IR-ATR analysis

3.5.1 XRPD analysis

The diffractometric analysis was conducted on the three solids and gave the following diffraction spectra.

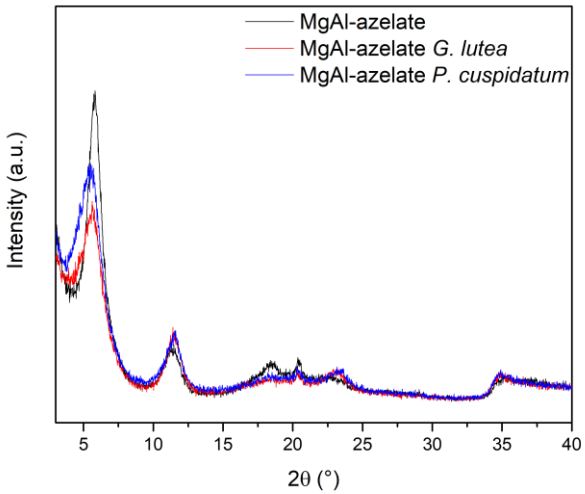

Figure 3. 39 XRPD spectrum of MgAl-azelate LDH as synthetized (black), after being dispersed in a G. lutea extract and dried (red) and after being dispersed in a P. cuspidatum extract and dried (blue)

The main peak doesn't change its position much, indicating an interlayer distance of 15.2 Å, 15.7 Å and 16.0 Å for the starting material, the solid after dispersion in *G. lutea* extract and the solid after dispersion in *P. cuspidatum* extract respectively. Given the high broadness of the peak, this small shift cannot be attributed to the presence in the interlayer region of a bigger anion, but is more likely the result of the experimental variability. The absence of a second phase with a higher interlayer distance means that no target molecule is present in the interlayer region, or at least not in a detectable concentration. Given the small concentration of target molecules on the sorbent

solid, further characterization were performed in order to confirm the data collected via XRPD analysis.

3.5.2 SEM imaging

A morphological analysis was conducted in order to assess if the target molecules are adsorbed on the surface of the solid. To do so the scanning electronic microscope was used in SED mode.

The collected images for the starting material are the following.

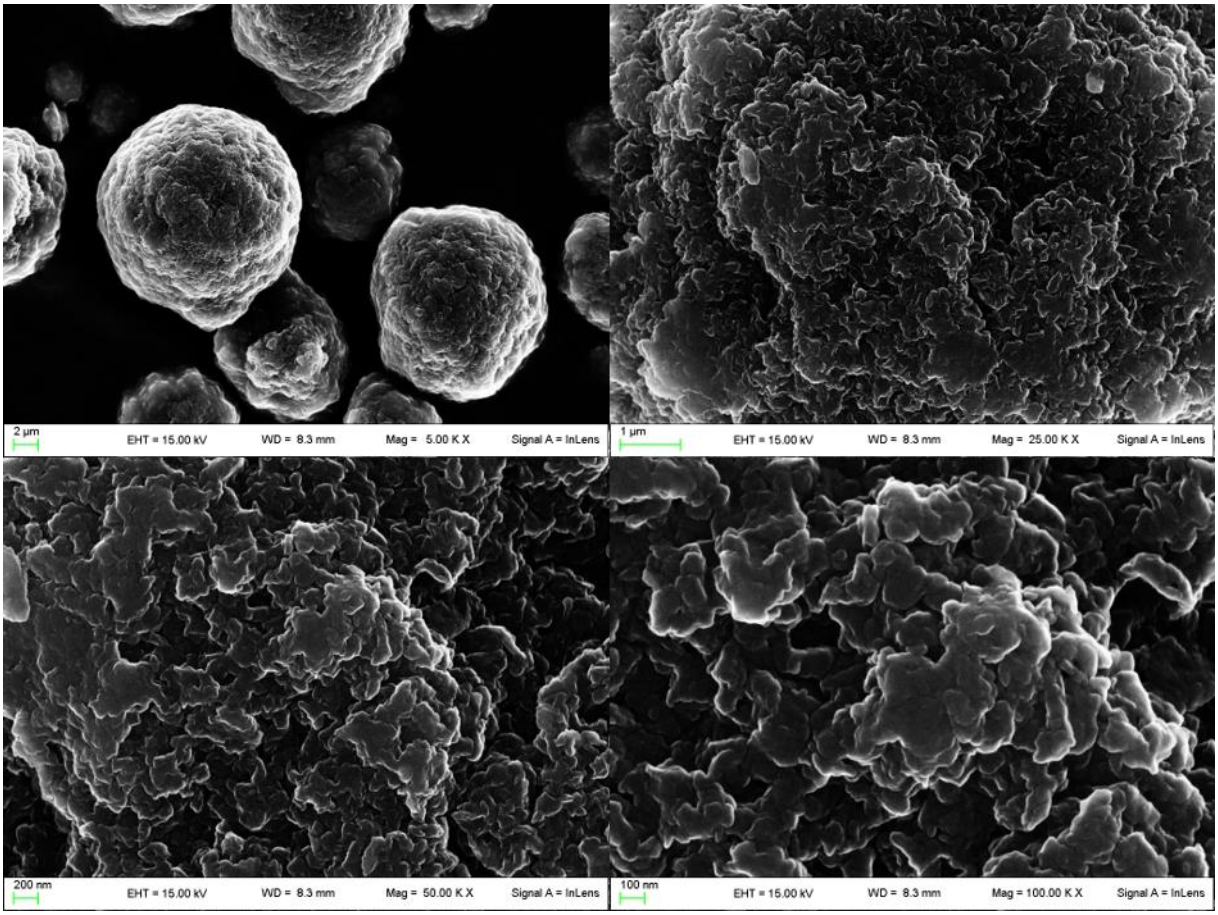

Figure 3. 40 MgAl-azelate SEM images at different magnification (5000x, 25000x, 50000x and 10000x)

Comparing the collected images to the ones collected with same magnifications for the same material after the adsorption of gentiopicroside and amarogentin in *G. lutea* extract (Figure 3.41), a morphological difference in the surface can be seen. While for the as synthetized solid the edges of the pseudo-hexagonal crystals (typical crystalline form of LDHs) are more defined, after the adsorption of the organic molecules the crystals are less identifiable, suggesting that the compounds adsorbed from the extract coat the surface of the solid.

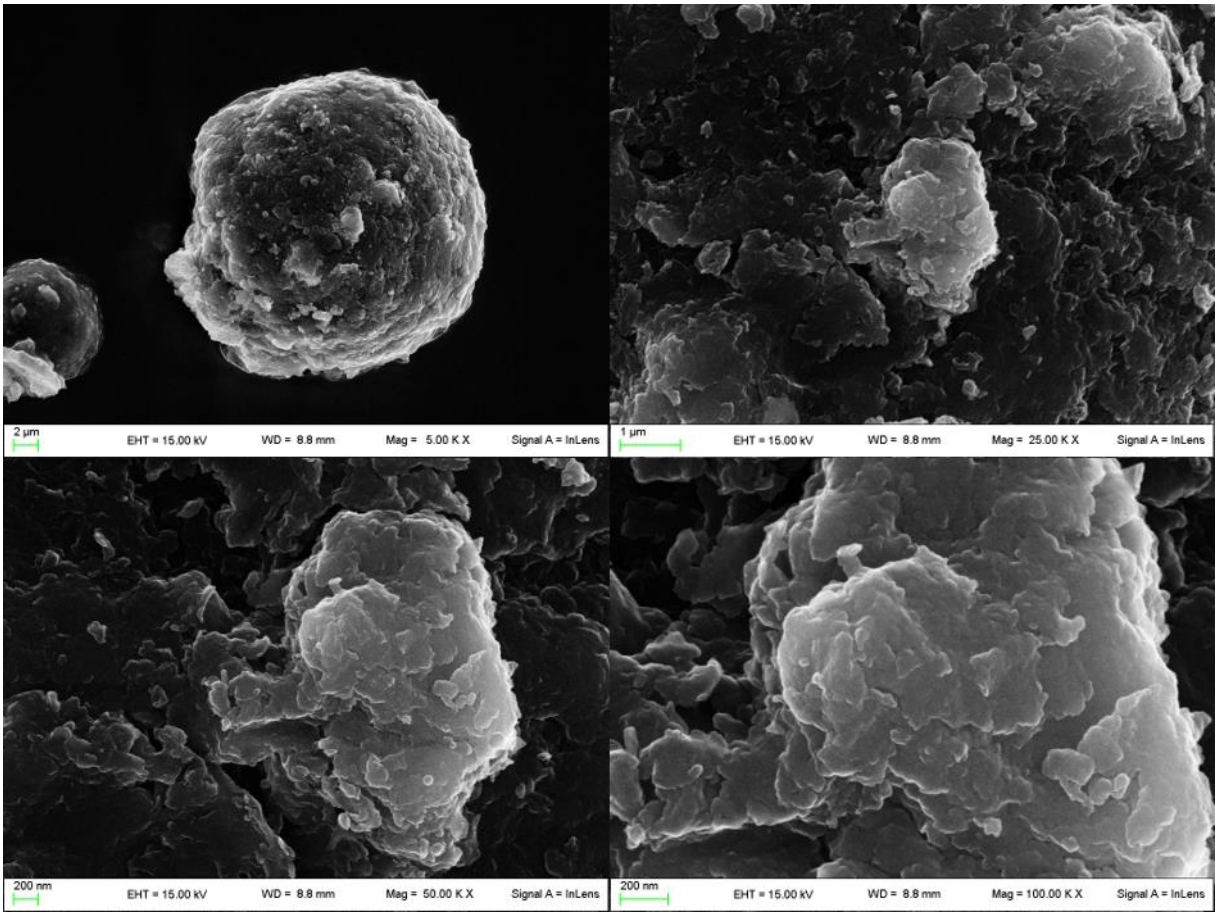

Figure 3. 41 MgAl-azelate after dispersion in G. lutea extract and drying SEM images at different magnification (5000x, 25000x, 50000x and 10000x)

In Figure 3.42 the same behaviour can be seen in the case of MgAl-azelate LDH after being dispersed in *P. cuspidatum* extract and subsequently separated and dried.

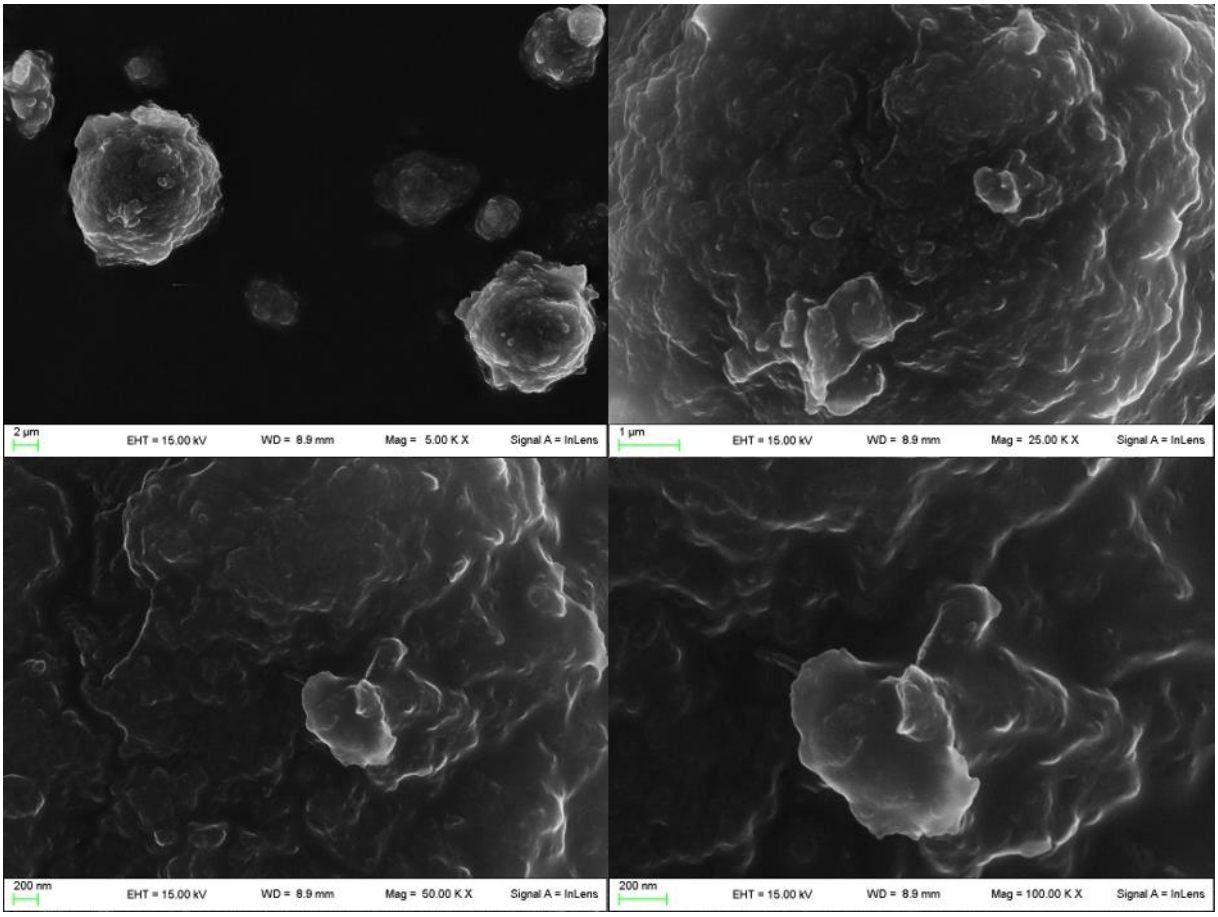

Figure 3. 42 MgAl-azelate after dispersion in P. cuspidatum extract and drying SEM images at different magnification (5000x, 25000x, 50000x and 10000x)

3.5.3 BET surface area analysis

The hypothesis of a surface interaction between the MgAl-azelate LDH and the target molecules was confirmed by the BET surface area analysis. Even though the changes in surface area are not big, this morphological modification is consistent with the results of the previous characterizations.

Table 3.9 summarizes the results of this analysis.

Table 3. 9 BET surface areas of the three studied solids

Solid	**MgAl-azelate**	**MgAl-azelate- *G. lutea***	**MgAl-azelate- *P. cuspidatum***
BET surface area (m^2/g)	1.31	3.81	3.45

3.5.4 FT-IR-ATR analysis

The nature of the bonds between the molecules solubilized in the phytoextracts and the solid on which they are adsorbed, was studied via FT-IR-ATR analysis.

The analysis was conducted first on the solid on which the organic molecules were adsorbed. The solids were then dispersed in ethanol as described in chapter 2 and the supernatant was analysed after the solvent evaporation.

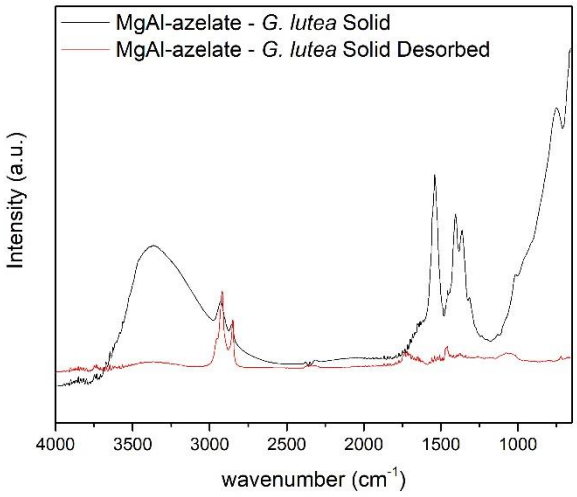

Figure 3. 43 FTIR-ATR spectra of MgAl-azelate LDH after adsorption of G. lutea extract and of its the desorbed compounds

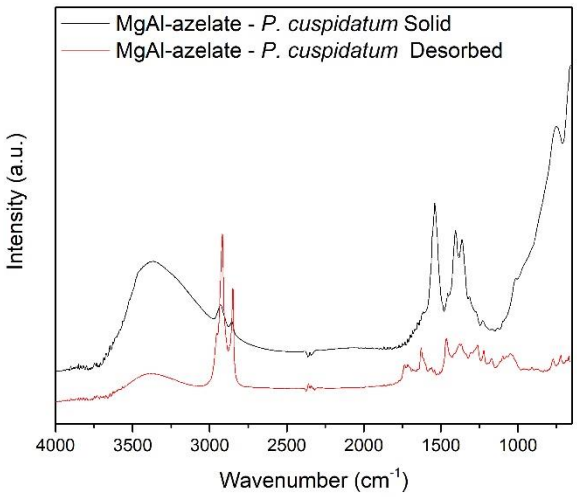

Figure 3. 44 FTIR-ATR spectra of MgAl-azelate LDH after adsorption of P. cuspidatum extract and of its the desorbed compounds

In the spectrum of the desorbed compounds, the typical peaks of the CH bond are detected at 2855 cm^{-1} and 2919 cm^{-1} in the case of the *G. lutea* derived solid and at 2849 cm^{-1} and 2917 cm^{-1} in the

case of the *P. cuspidatum* derived solid, suggesting that the adsorbed organic molecules have been desorbed. No C=O peak of the azelaic acid at 1683 cm^{-1} is observed, hence there has been no desorption of the azelate anion that is bond by ionic forces.

The observed behaviour suggests that the target organic molecules in the phytoextracts interact with the inorganic-organic solid via weak forces with the surface of the solid. The results are coherent with what was already observed in previous studies[4] where multiple cycles of adsorption and desorption of gentiopicroside and amarogentin were performed.

3.6 STUDY OF THE EFFECT OF THE SURFACE AREA

The adsorption of gentiopicroside and amarogentin from *G. lutea* and of emodin and chrysophanol from *P. cuspidatum*, was evaluated using as sorbent solids two LDHs both made of Mg and Al hydroxides and carbonate as counterion, but with different surface areas. The goal of the experiment was to verify the influence of the surface area on the adsorption capacity of the solids. The selected materials were MgAl-CO_3 LDH characterised by low surface area of 17.10 m^2/g (MgAl-CO_3 LA) and MgAl-CO_3 LDH characterised by high surface area of 72.58 m^2/g (MgAl-CO_3 HA); the commercial silica AEROSIL MOX 80 (SiO_2 MOX 80) with a surface area comparable to the one measured for MgAl-CO_3 HA (60-100 m^2/g declared by the manufacturer) was also tested as reference. It has to be noted that, even though the major difference between the two LDHs lays in the different surface area, another difference is given by the metals molar fractions. Unfortunately, it was not possible to synthetize two materials that only differ for the surface area.

The extract was obtained via methanolic maceration, dried and then dispersed again in water as described in chapter 2. The results are listed below.

Table 3. 10 Quantitative determination of gentiopicroside and amarogentin (values expressed as percentages ± SD) from leaf methanolic extracts of G. lutea adsorbed onto the solid sorbents under investigation

Sample entry	Gentiopicroside	Amarogentin
	% ± SD	% ± SD
MgAl-CO_3 LA [100mg]	12.3 ± 0.1	100.0 ± 0.1
MgAl-CO_3 HA [100mg]	79 ± 0.1	90.6 ± 0.1
MgAl-CO_3 HA [50mg]	55.7 ± 0.1	88.0 ± 0.1
SiO_2 MOX 80 [100mg]	3.5 ± 0.2	11.4 ± 0.2

Concerning the *G. lutea* extract, an increase in the adsorption percentages of gentiopicroside is observed for the high surface area LDH, while a slight decrease in the adsorption percentage of amarogentin is registered, even though it can be considered quite a high value anyway. The same behaviour can be observed with lower quantities of MgAl-CO_3 HA, confirming a much higher affinity of gentiopicroside for the high surface area LDH. The importance of the solid chemical nature emerges when comparing the results registered for the high surface area LDH with the much lower ones observed for the high surface area silica SiO_2 MOX 80.

The same experiment was conducted on *P. cuspidatum* extract.

Table 3. 11 Quantitative determination of emodin and chrysophanol (values expressed as percentages ± SD) from leaf methanolic extracts of P. cuspidatum adsorbed onto the solid sorbents under investigation

Sample entry	Emodin	Crysophanol
	% ± SD	% ± SD
MgAl-CO_3 LA [100mg]	81.1 ± 0.2	83.1 ± 0.2
MgAl-CO_3 HA [100mg]	100.0 ± 0.2	100.0 ± 0.2
MgAl-CO_3 HA [50mg]	99.5 ± 0.2	100.0 ± 0.2
SiO_2 MOX 80 [100mg]	55.3 ± 0.2	55.4 ± 0.1

In this case a higher affinity for both the target molecules can be observed for the MgAlCO_3 HA LDH compared to the performances of MgAl-CO_3 LA. The high affinity is confirmed by the adsorption percentages calculated for lower quantities of MgAl-CO_3 HA. Also in this case the performances

registered for the commercial silica are worse than the ones observed for the LDHs, confirming the key role of the chemical nature of the solid in the adsorption process.

MgAl-CO_3 HA was analysed before and after the adsorption processes via XRPD analysis, SEM imaging and FT-IR-ATR analysis.

3.6.1 XRPD analysis

The XRPD pattern show the same behaviour observed for the MgAl-azelate: no modification of the spectra is observed after the adsorption process. The collected spectra are reported in Figure 3.45

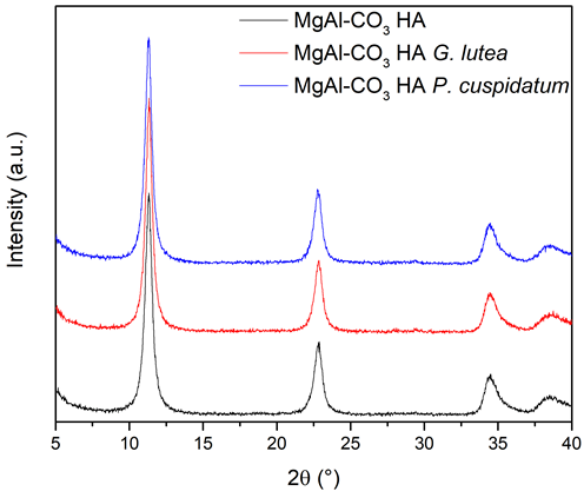

Figure 3. 45 XRPD pattern of MgAl-CO_3 HA as synthetised (black), after the extraction of gentiopicroside and amarogentin from G. lutea (red) and after the adsorption of emodin and chrysophanol from P. cuspidatum extract (blue)

3.6.2 SEM images

The images collected with the electronic microscope, show a morphology similar to the one observed for the MgAl-azelate LDH. The crystals surface seems to be slightly less defined after contact with the phytoextract, even though the effect is less evident with respect to what was seen for the previous solid. The SEM images collected are the following:

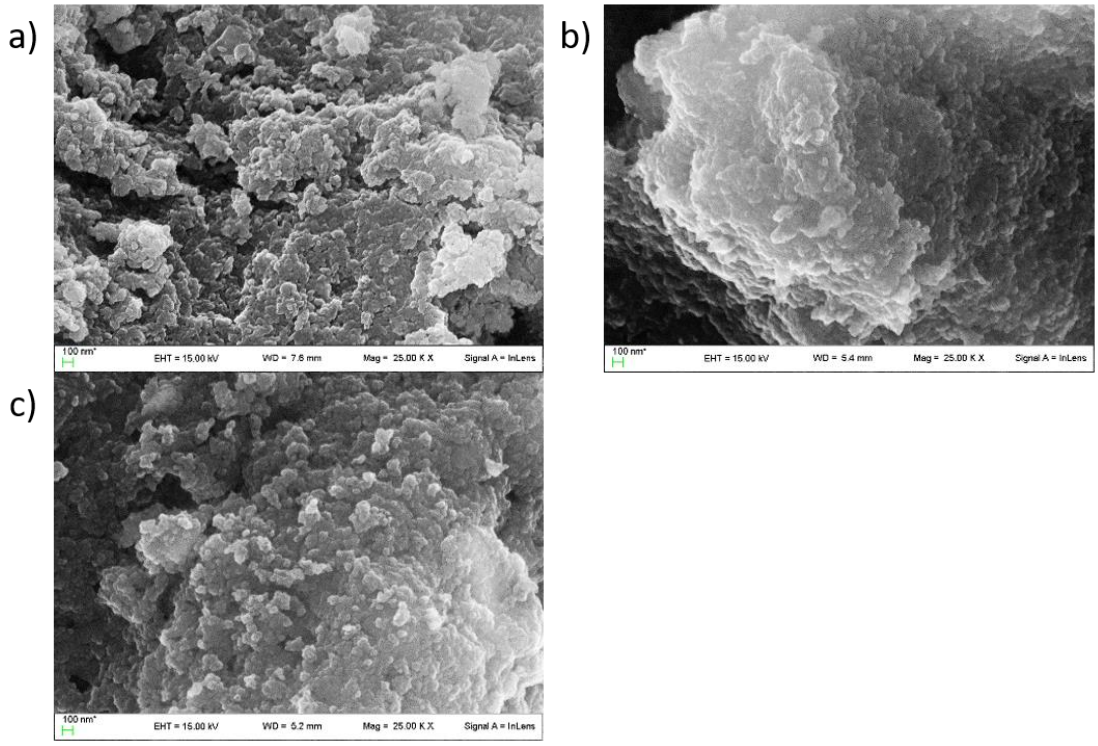

Figure 3. 46 SEM images at 25000x of a) MgAl-CO_3 HA, b) MgAl-CO_3 HA after the dispersion in G. lutea and following drying and c) MgAl-CO_3 HA after the dispersion in P. cuspidatum and following drying

3.6.3 BET analysis

The BET analysis is coherent with the results of the previous analysis conducted on MgAl-azelate LDH.

Table 3. 12 BET surface area of MgAl-CO_3 HA before and after the adsorption of the studied organic molecules

Solid	**MgAl-CO_3 HA**	**MgAl-CO_3 HA-** ***G. lutea***	**MgAl-CO_3 HA -** ***P. cuspidatum***
BET surface area(m^2/g)	72.58	88.77	99.97

3.6.4 FT-IR-ATR analysis

Also for FT-IR analysis the results are coherent with the ones already observed for MgAl-azelate as sorbent solid.

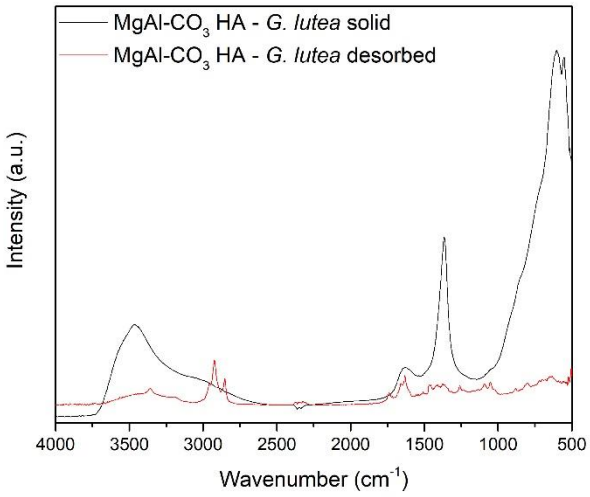

Figure 3. 47 FTIR-ATR spectra of MgAl-CO_3 HA LDH after adsorption of G. lutea extract and of its the desorbed compounds

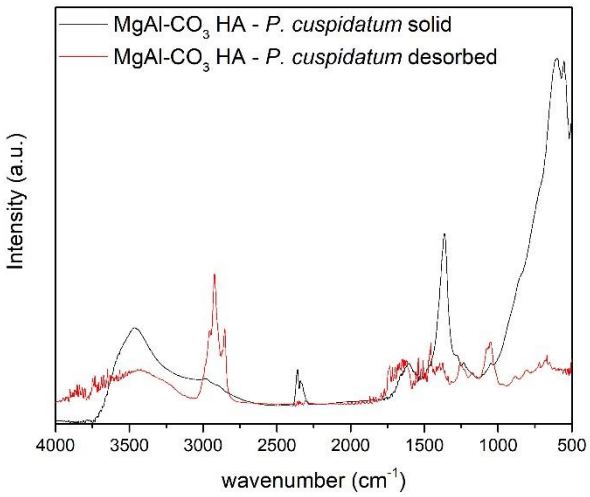

Figure 3. 48 FTIR-ATR spectra of MgAl-CO_3 HA LDH after adsorption of P. cuspidatum extract and of its the desorbed compounds

The presence of C-H bond typical signals in the desorbed spectrum confirms the presence of organic molecules bonded to the LDH with weak forces, probably von der Waals and hydrogen bonds.

BIBLIOGRAPHY

[1] T. Kuehn, H. Poellmann, “Synthesis and Characterization of Zn-Al Layered Double Hydroxides Intercalated With 1- to 19-Carbon Carboxylic Acid Anions” *Clays Clay Miner.* **2010**, *58*, 596–605.

[2] N. Majoul, S. Aouida, B. Bessaïs, “Progress of porous silicon APTES-functionalization by FTIR investigations” *Appl. Surf. Sci.* **2015**, *331*, 388–391.

[3] S. Fiorito, F. Epifano, L. Marchetti, L. Palumbo, F. Mascioli, M. Bastianini, F. Cardellini, R. Spogli, S. Genovese, “An improved method for the isolation of amarogentin, the bitter principle of yellow gentian roots” *Food Chem.* **2021**, *364*, 130383.

[4] S. Fiorito, F. Epifano, L. Palumbo, C. Collevecchio, F. Mascioli, R. Spogli, S. Genovese, “Leaves of Yellow Gentian (*Gentiana lutea*) as an Alternative Source of Bitter Secoiridoid Glycosides” *J. Nat. Prod.* **2022**, *85*, 2232–2235.

4 RESULTS AND DISCUSSION

ANTIBIOTIC REMOVAL FROM WATER

4.1 CHARACTERIZATION OF SYNTHETIZED SORBENT SOLIDS

To develop a removal system for SMX, CPX and TC, some new solids were synthesized and characterized. Here are reported the characterizations for MgAl-Cl, ZnAl-Cl, ZnAl-NO_3 and ZnAl-acetate LDHs. The other not commercial tested sorbent solids were already characterized in the previous chapter.

The XRPD pattern of MgAl-Cl can be observed in Figure 4.1.

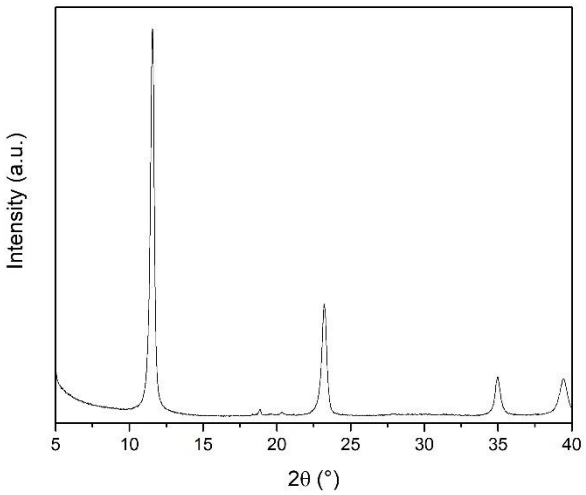

Figure 4. 1 XRPD pattern collected for MgAl-Cl LDH

The position of the main peak corresponds to an interlayer distance of 7.7 Å, typical of the MgAl-Cl LDHs.

The composition of the LDH was calculated on the basis of the ICP-OES analysis and was the following: $Mg_{0.62}Al_{0.38}Cl_{0.38}(OH)_2$*n H_2O. The precise value of n is difficult to determine even with TG analysis, because, apart from the crystallization water molecules, the material tends to adsorb water depending on the air humidity and the evaporation processes are not separated in TGA, therefore it's difficult to determine the precise formula weight of LDHs. In order to estimate the formula weight, n was considered equal to 1, leading to a FW of 90.79 g/mol.

The ZnAl-Cl LDH is characterized by an interlayer distance of 7.5 Å, coherent with the dimensions of the anion in the interlayer region (Figure 4.2).

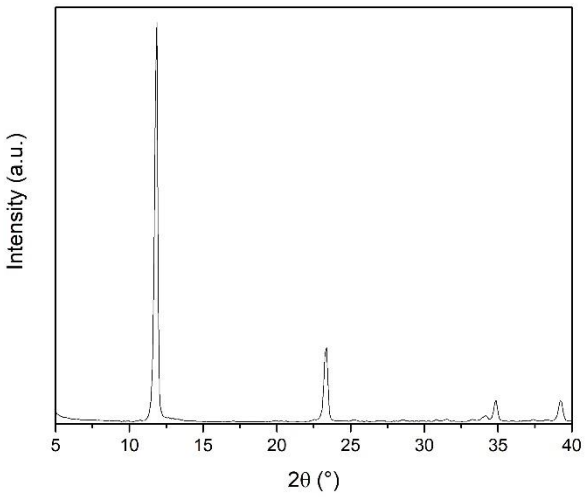

Figure 4. 2 XRPD pattern collected for ZnAl-Cl LDH

The composition of the LDH was determined via ICP-OES and the results are the following: $Zn_{0.72}Al_{0.28}Cl_{0.28}(OH)_2$* n H_2O. The precise value of n is difficult to determine even with TG analysis, because, apart from the crystallization water molecules, the material tends to adsorb water depending on the air humidity, and the evaporation processes are not separated in TGA, therefore it's difficult to determine the precise formula weight of LDHs. In order to estimate the formula weight, n was considered equal to 1, leading to a FW of 116.55 g/mol.

The XRPD spectrum collected for ZnAl-NO_3 is reported below. It is characterized by the position of the main peak that corresponds to an interlayer distance of 8.8 Å as it usually is for this type of materials. The peak at 6.5 ° (corresponding to a distance of 13.5 Å), is due to the presence of a small quantity of a precursor phase.

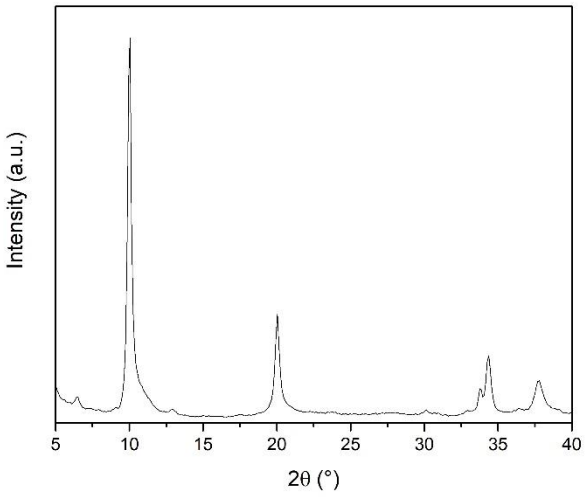

Figure 4. 3 XRPD pattern collected for ZnAl-NO_3 LDH

The composition of the LDH was determined via ICP-OES and the results are the following: $Zn_{0.75}Al_{0.25}(NO_3)_{0.25}(OH)_2*nH_2O$. Also in this case, the precise value of n is difficult to determine even with TG analysis, because, apart from the crystallization water molecules, the material tends to adsorb water depending on the air humidity, and the evaporation processes are not separated in TGA, therefore it's difficult to determine the precise formula weight of LDHs. In order to estimate the formula weight, n was considered equal to 1, leading to a FW of 123.30 g/mol. The ion exchange capacity, calculated with the same approximation, is 2.0 mmol/g.

The behaviour of the material increasing the temperature was evaluated via TGA-DSC analysis in order to have more useful data for the following functionalization. The recorded pattern is showed below.

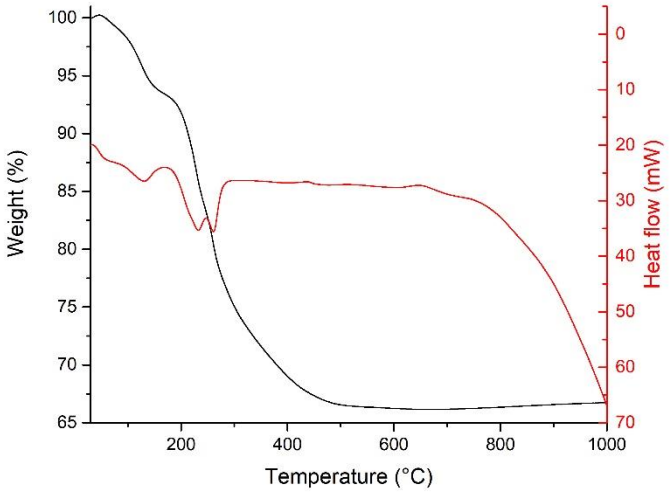

Figure 4. 4 TGA (black) and DSC (red) patterns of ZnAl-NO_3 LDH

The water percentage calculated from the analysis is of 6.7% (first weight loss); the second TGA step of 27.2% is due to the nitrates decomposition and the OH condensation.

The XRPD spectrum of ZnAl-acetate (Figure 4.5) is characterized by a main peak that corresponds to an interlayer region of 12.8 Å as expected, but the presence of the main peak of another phase can be observed at 11.6 ° (corresponding to a distance of 7.6 Å), that highlights the presence of a minor percentage of LDH with the carbonate anion in the interlayer region.

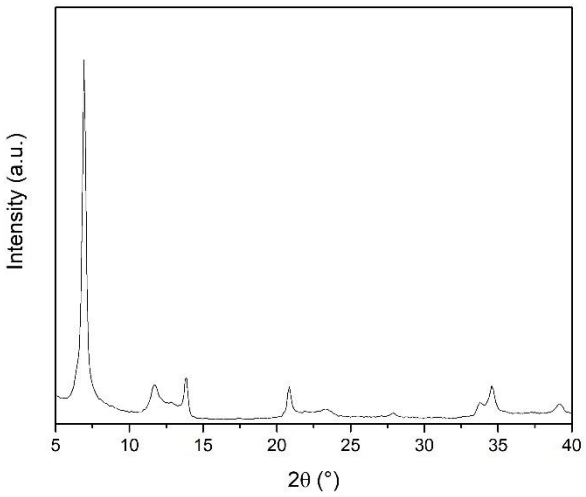

Figure 4. 5 XRPD pattern collected for ZnAl-acetate LDH

The composition of the LDH, determined via ICP-OES is: $Zn_{0.75}Al_{0.25}(Acetate)_{0.25}(OH)_2$* n H_2O.

The ZnAl-acetate LDH has the same composition of the nitrate one because it was obtained by organically modifying the nitrate form. The formula weight is not calculated because some of the nitrate anions haven't been exchanged, as demonstrated by IR spectrum. It shows the presence of a residue of the peak present in the nitrate pristine form at 1384 cm^{-1}, in addition to peaks associated to the presence of C-H bonds (2851 cm^{-1} and 2922 cm^{-1}).

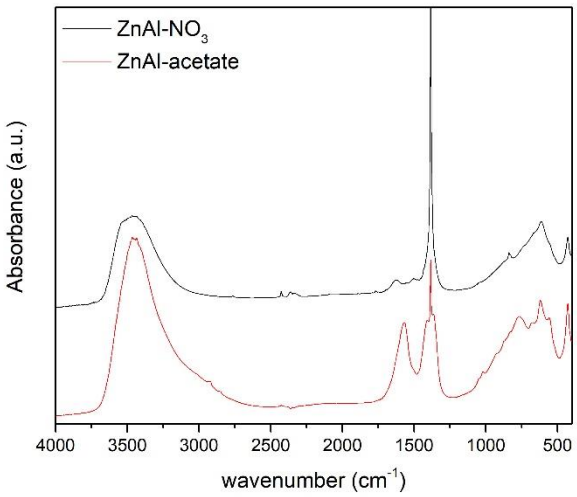

Figure 4. 6 IR spectra of ZnAl-NO_3 (black line) and ZnAl-acetate (red line)

The acetate LDH was also characterized via TGA and DSC analysis, and the graphs are reported below. The percentage of water is of 7.0%, while the total weight loss is of 37.8%, with a weight loss without water of 30.8%. The presence of other phases (i.e. carbonate containing phase) makes it difficult to determine the precise percentage of organic modifier. The DSC analysis shows the presence of different processes both endothermic and exothermic.

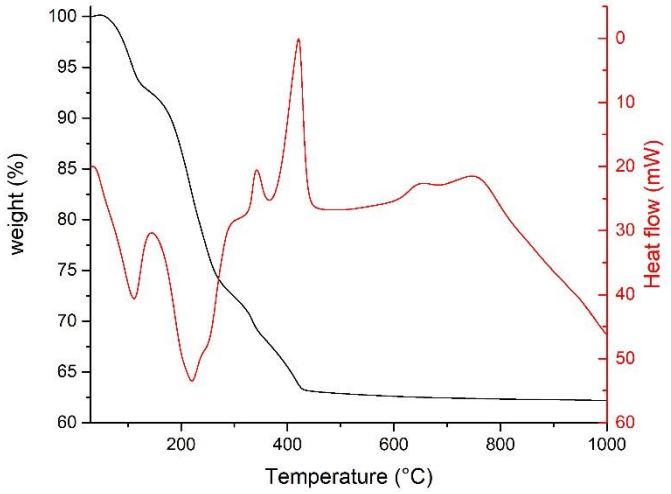

Figure 4. 7 TGA (black line) and DSC (red line) patterns of ZnAl-acetate LDH

The characterizations of the other synthetized sorbent solids used in the experiments presented in this chapter have already been reported in the previous chapter.

4.2 ADSORPTION TESTS OF SMX ON LDHS BASED ON ION EXCHANGE

4.2.1 LDHs screening

The adsorption capacity towards SMX of five LDHs usually used for ion exchange of the anion in the interlayer region have been tested via UV-vis analysis over 24 hours, by the methodology explained in Chapter 2.

The tested LDHs are: MgAl-NO_3, MgAl-Cl, ZnAl-NO_3, ZnAl-Cl and ZnAl-acetate. The measured adsorption capacities are listed in the following table.

Table 4. 1 Removal percentages of SMX by LDHs

Sample entry	SMX
	% ± SD
MgAl-NO_3	38 ± 7
MgAl-Cl	19 ± 5
ZnAl-NO_3	71 ± 2
ZnAl-Cl	24 ± 8
ZnAl-acetate	89 ± 2

Table 4.1 shows that the ZnAl-acetate has the highest adsorption capacity towards SMX.

The structure of each solid was then analysed via XRPD analysis to evaluate the impact of the adsorption of SMX on the crystalline structure of the solids. From Figure 4.8 it is clear that all the MgAl LDHs and the ZnAl-Cl LDH show no variation in the interlayer region, while the spectra of both ZnAl-NO_3 and ZnAl-acetate LDHs are characterized by the presence of a small peak corresponding to an interlayer distance of 15.4 Å (2θ=5.7 °) for the acetate LDH and 15.9 Å (2θ=5.5 °) for the nitrate LDH that are probably caused by the intercalation of SMX and one at 7.6 Å (2θ=11.6 °) in both cases due to the presence of carbonate anions in the interlayer region. The peak that corresponds to an interlayer distance of 13.5 Å (2θ=6.5 °) that was already visible in the ZnAl-NO_3 LDH before the SMX adsorption, is visible also in the case of the ZnAl-acetate LDH after the adsorption: as the intensity of the acetate peak decreases, it becomes visible also for this solid, as expected considering that it was synthetized starting from ZnAl-NO_3 LDH.

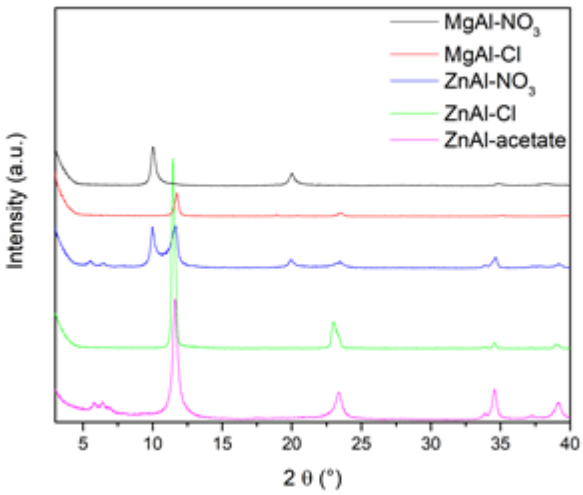

Figure 4. 8 XRPD spectra of the tested LDHs after the SMX adsorption

The ZnAl-acetate LDH, being the solid with the highest adsorption capacity compared to the other tested ones, was selected to further investigate the effect of pH, the kinetic of the adsorption process and the effect of the SMX/solid ratio.

4.2.2 Effect of the pH

The adsorption capacity of the selected solid was tested at three different pH values: 7.0 ± 0.5, 9.0 ± 0.5 and 3.0 ± 0.5, reached by adding NaOH or HCl to the SMX water solution as described in the relative paragraph in Chapter 2.

The results collected are reported in Table 4.2.

Table 4. 2 Effect of the solution pH on the SMX adsorption capacity of ZnAl-acetate LDH

pH	**SMX**
	% ± SD
9.0	90 ± 1
7.0	89.9 ± 0.1
3.0	82 ± 3

The alkaline environment favours the deprotonation of SMX, hence increasing the percentage of anion that can interact with the positively charged matrix. At neutral pH, the percentage of adsorbed SMX doesn't change compared to the one calculated for the alkaline environment: the molecule is already mostly deprotonated, having a pK_a of the acid proton of 5.7 [1]. At lower pH values, a small decrease in the adsorption capacity is detected: this could be correlated to a lower percentage of anion in solution.

4.2.3 Kinetic of the adsorption process

The adsorbed SMX was quantified over time from the starting of the contact between the LDH and the SMX solution up to 24 hours.

Figure 4.9 shows the observed trend: after 15 minutes (first point) 87 ± 4 % of the SMX is adsorbed, and this percentage increases up to a maximum of 89 ± 2 %, reached after 1 hour. It can be noted that after 24 hours the mean value of the adsorption percentage slightly decreases (88 ± 2 %), probably due to the reach of an equilibrium status.

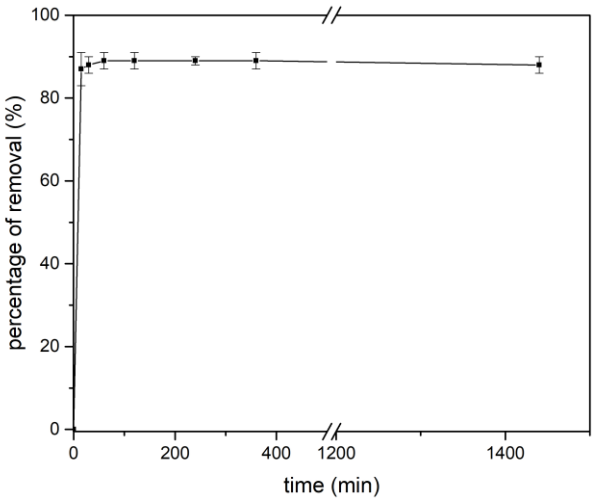

Figure 4. 9 Kinetic trend of the SMX adsorption on ZnAl-acetate LDH

The XRPD spectra of the LDH after different contact times with the SMX solution were collected. Figure 4.10 shows the lowering of the peak associated to the presence of the acetate in the interlayer region (6.9 ° corresponding to an interlayer distance of 12.8 Å) and an increase of the intensity of the peak at 5.7 ° (corresponding to an interlayer distance of 15.4 Å) associated to the presence of SMX in the interlayer region, over time. All the spectra are characterized by the presence of the peak of the carbonate (11.6°, 7.6 Å).

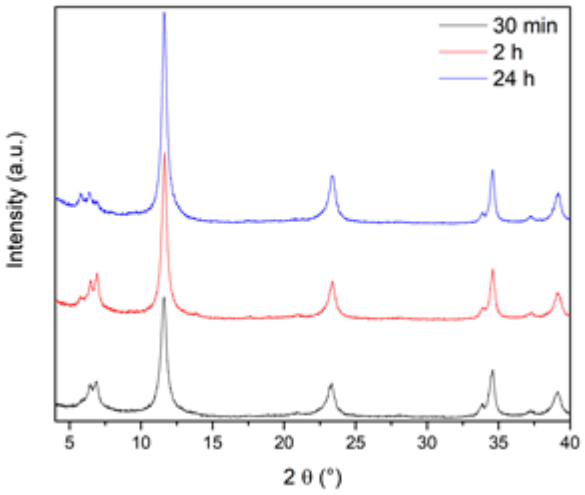

Figure 4. 10 XRPD spectra of ZnAl-acetate LDH after 30 minutes, 2 hours and 24 hours of contact with SMX solution

The differences in the peaks intensity after 2 and 24 hours, both collected after reaching the maximum percentage of adsorption, may suggest that, after a first interaction of the SMX with the surface of the LDH, the anionic antibiotic settles in the interlayer region, while the acetate is released. The spectra show the tendency of the LDH to incorporate carbonate anions in the interlayer region, which are hardly exchangeable.

4.2.4 Effect of the SMX / LDH ratio

To verify if the adsorption can be performed in a more efficient way, the SMX / LDH ratio have been varied: in particular, 200 mg and 100 mg of LDH were dispersed in 100 mL of the SMX solution 200 mg/L, to compare the performances of ratios of 1:10 and 1:05 to the one previously used of 1:20.

The percentages of adsorption measured were of 78 ± 3 % and 43 ± 2 % for the 1:10 and the 1:05 ratios respectively, confirming that lower quantities of LDH would reduce the adsorption of the antibiotic.

4.2.5 SEM characterization of the LDH after the adsorption

After the SMX adsorption with 24 hours of contact (SMX / LDH = 1:20), the recovered solid was analysed at the SEM. The images in Figure 4.11 show the typical desert rose morphology usually observed for this material.

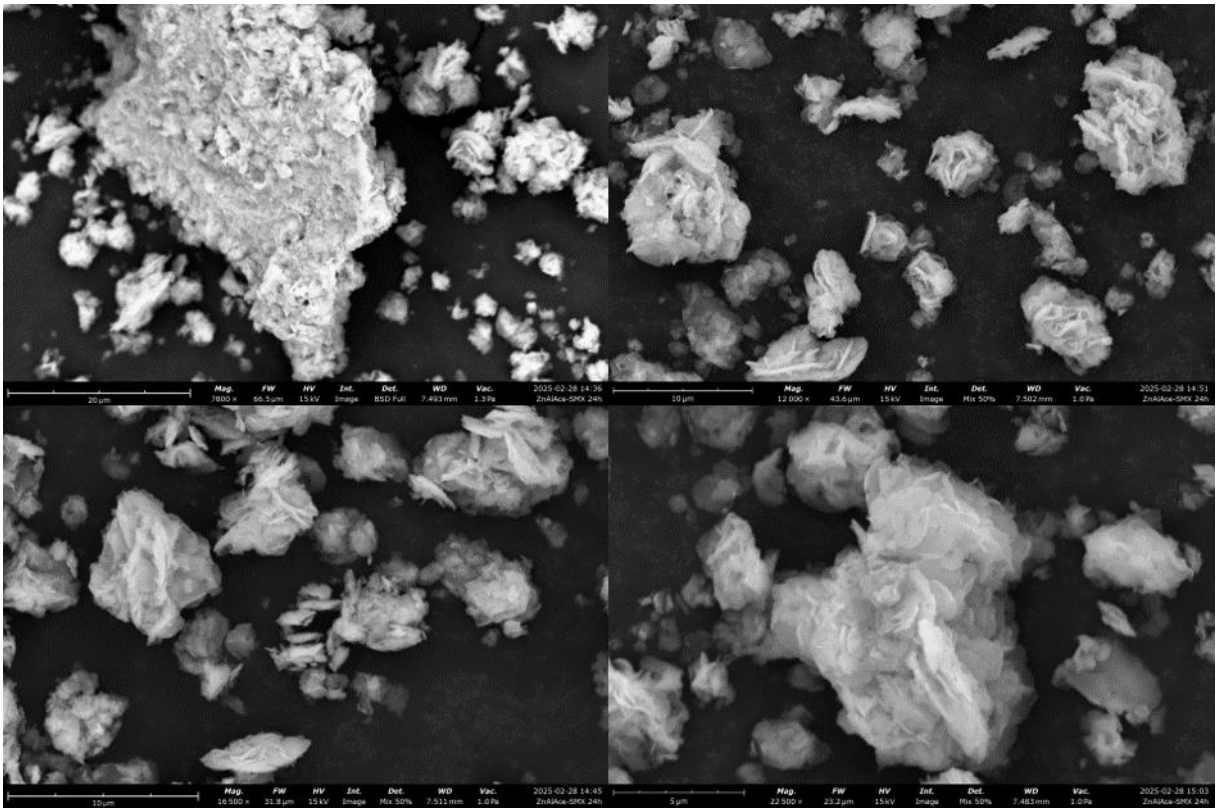

Figure 4. 11 SEM images of ZnAl-acetate after SMX adsorption (magnification 7800x, 12000x, 16500x and 22500x)

To verify the presence of SMX on the crystals, the EDX analysis was performed: in Figure 4.12 the uniform distribution of sulfur and nitrogen on the crystals, both present in the SMX structure, can be seen, confirming that the antibiotic is homogenously adsorbed by the LDH crystals.

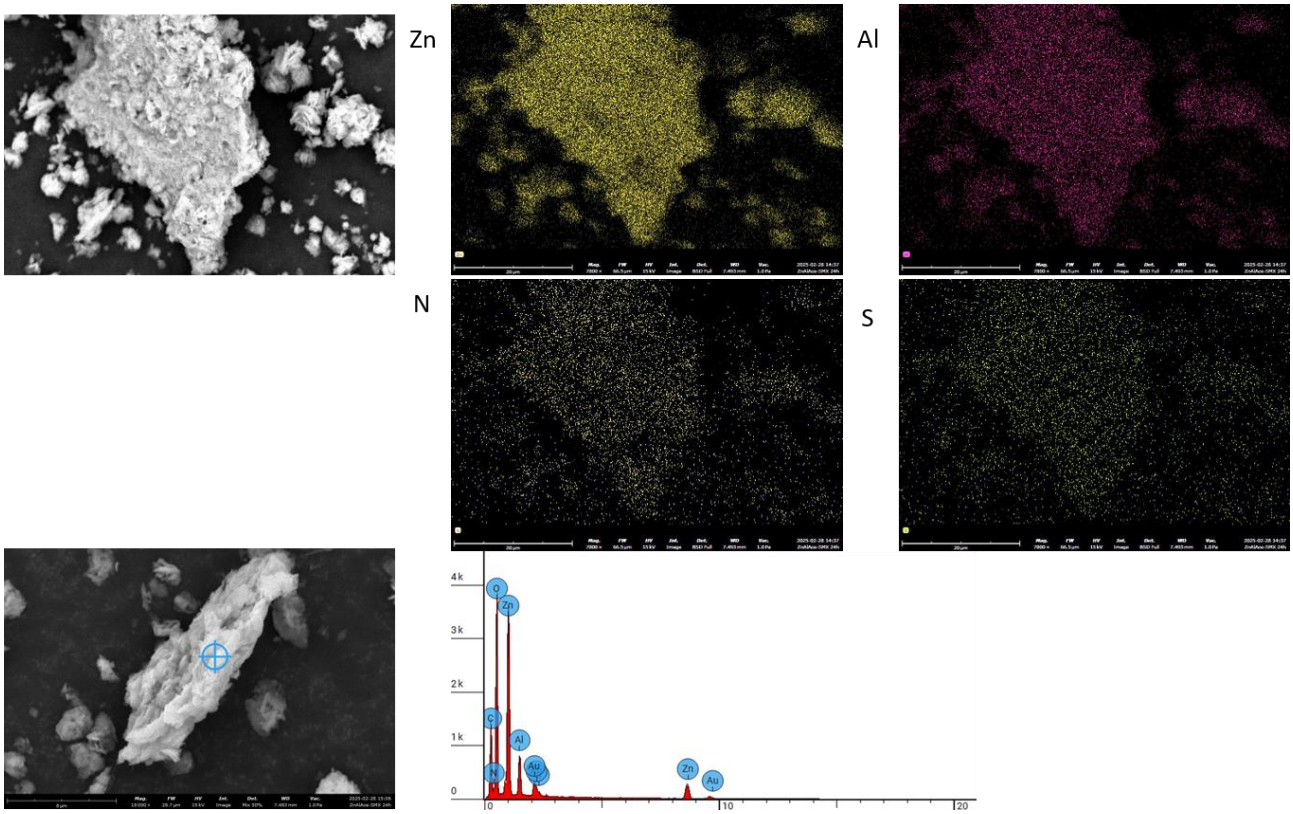

Figure 4. 12 EDX mapping of a crystal of ZnAl-acetate after adsorption of SMX and punctual EDX analysis

The percentages of every element measured with the punctual EDX analysis are listed in Table 4.3. Even though in low concentration, as expected, both sulfur and nitrogen are detected also in this analysis.

Table 4. 3 Results of the EDX punctual analysis

Element Symbol	Element Name	Atomic Conc. [%]	Weight Conc. [%]
C	Carbon	32.26	18.00
N	Nitrogen	2.30	1.50
O	Oxygen	49.51	36.80
Al	Aluminium	4.31	5.40
S	Sulfur	0.54	0.80
Zn	Zinc	10.44	31.70
Au	Gold	0.63	5.80

4.3 ADSORPTION TESTS ON SORBENT SOLIDS BASED ON NON-IONIC INTERACTIONS

4.3.1 Adsorption of SMX

The presence of high percentages of carbonate anion in the interlayer region after the adsorption of SMX, makes the reuse of the ZnAl-acetate LDH difficult. Therefore, other sorbent solids were tested, this time the selection was made among solids that don't usually give anion exchanges. The adsorption capacity was tested via HPLC-DAD analysis. The first experimental set was obtained testing the adsorption capacity of different solids with a SMX / sorbent solid ratio of 1:100 in weight.

The solids were selected based on their potential ability to give weak interactions with the analyte.

The results are listed in the following table, expressed as mean values ± SD.

Table 4. 4 Quantification of SMX absorbed on 100 mg of solid in percentage (%), after treatment and HPLC-DAD analysis

Sample entry	SMX
	%
Magnesium oxide	N.D.
MgAl-pentanoate	75.9 ± 0.1
MgAl-oxalate	11.7 ± 0.2
MgAl-malonate	12.4 ± 0.2
MgAl-succinate	14.7 ± 0.2
MgAl-glutarate	17.2 ± 0.2
MgAl-adipate	15.8 ± 0.2
MgAl-pimelate	22.1 ± 0.3
MgAl-suberate	91.2 ± 0.1
MgAl-azelate	13.0 ± 0.2
MgAl-sebacate	75.5 ± 0.1
MgAl-dodecandioate	27.0 ± 0.4

Good results were obtained for MgAl-pentanoate, MgAl-suberate and MgAl-sebacate.

Given the promising results, the same analysis was performed to assess the adsorption capacity of the same set of solids towards CPX, another widely spread antibiotic selected for this study.

4.3.2 Adsorption of CPX

The experiments were performed using the same conditions of the previous set. The results are listed in the following table, expressed as mean value ± SD.

Table 4. 5 Quantification of CPX absorbed on 100 mg of solid in percentage (%), after treatment and HPLC-DAD analysis

Sample entry	CPX
	%
Magnesium oxide	97.4 ± 0.3
MgAl-pentanoate	N.D.
MgAl-oxalate	20.7 ± 0.26
MgAl-malonate	8.5 ± 0.10
MgAl-succinate	N.D.
MgAl-glutarate	N.D.
MgAl-adipate	21.9 ± 0.3
MgAl-pimelate	N.D.
MgAl-suberate	38.8 ± 0.1
MgAl-azelate	88.9 ± 0.1
MgAl-sebacate	96.9 ± 0.1
MgAl-dodecandioate	100.0 ± 0.2

In this case the most promising materials are magnesium oxide, MgAl-sebacate and MgAl-dodecandioate.

Only one of the tested solids has shown good adsorption capacity towards both antibiotics: MgAl-sebacate LDH.

The most performing solids for each antibiotic were characterized before and after the adsorption to assess if there were any structural or morphological changes in the sorbents.

4.3.3 Solids characterization after adsorption

The structural variations were studied via XRPD analysis. The spectra collected for MgAl-pentanoate are reported in Figure 4.13.

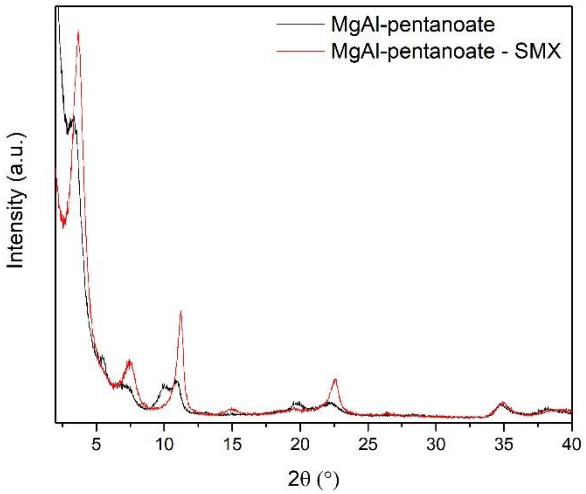

Figure 4. 13 XRPD spectra of MgAl-pentanoate before and after SMX adsorption

The position of the main peak doesn't change significantly, while the small peak of the hydrated form of interlayer pentanoate anion, visible in the solid before the adsorption, is not detected after the dispersion in SMX solution and drying process. On the other hand, after the adsorption, the peak associated to the presence of the carbonate anion in the interlayer region is more intense, suggesting the presence of a higher percentage of intercalated carbonate anion. No peak that could be assigned to SMX in the interlayer region is detected: this observation could either confirm its absence between the lamellae or be a consequence of the low concentration of the antibiotic in the interlayer region.

The spectra collected for MgAl-suberate are reported in Figure 4.14 a. The position of the three most intense peaks is slightly shifted after the adsorption of the antibiotic, probably due to a different hydration degree of the organic molecules in the interlayer region. In order to confirm this hypothesis, the sorbent solid was dispersed in pure water, collected and dried in the same conditions used for the solid after the antibiotic sorption. The comparison, showed in Figure 4.14 b, shows that the position of the peaks for the solid analysed immediately after the dispersion in water and drying is the same of the one that has adsorbed SMX. No peak indicates the presence of SMX in the interlayer region.

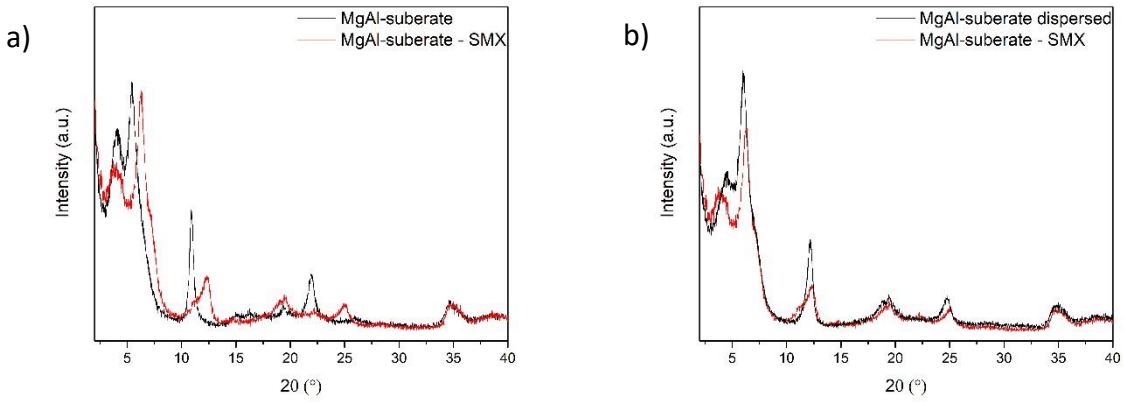

Figure 4. 14 XRPD spectra of MgAl-suberate after adsorption of SMX compared with a) the dried solid before the adsorption, b) the dried sorbent solid after being dispersed in pure water

The same behaviour is observed for MgAl-sebacate, as shown in Figure 4.15 a and b.

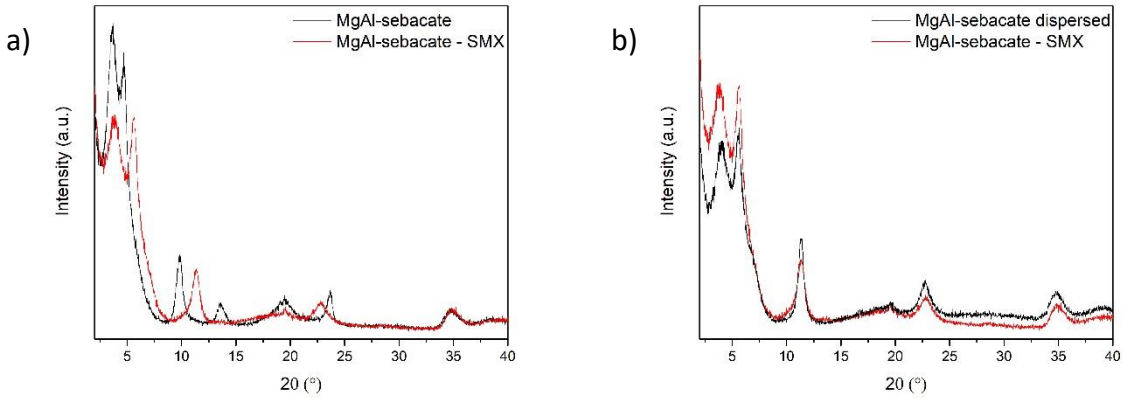

Figure 4. 15 XRPD spectra of MgAl-sebacate after adsorption of SMX compared with a) the dried solid before the adsorption, b) the dried sorbent solid after being dispersed in pure water

MgAl-sebacate LDH shows the same shift after the adsorption of CPX and, also in this case, the change is determined by the different percentage of water in the interlayer region. No other peak is detected, suggesting that the antibiotic is not in the interlayer region or that its concentration in the interlayer region is too low to be detected. The dispersed solid is characterized by the presence of a more intense peak associated to the presence of carbonate anion in the interlayer region compared to the other two solids.

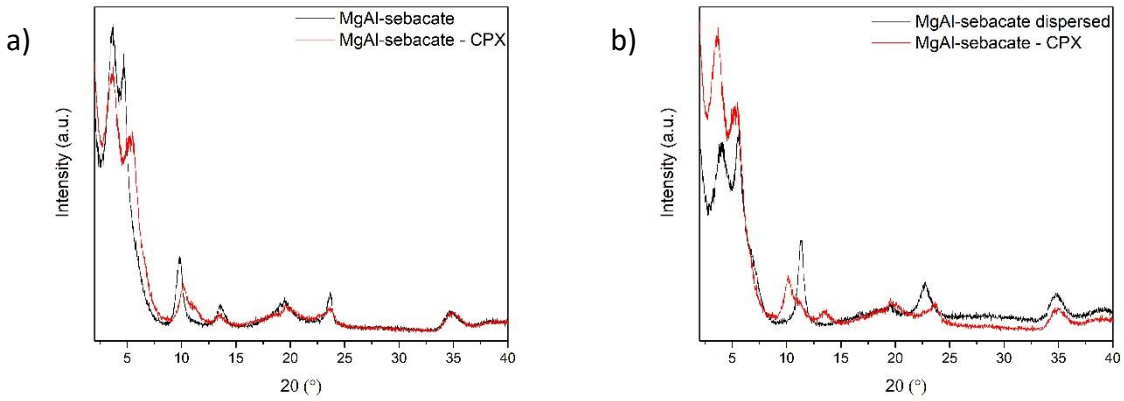

Figure 4. 16 XRPD spectra of MgAl-sebacate after adsorption of CPX compared with a) the dried solid before the adsorption, b) the dried sorbent solid after being dispersed in pure water

The different amount of water between the original powder and the re-dispersed powder was confirmed in both cases by TGA analysis: as it can be seen in Figure 4.17, the original powders have a percentage of water of around 10% in weight (9.2% for MgAl-suberate and 9.5% for MgAl-sebacate), while after the dispersion in water and the drying process the percentages decrease to 4.7% for MgAl-suberate and 5.1% for MgAl-sebacate, consistent with the decrease of the interlayer distance observed at the XRPD. The dried solid seems then to increase its water percentage during time by incorporating it in the interlayer region from the air humidity.

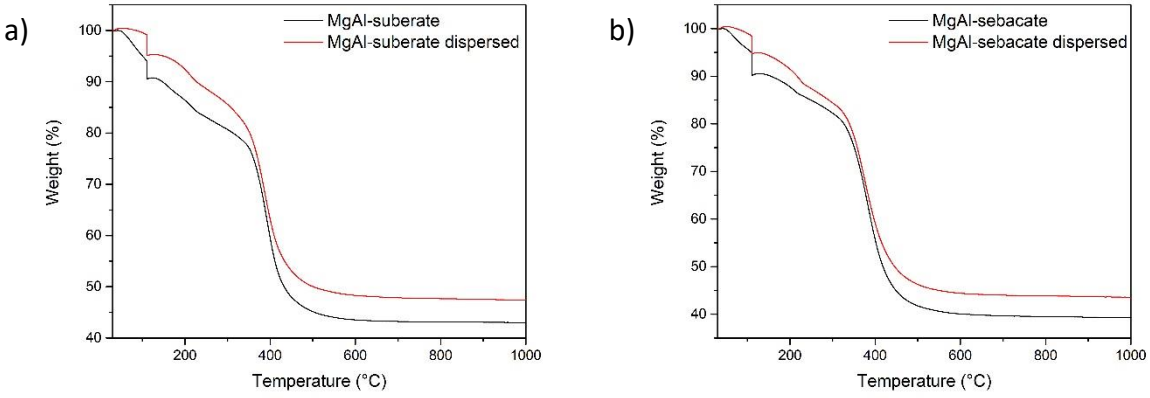

Figure 4. 17 TGA of original powder and the sorbent solid after dispersion in water and drying of a) MgAl-suberate and b) MgAl-sebacate

The XRPD characterization was performed also on MgAl-dodecandioate LDH before and after the adsorption of CPX, as reported in the following figure. No structural variation is observed in this case.

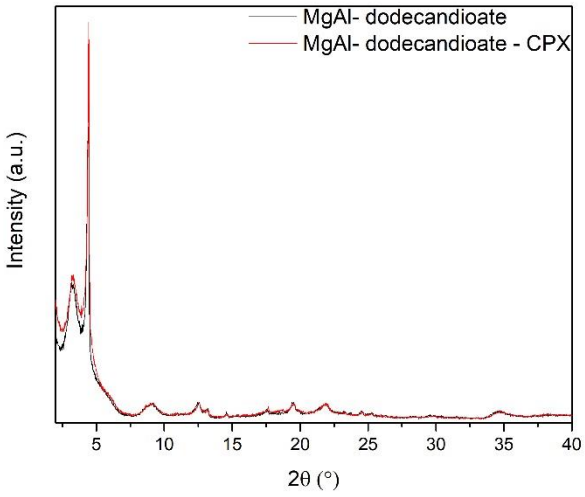

Figure 4. 18 XRPD spectrum of MgAl-dodecandioate before and after the adsorption of CPX

The XRPD spectrum of MgO after the adsorption of CPX is characterized by the same peaks of the pristine MgO (where the signals of both MgO and $Mg(OH)_2$ are visible)[2], but the peaks associated to $Mg(OH)_2$ increase in intensity, while the ones of MgO have lower intensity. The peak at 4.6 Å of the hydroxide may cover the main peak of CPX[3], thus making it impossible to detect the crystalline peak of the antibiotic.

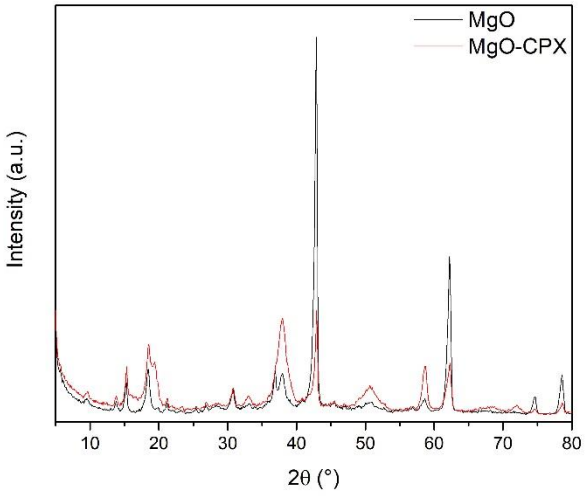

Figure 4. 19 XRPD spectra of MgO before and after CPX adsorption

The SEM images collected for MgAl-pentanoate before and after SMX adsorption are reported below. After the sorption the surface crystals seem to be more compact compared to the original solid.

a) b)

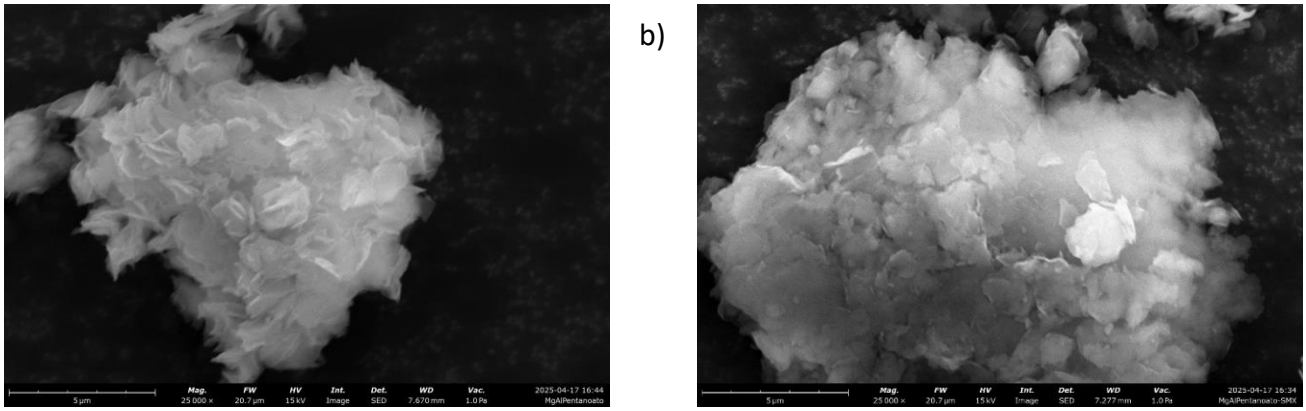

Figure 4. 20 SEM images of MgAl-pentanoate before (a) and after (b) SMX adsorption. Magnification 25000x

The same analysis was conducted for MgAl-suberate, but in this case no big surface modification was observed.

a) b)

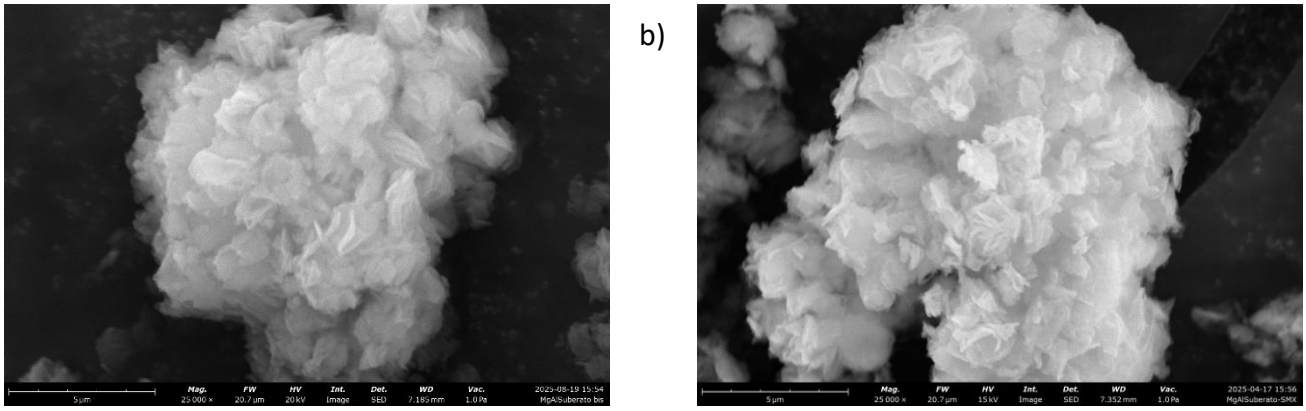

Figure 4. 21 SEM images of MgAl-suberate before (a) and after (b) SMX adsorption. Magnification 25000x

MgAl-sebacate after adsorption of SMX and CPX slightly changes the morphology, showing the presence of more compact crystals.

a) b) c)

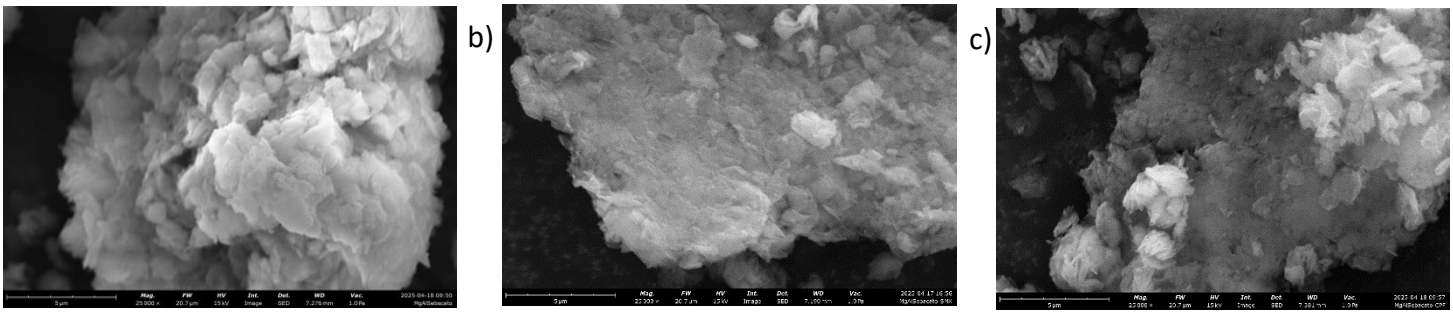

Figure 4. 22 SEM images of MgAl-sebacate before (a) and after SMX (b) and CPX (c) adsorption. Magnification 25000x

The images collected for MgAl-dodecandioate show no major difference between the two solids.

a) b)

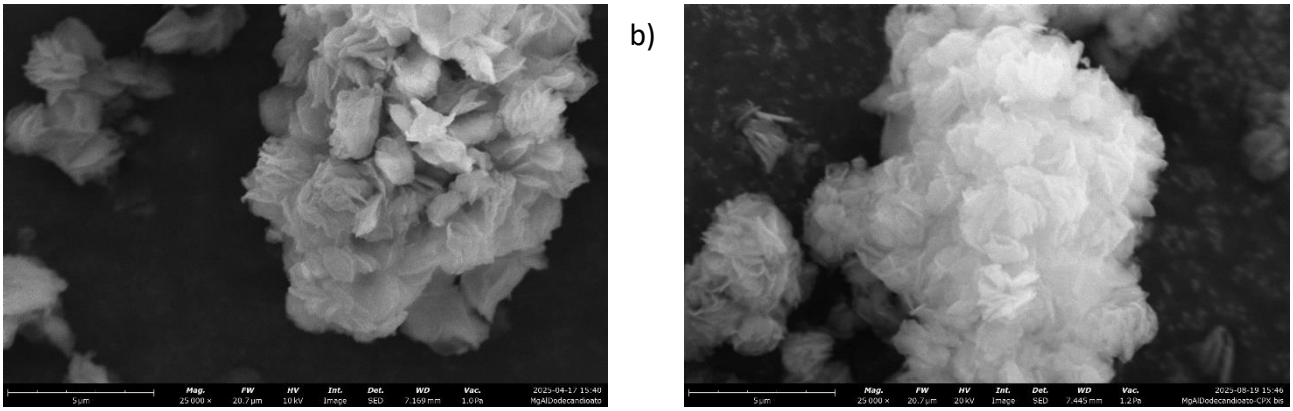

Figure 4. 23 SEM images of MgAl-dodecandioate before (a) and after (b) SMX adsorption. Magnification 25000x

Some changes can be detected in the morphology of MgO after CPX adsorption compared to the original solid, as can be seen in Figure 4.24, but the difference may be due to the formation of magnesium hydroxide.

a) b)

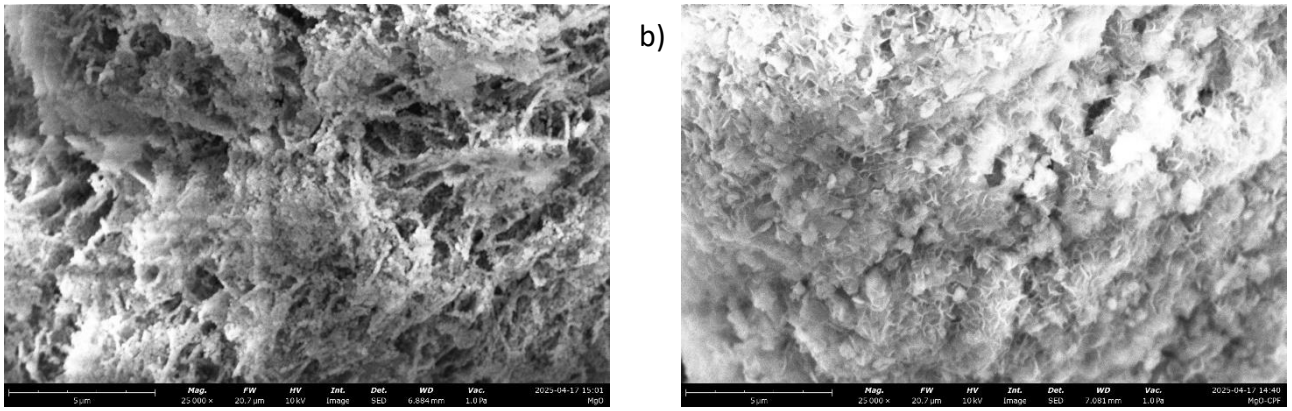

Figure 4. 24 SEM images of MgO before (a) and after (b) CPX adsorption. Magnification 25000x

The EDX analysis didn't show the presence of any element that could be attributed exclusively to the presence of SMX or CPX as nitrogen, sulphur or fluoride: in this case the percentage of antibiotic on the total solid mass is lower than the one adsorbed on ZnAl-acetate LDH, because the ratio antibiotic / sorbent solid in water is lower. The low amount of antibiotic present makes the detection of nitrogen, sulphur or fluoride difficult to accomplish.

The BET surface areas were measured for every solid before and after the adsorptions and the results are listed below.

Table 4. 6 BET surface areas of the studied sorbent solids before and after the antibiotics adsorption

Solid	BET surface area (m^2/g)
MgAl-pentanoate	16.68
MgAl-pentanoate - SMX	30.69
MgAl-suberate	16.83
MgAl-suberate - SMX	20.39
MgAl-sebacate	19.62
MgAl-sebacate - SMX	26.80
MgAl-sebacate - CPX	25.02
MgAl-dodecandioate	17.63
MgAl-dodecandioate - CPX	21.10
MgO	15.65
MgO-CPX	37.91

The most notable variations of surface areas are observed for the solids that showed a relevant morphological change at the SEM after the antibiotic adsorption, i.e. MgAl-pentanoate and MgO. MgAl-sebacate LDHs are characterized by a slight change in surface area, corresponding to small morphological variations observed at SEM, while the other solids undergo a very small change in surface area, corresponding to the absence of modification detected with the electron microscope.

The collected data suggest a surface interaction of the antibiotics with the sorbent solids and the absence of the target molecules in the interlayer region. The greater changes in BET surface area correspond to the greater morphological changes observed at the SEM; the adsorption of the antibiotics on the surface of the solids may affect the aggregation of the particles during the drying process, hence modifying the surface areas. It has to be pointed out though that, in the case of MgO, the formation of the hydroxide may affect the morphology and the surface area, but, for this type of solid, only the surface adsorption is possible.

4.3.4 Adsorption of SMX, CPX and TC

Adsorption of TC was tested using a ratio antibiotic / sorbent solid of 1:20 in weight. The adsorption of SMX and CPX on the most performing solids previously determined for each antibiotic was tested again with the same ratio used for TC. The results are listed below, expressed as mean value ± SD.

Table 4. 7 Quantification of SMX, CPX and TC absorbed on solid in percentage (%), after treatment and HPLC-DAD analysis

Sample entry	SMX	CPX	TC
	%	%	%
Magnesium oxide	-	96.4 ± 0.1	60.3 ± 0.2
MgAl-pentanoate	N.D.	-	88.4 ± 0.2
MgAl-oxalate	-	-	79.2 ± 0.06
MgAl-malonate	-	-	93.5 ± 0.09
MgAl-succinate	-	-	96.8 ± 0.13
MgAl-glutarate	-	-	96.4 ± 0.09
MgAl-adipate	-	-	98.1 ± 0.1
MgAl-pimelate	-	-	96.6 ± 0.12
MgAl-suberate	42.3 ± 0.2	-	97.1 ± 0.1
MgAl-azelate	-	48.1 ± 0.2	98.6 ± 0.1
MgAl-sebacate	12.2 ± 0.2	26.5 ± 0.3	27.8 ± 0.3
MgAl-dodecandioate	-	40.0 ± 0.3	2.1 ± 0.1

The adsorption of the mixed three antibiotics in aqueous solution on the studied sorbent solids was then tested. Given the low percentages of adsorption determined for all the analytes with a ratio between antibiotic and sorbent solid of 1:20, the tests were performed using ratios of each antibiotic: sorbent solid of 1:100, 1:200 and 1:300 in weight.

Only the solids with higher adsorption capacities were selected to perform the test with the antibiotic mix.

The results, listed below, are expressed as mean value ± SD.

Table 4. 8 Quantification of SMX, CPX and TC absorbed on 100, 200 and 300 mg of solid in percentage (%), after treatment and HPLC-DAD analysis

Sample entry	SMX	CPX	TC
	%	%	%
Ratio 1:100			
MgAl-azelate	28.1 ± 0.2	81.6 ± 0.2	74.7 ± 0.1
Magnesium oxide	N.D.	90.2 ± 0.1	99.4± 0.1
MgAl-pentanoate	67.7 ± 0.1	N.D.	98.7 ± 0.2
MgAl-adipate	N.D.	22.2 ± 0.3	98.2 ± 0.1
MgAl-suberate	93.8 ± 0.1	32.2 ± 0.1	98.1 ± 0.2
MgAl-sebacate	74.8 ± 0.2	96.5 ± 0.2	99.5 ± 0.1
Ratio 1:200			
MgAl-azelate	41.9 ± 0.1	84.1 ± 0.1	99.7 ± 0.2
Magnesium oxide	15.4 ± 0.2	95.2 ± 0.3	99.5 ± 0.1
MgAl-pentanoate	70.3 ± 0.2	15.6 ± 0.1	100 ± 0.1
MgAl-adipate	18.5 ± 0.2	33.2 ± 0.2	100 ± 0.1
MgAl-suberate	97.2 ± 0.1	38.9 ± 0.2	99.7 ± 0.1
MgAl-sebacate	80.3 ± 0.3	97.0 ± 0.3	100 ± 0.2
Ratio 1:300			
MgAl-azelate	52.7 ± 0.1	90.0 ± 0.1	100.0 ± 0.1
Magnesium oxide	30.3 ± 0.1	97.4 ± 0.2	100.0 ± 0.2
MgAl-pentanoate	75.9 ± 0.1	28.8 ± 0.4	100.0 ± 0.1
MgAl-adipate	20.1 ± 0.2	39.9 ± 0.1	100.0 ± 0.2
MgAl-suberate	100 ± 0.1	42.7 ± 0.2	100.0 ± 0.2
MgAl-sebacate	88.9 ± 0.2	97.5 ± 0.2	100.0 ± 0.1

Increasing the quantity of sorbent solids, the percentages of adsorption increase for every antibiotic and every solid. Notably TC is well adsorbed on every sorbent solid, while SMX and CPX follow the same trend observed in the previous experiments conducted for each antibiotic. Even though high

percentages of removal for specific antibiotics are determined for various sorbents, the two solids that adsorb in higher percentage all the three antibiotics are MgAl-azelate and MgAl-sebacate.

Also in this case the presence of a lipophilic portion of the intercalated anion alongside the hydrophilic COOH moiety seem to enhance the adsorption capacity of the LDH.

The most promising solids were characterized before and after the adsorption process as was done before for the previous experiments. The ratio used for the characterization of the sorbent solids was the one with higher performances, 1:300.

4.3.5 Solids characterization after adsorption of SMX, CPX and TC

MgAl-azelate and MgAl-sebacate were characterized via XRPD analysis in order to verify if any variation had occurred in the crystalline structure after the antibiotics adsorption.

Figure 4.25 shows the XRPD spectra of MgAl-azelate before and after the adsorption of the mix of the antibiotics. As it was observed in previous experiments conducted with this material, no variation in the crystalline structure was observed.

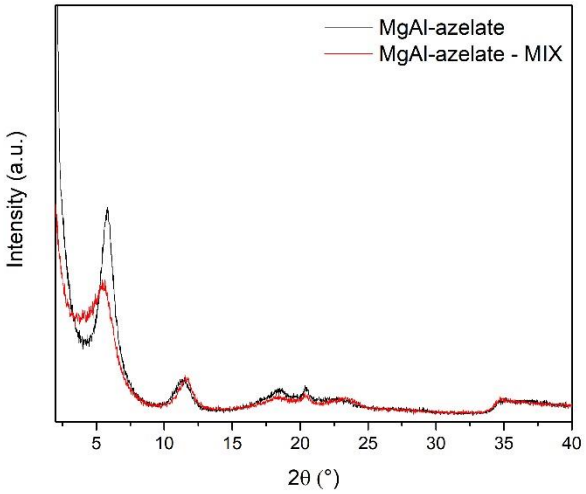

Figure 4. 25 XRPD spectra of MgAl-azelate before and after antibiotics adsorption

MgAl-sebacate after the adsorption is characterized by the presence of a shifted second peak. This behaviour is the same already observed for this material in the previous paragraphs and is attributed to a different percentage of humidity in the interlayer region.

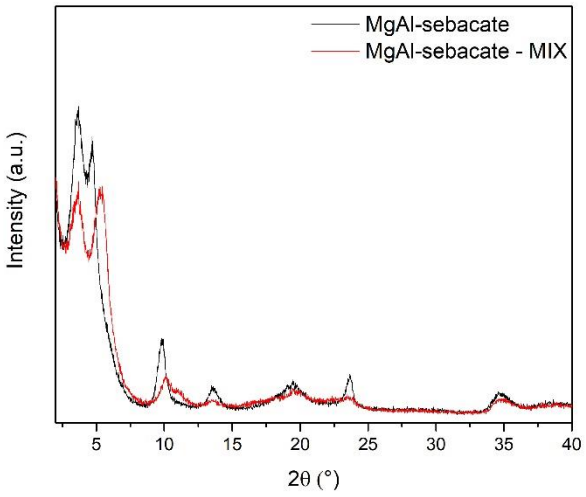

Figure 4. 26 XRPD spectra of MgAl-sebacate before and after antibiotics adsorption

The SEM images collected in order to verify whether a morphological change occurs after the adsorption, show that the MgAl-azelate LDH does not change its morphology after the contact with the antibiotic mix.

a) b)

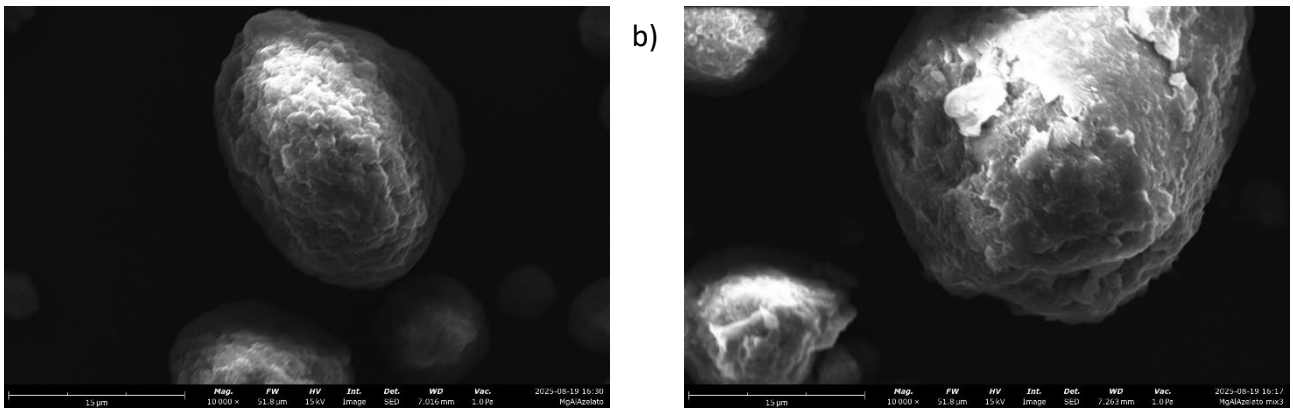

Figure 4. 27 SEM images of MgAl-azelate before (a) and after (b) antibiotic mix adsorption. Magnification 10000x

A slight change in MgAl-sebacate morphology is observed, as it was already detected for the other tests conducted with antibiotics.

a) b)

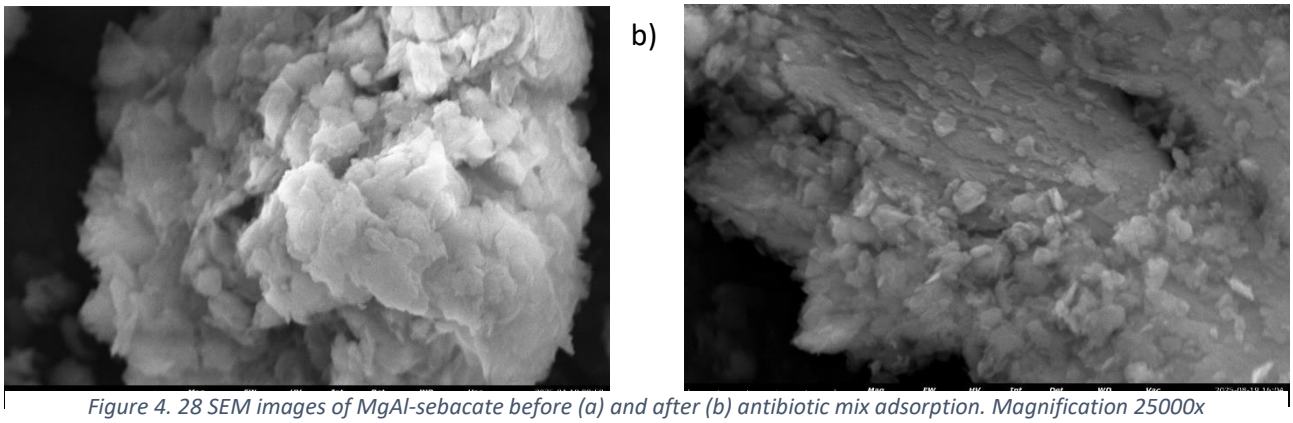

Figure 4. 28 SEM images of MgAl-sebacate before (a) and after (b) antibiotic mix adsorption. Magnification 25000x

Also in this case the EDX analysis didn't detect any element that could mark the presence of SMX, CPX or TC (i.e. nitrogen, sulphur or fluoride), because of the low ratio between the antibiotics and the sorbent solids.

BET surface areas were also monitored, and the results are shown in Table 4.9.

Table 4. 9 BET surface areas of the studied solids

Solid	BET surface area (m^2/g)
MgAl-azelate	1.31
MgAl-azelate - MIX	4.55
MgAl-sebacate	19.62
MgAl-sebacate - MIX	25.62

Both sorbent solids slightly increase their surface area after the adsorption, as it was already observed in other similar experiments.

4.4 PRODUCTION OF PELLETS FOR ADSORPTION TESTS IN COLUMN

MgAl-sebacate LDH was produced in pellets in order to be able to arrange the solid in column and flux the contaminated water through it without reaching high pressures. This system allows for easier use of LDH on a large scale, a prerequisite for future industrial applications.

The pellets were produced and physically characterized by Prof. Paolo Colombo's group in Università di Padova: the powder was blended with silica precursor, 3D printed and cured at 200°C, obtaining a compound with a mass content of LDH of 50%. The obtained material has a BET surface area of 164.6 m^2/g and a pore average diameter of 9.76 nm, that makes it possible to access the sorbent solid.

A photo of the produced pellets is reported in Figure 4.29.

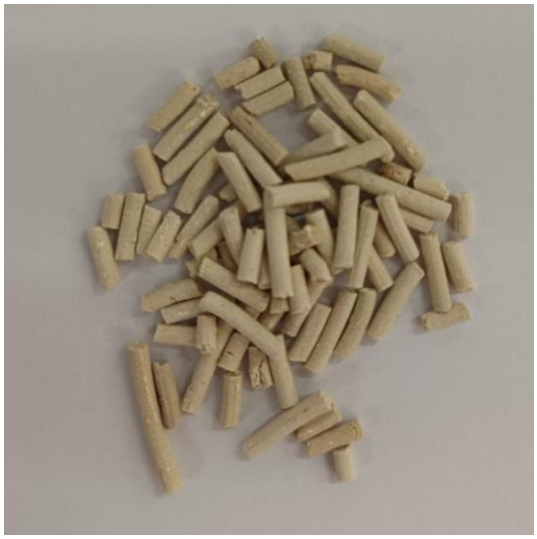

Figure 4. 29 Produced MgAl-sebacate pellets 50% wt

In future studies a column packed with LDH pellets will be developed to test the adsorption capacity of the engineered material.

BIBLIOGRAPHY

[1] A. L. Boreen, W. A. Arnold, K. McNeill, "Photochemical Fate of Sulfa Drugs in the Aquatic Environment: Sulfa Drugs Containing Five-Membered Heterocyclic Groups" *Environ. Sci. Technol.* **2004**, *38*, 3933–3940.

[2] S. Yousefi, B. Ghasemi, M. P. Nikolova, "Opto-structural characterization of Mg(OH)2 and MgO nanostructures synthesized through a template-free sonochemical method" *Appl. Phys. A* **2021**, *127*, 549.

[3] S. Thangadurai, S. K. Shukla, A. K. Srivastava, Y. Anjaneyulu, "X-ray powder diffraction patterns for certain fluoroquinolone antibiotic drugs" *Acta Pharm* **2003**, *53*, 295–304.

5 CONCLUSIONS AND FUTURE DEVELOPMENTS

5.1 TARGET MOLECULES SEPARATION FROM PHYTOEXTRACTS

During this thesis work, different experiments have been performed to better understand the adsorption mechanism of gentiopicroside and amarogentin from *G. lutea* extract and of emodin and chrysophanol from *P. cuspidatum* on MgAl-azelate LDH. Regarding *G.* lutea extract, from the study performed we managed to understand that not only the inorganic matrix plays an important role in the adsorption mechanism (thanks to the presence of magnesium atoms and hydroxyl groups), but also the nature of the interlayer counterion is important for the process. The presence of the second carboxylic moiety on the organic anions improves the adsorption capacity, probably thanks to the possibility of establishing a greater number of hydrogen bonds compared to their monocarboxylic counterpart. At the same time, the chain length seems to be another important factor for the tuning of the adsorption performance of the solid: with alkyl chains longer than four carbon atoms, the adsorption of both the secondary metabolites seems to reach its maximum, with higher retention percentages towards amarogentin rather than gentiopicroside, as it was observed for all the organically modified LDHs. This behaviour was interpreted as a higher affinity of the target molecules for organic modifiers with a bigger apolar region between the hydrogen bond-reach regions.

From the analysis of MgAl-azelate LDH before and after the adsorption of target molecules from *G. lutea* and *P. cuspidatum*, the hypothesis of a surface interaction via weak bond rather than an interlayer adsorption with a typical host-guest behaviour, have been formulated. To confirm this, the adsorption process was performed on two MgAl-CO_3 LDHs with different surface areas and the high surface area solid showed higher compatibility for the molecules. When the study was conducted, in our laboratories the only known way to synthetize two MgAl-CO_3 LDHs with different surface areas involved a slight change in the composition of the layer, varying a bit the Mg:Al ratio. Lately a new synthesis method is being developed that allows us to get higher surface areas with the same Mg:Al ratio; this newly developed material will be tested as sorbent solid for *G. lutea* and *P. cuspidatum* extracts in future studies.

5.2 ANTIBIOTIC REMOVAL

The second part of this thesis focused on pollutants removal, in particular on antibiotics removal (sulfamethoxazole, ciprofloxacin and tetracycline hydrochloride). In this case different solids were tested: after trying to remove SMX with solids that could give anion exchange and noticing some recyclability problems due to the carbonate anion intercalation in the interlayer region, solids that are more likely to give weak forces interaction were tested for all the three antibiotics. The most performing solids for SMX, CPX and the mix of the three antibiotics were analysed before and after the adsorption process. Also in this case the adsorption seems to be due to a surface interaction with the lamellar solids and doesn't seem to affect the interlayer region. The most promising solid, with the higher adsorption percentages for the mix of the three antibiotics is the MgAl-sebacate LDH. With a ratio in weight of each antibiotic/LDH of 1:300 the adsorbance percentages are 88.9% of SMX, 97.5% of CPX and 100% of TC, meaning that for 1 g of LDH 3.0 mg of SMX, 3.2 mg of CPX and 3.3 mg of TC are adsorbed from a solution containing 3.3 mg of each antibiotic. To the best of our knowledge, no simultaneous removal of the three studied antibiotics has been reported in literature. LDH containing silica pellets were developed for application on greater scale by fluxing contaminated water through a column filled with pellets.

In future studies the effect of multiple cycles of adsorption and desorption of the antibiotic mix from MgAl-sebacate LDH will be investigated and the adsorption in column will be tested, using the developed LDH-SiO_2 pellets. Other investigations will concern the effect of the matrix: the adsorption process will be conducted in wastewater doped with the antibiotic mix.